Biochemical and structural characterization of NOD-like receptors and insights into their function in innate immune signaling

Dissertation

zur

Erlangung des Doktorgrades (Dr. rer. nat.)

der

Mathematisch-Naturwissenschaftlichen Fakultät

der

Rheinischen Friedrich-Wilhelms-Universität Bonn

vorgelegt von

Christoph Winterberg

aus

Siegburg

Bonn, 2025

Angefertigt am Institut für Strukturbiologie
der Rheinischen Friedrich-Wilhelms-Universität Bonn
mit Genehmigung der Mathematisch-Naturwissenschaftlichen Fakultät
der Rheinischen Friedrich-Wilhelms-Universität Bonn

Gutachter/Betreuer: Prof. Dr. Matthias Geyer
Gutachter: Prof. Dr. Ulrich Kubitscheck

Tag der Promotion: 11.12.2025

Erscheinungsjahr: 2025

Table of Contents

Preface

All living organisms face constant biological threats from their environment, including exposure to infectious agents, tissue damage, and cellular stress. To survive, they rely on a complex innate and adaptive immune system capable of detecting internal and external danger signals. In higher organisms, immunity serves not only as a defense mechanism, but also as a critical regulator of homeostasis, inflammation, and tissue repair. At the cellular level, the immune system operates through intricate signaling networks that must remain sensitive and highly specific. These networks activate only when necessary and resolve quickly to avoid collateral damage. Pattern recognition receptors are an important building block in this system, while functioning as cellular sensors. Once activated, these receptors can trigger powerful immune responses, such as the assembly of inflammasomes, activation of inflammatory cytokines, and induction of programmed cell death pathways, including pyroptosis.

Over the past two decades, research has revealed that pattern recognition receptors have a wide range of functions, including roles in chronic inflammation, metabolic regulation, and autoimmune disease, in addition to infection control. Their ability to distinguish between physiological and pathological states is central to immune regulation and makes them a subject of intense investigation in current immunological studies.

Abstract

The human immune system is composed of two main parts, the innate and the adaptive immune system. Pattern recognition receptors (PRRs) present in the innate immune system are capable of recognizing pathogens via pathogen-associated molecular patterns (PAMPs). Nucleotide-binding oligomerization domain (NOD)-like receptors (NLRs) belong to the cytosolic PRRs and can be divided into two major subfamilies, pyrin domain-containing receptors (NLRPs) or caspase recruitment domain-containing receptors (NLRCs). This thesis focusses on the NOD-like receptors NLRP10, NLRP12 and NOD2. It covers different biochemical approaches and techniques regarding protein design, purification, interaction and activation.

Nucleotide-binding domain, leucine-rich repeat and pyrin domain containing receptor 10 (NLRP10) is a PRR that is activated by mitochondrial damage, which leads to NLRP10 inflammasome activation, ASC speck formation, and caspase-1-dependent cytokine release (Próchnicki et al., 2023; D. Zheng et al., 2023). Also, poly (I:C) has been hypothesized to be an activator of the NLRP10 inflammasome (Masters, 2023). In this thesis was shown that truncated constructs of NLRP10 offer a different behavior during purification from recombinant expression by forming a monomer-dimer equilibrium in solution. Through mutation of several lysine and arginine residues to glutamines in the C-terminal region, the overall positive charge was removed, decreasing the interaction with cellular membranes and resulting in a highly reduced activity of NLRP10. This was shown by decreased ASC speck formation leading to the hypothesis that either nucleotide or membrane binding is involved in the NLRP10 inflammasome activation. These results are consistent with the observation that mitochondrial damage and release of distinct molecular entities leads to NLRP10 activation.

The chapter about NLRP12 deals with the off-target effect of small molecule inhibitors that interact with NLRP3, the closest neighbor in the NLRP family (Hochheiser, Pilsl, et al., 2022; Keuler et al., 2022). Therefore, various interaction studies using surface plasmon resonance (SPR) spectroscopy, thermal shift assays, and crystallization experiments were performed. In addition, an effort was made to obtain novel NLRP12-specific binders in collaboration with the Core Facility Nanobodies at the University Clinics Bonn.

The receptor NOD2 belongs to the CARD containing subfamily and was shown to be activated by sensing muramyl dipeptide (MDP) to induce subsequent signaling (Girardin et al., 2003; Inohara et al., 2003; Stafford et al., 2022). During the expression and purification of NOD2, the binding partner valosin-containing protein (VCP) was identified and characterized. It was endogenously co-purified from *Sf-9* insect cells and formed stable complexes with NOD2. The regulatory effect of VCP on the inflammatory response in NOD2 activation has been described previously (Ghalandary et al., 2022).

Since the function and structure of these NOD-like receptors are poorly described, they are valuable targets for future research to gain more insights and develop possible approaches for pharmaceutical applications.

1. Introduction

1.1 The immune system

Living organisms have evolved various forms of immune responses to protect themselves from environmental pathogens such as viruses, bacteria, and fungi. These defenses have evolved over billions of years and vary in complexity among different organisms. The immune response was first described by Edward Jenner in 1796, who discovered that vaccination with cowpox could protect against a serious disease called smallpox. In the 19th century, other scientists, such as Robert Koch and Louis Pasteur, developed strategies for vaccinating against other diseases like cholera. Emil von Behring and Shibasaburo Kitasato discovered antibodies in 1890. They found that these particles specifically bound to the respective pathogens in vaccinated organisms. Based on these observations Elie Metchnikoff introduced the distinction between innate and adaptive immunity (Janeway et al., 2001).

The defense against physical stress or pathogens evolved already in procaryotes and archaea. This immune system differentiated into innate and adaptive responses to fight more efficiently against physical stress or bacteriophages. Two prominent antiviral immune mechanisms are the restriction-modification system (innate) and the CRISPR-Cas system (adaptive) (Jansen et al., 2002; Wein & Sorek, 2022). Based on this system, a gene-editing technique was engineered by Jennifer Doudna and Emmanuelle Charpentier, who were awarded the Nobel Prize in Chemistry in 2020 (Deltcheva et al., 2011; Jinek et al., 2012; Strzyz, 2020). Plants also possess an innate immune system using for example pattern recognition receptors (PRRs) to identify and combat pathogens (Zipfel, 2014). Other eukaryotes have evolved more complex systems built up by different parts for immune responses.

Today, the human immune system is the most highly developed and complex immune system composed of the innate and the adaptive immune system (**Figure 1-1**).

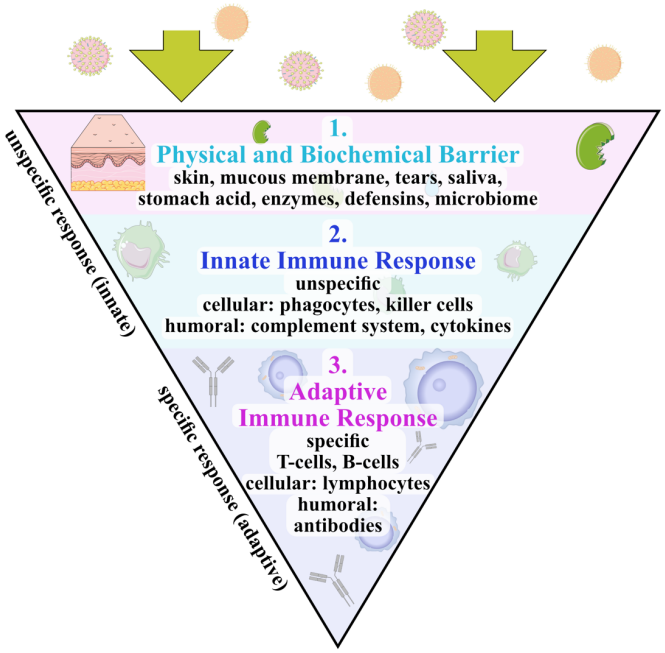

Figure 1-1: Overview of the human immune system.
The human immune system is divided into two parts, unspecific innate response and specific adaptive response. There are several components involved like physical barriers, cellular or humoral mechanisms. This figure was modified from dr-boehm.at/ratgeber/immunsystem (2025) and was created with bioicons.com.

1.1.1 Innate immune system

The innate immune system (IIS) serves as the body's first line of defense, providing a rapid but non-specific response to pathogens. The defense mechanisms have grown and adapted over thousands of years. Time and time again, epidemics and pandemics have afflicted mankind towards many different pathogens. Two prominent examples are *Yersinia Pestis* and *Vibrio Cholerae*, which are highly infectious and deadly bacteria (Kaper et al., 1995; Morelli et al., 2010). Unlike the adaptive immune system, previous exposure to pathogens is not required for an effective immune response. The IIS includes physical barriers such as the skin, mucous membrane and cilia, as well as different cellular and molecular components. The skin acts as physical protection, while mucous membranes in the respiratory and digestive tracts capture pathogens and remove them. In addition, stomach acid and enzymes in saliva aid in the destruction of pathogens. In the IIS several immune cells are involved in the immune response including macrophages, which process and digest pathogens through phagocytosis; neutrophils, which act as first responders to infection, and natural killer (NK) cells, which identify and destroy infected or cancerous cells. Upon infection, inflammation triggers the recruitment of immune cells to the affected loci, mediated by cytokine release and other signaling molecules. In addition, the complement system, a group of proteins, enhances the ability of antibodies and immune cells to eliminate pathogens (Püschel et al., 2011; Wein & Sorek, 2022).

1.1.2 Adaptive immune system

The adaptive immune system (AIS) provides a more specific and prolonged defense against pathogens. In contrast to the innate immune response, the AIS takes more time to respond to infections. However, the AIS creates a memory of past infections to respond more quickly and specifically to re-infections. B-cells and T-cells are the main components included in this response.

B cells, also known as lymphocytes, are a type of white blood cell that matures in the bone marrow and can recognize pathogens. These so-called plasma cells produce antibodies that neutralize pathogens or target them for subsequent destruction. After an infection, memory B cells remain in the body to respond quicker and more efficient upon reinfection.

T cells are also white blood cells and carry a T-cell receptor (TCR) on their surface. They originate in the bone marrow but mature in the thymus gland, where they differentiate into a number of different subtypes. Helper T-cells release cytokines that regulate and enhance immune responses, while cytotoxic T-cells directly attack infected or abnormal cells. In addition, memory T-cells persist after an infection, allowing for a faster and stronger immune response upon re-infection with the same pathogen. These specialized cells work in concert with other immune components to provide an effective and targeted defense against infection and disease (Bonilla & Oettgen, 2010; Püschel et al., 2011).

The innate and adaptive immune responses are not independent of each other. In fact, they are interconnected and work in tandem. The IIS activates the AIS by presenting antigens to lymphocytes. For example, dendritic cells process antigens and present them to T cells, providing the link between the two systems. Together, they form the human immune system and provide the best possible protection mechanism against foreign dangers.

1.2 Pattern recognition receptors

Pattern recognition receptors (PRRs) span a class of various proteins, which are capable of recognizing distinct pathogen patterns or specific molecular structures. These are either called pathogen-associated molecular patterns (PAMPs) or danger-associated molecular patterns (DAMPs). The concept of PRRs was first described as the link between innate immune signaling and induction of adaptive immune response in 1989 (Janeway, 1989). These findings have affected the research on innate immunity to this day (Janeway, 1989; Li & Wu, 2021). By recognition of these molecular patterns, the human immune system can rapidly react to foreign dangers and protect our bodies. PRRs are divided in two classes, transmembrane and cytosolic receptors. Toll-like receptors (TLRs) and C-type lectin receptors (CLRs) are surface receptors and located in the cell membrane. NOD-like receptors (NLRs) and RIG-I-like receptors (RLRs, or RIG-I helicases) are cytosolic receptors present in the cytoplasm (**Figure 1-2**). All receptors interact with different activators (e.g., LPS, RNA, DNA) causing downstream signaling effects. They can occur in different manners, such as oligomerization, induction of inflammatory signaling pathways, recruitment of adaptor proteins or activation of kinases. PRRs are mainly expressed in immune cells, such as macrophages or dendritic cells, and are composed of a central regulatory or transmembrane domain, a ligand recognition domain and an effector domain (Li & Wu, 2021; Takeuchi & Akira, 2010; Thompson et al., 2011).

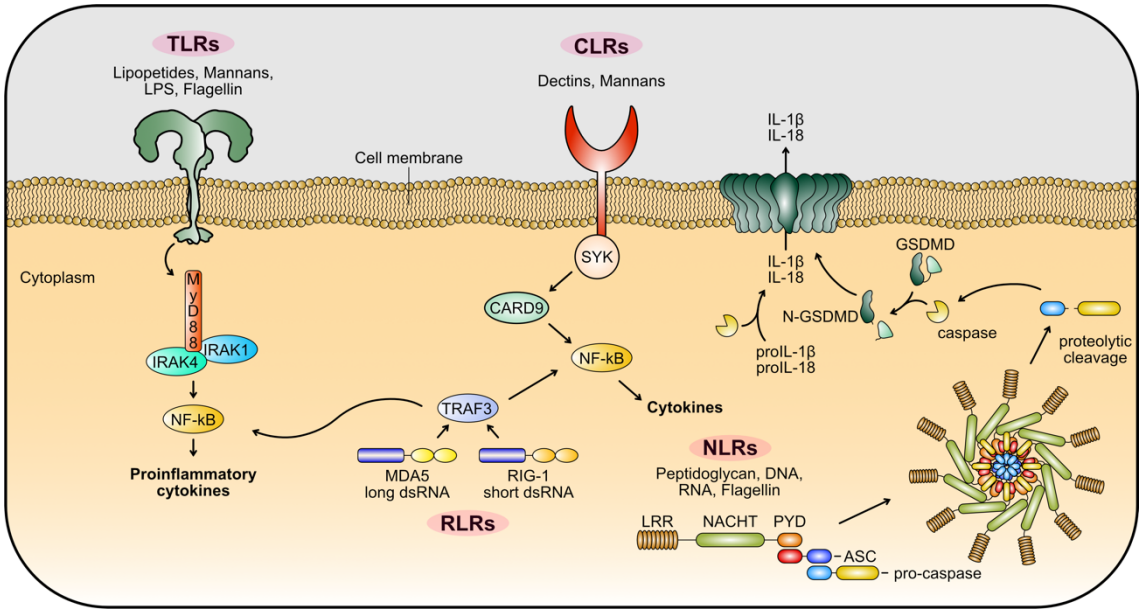

Figure 1-2: Overview of Pattern Recognition Receptor families.
The four major classes of pattern recognition receptors in human innate immunity: Toll-like receptors (TLRs), C-type lectin receptors (CLRs), NOD-like receptors (NLRs) and RIG-I-like receptors (RLRs). TLRs and CLRs are located in the membrane, whereas NLRs and RLRs are located in the cytoplasm. Example pathways of the receptors induced by different activators are shown. This figure is a simplified summary of pattern recognition receptors and was modified from (Schwartz et al., 2011).

Dysfunction in these complex mechanisms and pathways can lead to autoimmune diseases through up- or downregulation of various receptors and inflammatory signals, such as nuclear factor-κB (NF-κB), resulting in the release of pro-inflammatory cytokines. Several mechanisms, structures and interaction partners are not yet fully understood and are under investigation by numerous research groups.

1.2.1 Toll-like receptors

The toll-like receptor (TLR) family represents one part of transmembrane PRRs. They are mainly involved in the detection of PAMPs and DAMPs and inducing downstream molecular pathways. TLRs were initially discovered in *Drosophila melanogaster* to be responsible for NF-κB signaling, embryonic development and immunity (Lemaitre & Hoffmann, 2007; Valanne et al., 2011). Later they were also described to play a crucial role in the recognition of microbial components and cellular stress in mammals (Akira et al., 2001).

In humans, ten members of the TLR family are identified (TLR1 to TLR10), recognizing specific ligands (e.g., flagellin, LPS) in different membranes. TLRs are present in many immune cells like macrophages, dendritic cells, neutrophils and epithelial cells (Duan et al., 2022). Regarding to their localization in cells, TLRs can be assigned into two subgroups: cell surface membrane located TLRs (TLR1, TLR2, TLR4, TLR5, TLR6) or endosome membrane located TLRs (TLR3, TLR7, TLR8, TLR9, TLR10) (Lim & Staudt, 2013).

Different TLRs are specific receptors for distinct molecular patterns. For example, TLR4 is localized in the plasma membrane and recognizes lipopolysaccharides (LPS) from gram-negative bacteria. Upon activation it gets endocytosed into endosomes (H.-J. Kim et al., 2023). TLR3 is responsive to dsRNA, introduced by several viruses, whereas TLR7 and TLR8 are responsive to ssRNA. TLR1, TLR2 and TLR6 are activated by lipopeptides at the plasma membrane and flagellin is a specific activator for TLR5. Upon ligand binding, TLR dimerization is induced and an intracellular signaling cascade is initiated, leading to myddosome complex formation. Myeloid differentiation primary response 88 (MyD88) is recruited to the TLR-TIR domain and subsequently binds interleukin-1/2/4 receptor-associated kinases (IRAK1/2/4) via death domain (DD) interactions (**Figure 1-3**) (Balka & Nardo, 2019; Gay, 2019). Downstream signaling activates transcription factors such as NF-κB, AP-1, and IRFs, ultimately leading to the production of pro-inflammatory cytokines, type I interferons, chemokines, and other mediators that orchestrate early immune response and bridge to adaptive immunity (Duan et al., 2022).

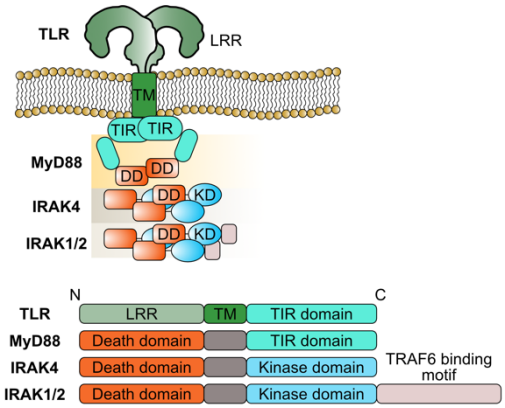

Figure 1-3: TLR signaling induces myddosome complex formation.
TLR receptors consist of three domains: N-terminal LRR, central trans-membrane domain (TM) and C-terminal toll-interleukin receptor domain (TIR). Recruitment of MyD88 via TIR domain interaction. Death domain (DD) of MyD88 interacts with DD of IRAK4. Further complex elongation due to DD interactions between IRAK4 and IRAK1/2. Oligomerization leads to auto-phosphorylation of kinase domains (KD) and subsequent signaling via TNF receptor associated factor 6 (TRAF6). This figure was modified from (Balka & Nardo, 2019).

Abnormalities in TLR signaling are associated with various chronic inflammatory diseases or autoimmune disorders. Research towards the understanding of TLR signaling has improved the treatment of diseases such as respiratory diseases like COVID-19 (M. Zheng et al., 2021), cardiovascular diseases like myocardial inflammation (Yang et al., 2016), and atherosclerosis (Fukuda et al., 2019). Also, digestive diseases like ulcerative colitis, necrotizing small bowel colitis (Høivik et al., 2013), and sepsis (Salomão et al., 2008) are diseases associated with TLR signaling.

1.2.2 C-type lectin receptors

C-type lectin receptors (CLRs) represent another group of transmembrane PRRs with a diverse group of receptors. They are capable of binding carbohydrate structures in a calcium dependent manner. Predominantly carbohydrates derived from fungal infections and bacterial or viral structures like LPS, flagellin or DNA/RNA are recognized (Geijtenbeek & Gringhuis, 2009). CLRs are mainly expressed in myeloid cells, including dendritic cells, macrophages, and monocytes and play a key role in translating innate immune signaling into T and B cell responses (Sousa et al., 2024).

All CLRs contain one or more extracellular C-type lectin-like domains (CTLDs) responsible for ligand binding. Based on their structure, they can be divided into subfamilies including the best studied dectin or mannose receptors. One major function is the ability to detect fungal pathogens. For example, dectin-1 recognizes β-glucans which are present in the cell walls of fungi such as *Candida albicans* and *Aspergillus fumigatus* (Brown, 2006). Upon ligand binding, dectin-1 initiates intracellular signaling via an immunoreceptor tyrosine-based activation motif (ITAM) in its cytoplasmic domain, recruiting the spleen tyrosine kinase (SYK). This recruitment process activates NF-κB and other transcription factors, which ultimately results in the production of pro-inflammatory cytokines and chemokines (Brown, 2006; Kalia et al., 2021).

1.2.3 RIG-I-like receptors

RIG-I-like receptors (RLRs) are a class of intracellular PRRs that play a critical role in the recognition and control of viral infections. There are three members described in the RLR family: retinoic acid-inducible gene-I (RIG-I), melanoma differentiation-associated protein 5 (MDA5), and laboratory of genetics and physiology 2 (LGP2). These receptors mediate antiviral immune responses by recognizing viral RNA in the cytoplasm and initiating signaling cascades (Goubau et al., 2013).

RIG-I, MDA5 and LGP2 share a similar architecture build up by a central DExD/H helicase domain, responsible for RNA binding, a repressor domain (RD) and a C-terminal domain (CTD) for ligand binding. RIG-I and MDA5 each contain two N-terminal caspase activation and recruitment domains (CARDs) responsible for oligomerization upon activation (Li & Wu, 2021). LGP2 lacks the CARD domains and has been shown to interact with RIG-I and MDA5, thereby regulating immune responses mediated by the latter two (Rehwinkel & Gack, 2020).

RIG-I primarily recognizes short double-stranded RNA (dsRNA) and 5'-triphos-phorylated single-stranded RNA (ssRNA), whereas MDA5 was shown to bind long dsRNA, as well as the synthetic RNA, poly I:C (Bamming & Horvath, 2009). RNA binding leads to activation by self-oligomerization and subsequent CARD-CARD interactions with the mitochondrial antiviral-signaling protein (MAVS) at the outer mitochondrial membrane. This interaction induces the activation of transcription factors such as IRF3, IRF7 and NF-κB, ultimately leading to inflammatory cytokine release (Rehwinkel & Gack, 2020).

1.2.4 NOD-like receptors

The human NLR family consists of 22 cytosolic pattern recognition receptors (PRRs) that detect foreign pathogens or danger-associated molecular patterns (DAMPs), thereby initiating innate immune responses (Creagh & O'Neill, 2006; M. H. Shaw et al., 2008; P. J. Shaw et al., 2010). These patterns can have many different origins such as environmental threats (alum, silica, asbestos, UV, etc.), microbial components (peptidoglycan, flagellin, viral RNA, etc.) or host cell compartments (ATP, cholesterol crystals, etc.) (Y. K. Kim et al., 2016; Motta et al., 2015).

To name some examples of NLR activators, bacterial cell wall-derived muramyl dipeptide (MDP) is recognized by NOD2 as well as NLRP1 and causes downstream signaling (Mo et al., 2012; Reubold et al., 2014). Flagellin, a protein present in flagellated bacteria, was found to activate the NAIP/NLRC4, as well as the NLRP3 inflammasome (Gram et al., 2020). Also, ATP was shown to activate the NLRP3 inflammasome (Motta et al., 2015). The current understanding of the activation and function of different NLRs is limited and still being investigated.

The NLR family proteins share a similar domain architecture composed of an N-terminal death-fold family effector domain, a central NACHT (NAIP [NLR family apoptosis inhibitory protein], CIITA [class II, major histocompatibility complex, trans activator], HET-E [incompatibility locus protein from *Podospora anserina*], and TP1 [telomerase-associated protein]) domain, and a C-terminal LRR domain (Chou et al., 2023; Meunier & Broz, 2017).

The **N-terminal effector domain** is responsible for the classification in four different subfamilies: NLRAs, NLRBs, NLRCs and NLRPs (**Figure 1-4**) (Y. K. Kim et al., 2016). In humans, NLRA and NLRB are represented by each one protein. CIITA contains an N-terminal caspase activation and recruitment domain (CARD) and an acidic trans activation domain (AD). NAIP contains three N-terminal BIR (baculovirus inhibitor of apoptosis protein repeat) domains. The largest subfamily, the NLRPs, includes 14 members (NLRP1-14) that all contain an N-terminal pyrin domain (PYD). The NLRC subfamily includes five members: NOD1 (NLRC1), NOD2 (NLRC2), NLRC3, NLRC4, and NLRC5. NOD1, NOD2, and NLRC4 contain either one or two CARD domains, whereas NLRC3 and NLRC5 contain a CARD-like domain. NLRX1 is also associated with the NLRC family and has an N-terminal MLS (mitochondrial localization signal) domain (Chou et al., 2023; Meunier & Broz, 2017).

Both the PYD and CARD domains share a six-helical bundle fold and belong to the death-fold protein superfamily. They are known to form homotypic PYD-PYD or CARD-CARD interactions, which results in formation of large oligomers (Huoh & Hur, 2022; Kersse et al., 2011). However, not all of these receptors assemble into higher order protein complexes in solution independently. Specific interaction partners or triggers may also influence this process.

The central **NACHT domain** contains four subunits that characterize NLRs as signal transduction ATPases with numerous domains (STAND). The nucleotide-binding domain (NBD), helical domain 1 (HD1), the winged helix domain (WHD), and helical domain 2 (HD2) comprise several conserved motifs involved in nucleotide hydrolyses. The NBD covers the highly conserved Walker A and Walker B motif, whereas the helical domains accommodate several sensor residues (Brinkschulte et al., 2022). It was described that ATP hydrolysis induces conformational changes in NLRs and causes signal transduction (Platnich & Muruve, 2019; Sandall et al., 2020a).

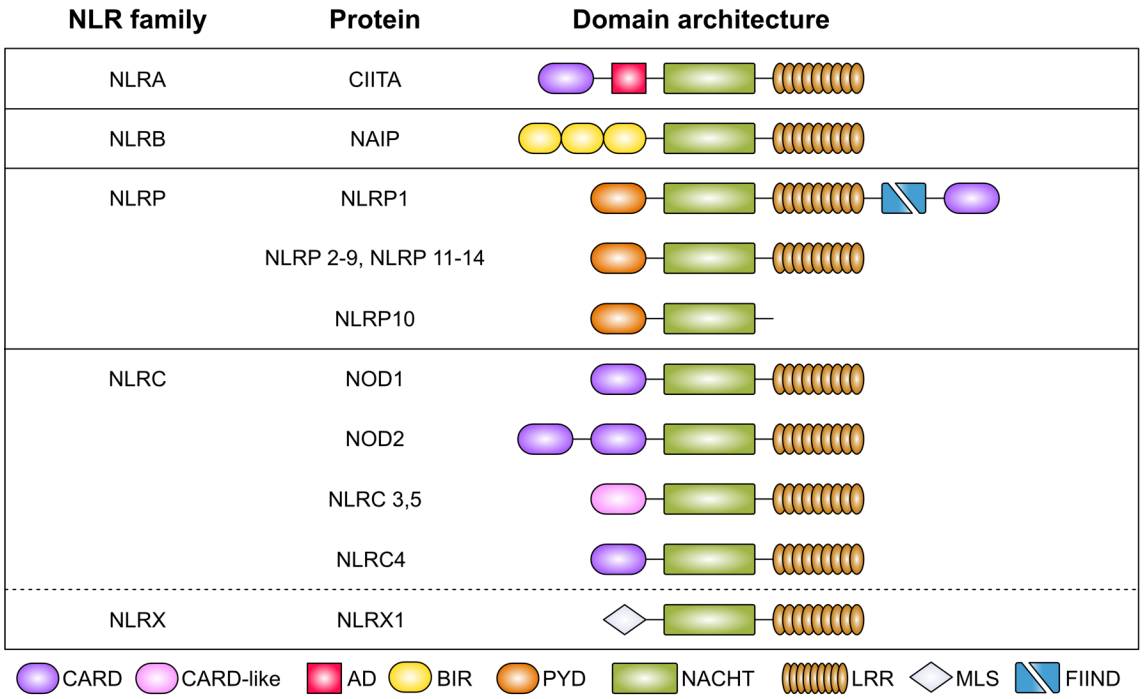

Figure 1-4: The human NOD-like receptor family.
Overview of all 22 human NOD-like receptors (NLRs) divided into four subfamilies: NLRA, NLRB, NLRP, and NLRC+NLRX. They all share a tripartite domain architecture with an N-terminal effector domain, a central NACHT domain, and a C-terminal LRR domain. CIITA: Class II, major histocompatibility complex, trans activator, NAIP: NLR Family Apoptosis Inhibitory Protein, NOD: nucleotide-binding oligomerization domain, CARD: caspase activation and recruitment domain, AD: acidic transactivation domain, NACHT: acronym for NAIP, CIITA, HET-E, and TP1, LRR: leucine-rich repeat, BIR: baculovirus inhibitor of apoptosis protein repeat, PYD: pyrin domain, FIIND: function-to-find domain, MLS: mitochondrial localization signal.

The **C-terminal LRR domain** is mainly responsible for ligand sensing or autoinhibition of NLRs. In NOD1 and NOD2 this region is capable of sensing the bacterial peptidoglycan fragments γ-d-glutamyl-meso-diaminopimelic acid (iE-DAP) and muramyl dipeptide (MDP) and subsequently leads to CARD-CARD interactions which mediate signal transduction (Strober et al., 2006). The LRR domain of NAIP recognizes flagellin and leads to NLRC4 inflammasome formation (Gram et al., 2020). In addition, the LRR domain was shown to keep NOD2 and NLRC4 in an autoinhibited state to prevent self-oligomerization and autoactivation (Hu et al., 2013; Maekawa et al., 2016).

NLRP1 and NLRP10 show a distinct architecture regarding the C-terminus. NLRP1 contains an additional function-to-find domain (FIIND) and a CARD domain. The FIIND domain is divided into the Zu5 (zone undefined 5) and UPA (ubiquitin-like protein associated) subdomains that undergo autolytic cleavage. NLRP1 activation is dependent on this cleavage, but dipeptidyl peptidase 9 (DPP9) is responsible for maintaining the integrity of these components. Degradation of the inhibitory N-terminus leads to the release of the inflammasome-forming UPA-CARD fragment and subsequent ASC recruitment (Chui et al., 2019; Hollingsworth et al., 2021). NLRP10 lacks the C-terminal LRR, so its activation mechanism is likely different. The typical ligand sensing motif is absent, suggesting a unique ligand sensing mechanism. Recent studies have shown that activation of the NLRP10 inflammasome is related to mitochondrial damage, possibly induced by display of molecular entities, such as the negatively charged inner mitochondrial membrane (Próchnicki et al., 2023; D. Zheng et al., 2023).

1.3 The inflammasome – NLRP3, a key member of inflammatory immune response

An inflammasome is a multi-protein complex that plays an important role in the innate immune response by acting as a key mediator of inflammation. In 2002, Jürg Tschopp's group first described it as a caspase-activating complex mediated by the NLRP1 inflammasome (Martinon et al., 2002). Inflammasomes form in response to pathogenic microorganisms, stress signals, or cellular damage. They activate inflammatory processes by promoting the maturation and release of pro-inflammatory cytokines, especially interleukin-1β (IL-1β) and interleukin-18 (IL-18). Nowadays, several receptors are described to form different forms of inflammasomes. Within the NLR protein family NLRP1, NLRP3, NLRP6 and NLRC4 were found to act as inflammasome sensors, activated by a large variety of triggers (Ghimire et al., 2020; Matico et al., 2024; Mi et al., 2022; Swanson et al., 2019). Beside this class of receptors, also AIM2 and Pyrin were found to form inflammasomes to mediate the inflammatory immune response (Rathinam et al., 2010; Schnappauf et al., 2019).

The current model of inflammasome formation is characterized by two individual steps, **priming** and **activation**. These steps are best described for the NLRP3-mediated inflammasome (**Figure 1-5**) (Swanson et al., 2019; Weber et al., 2025).

The **priming** step includes different signals induced by other PRRs (TLRs or NOD2) or cytokine receptors (TNFR or IL-1R1). These signals lead to the upregulation of nuclear factor-κB (NF-κB), the transcription factors pro-IL-1β and pro-IL-18, and the sensor protein e.g., NLRP3 (Bauernfeind et al., 2009). The priming process additionally activates important enzymes for post-translational modifications (PTMs), such as phosphorylation, ubiquitination, palmitoylation, that are indispensable for the inflammasome complex assembly (O'Keefe et al., 2024).

The **activation** step triggers a conformational change from the inactive to the active state with subsequent self-oligomerization into a disc-like structure (Xiao et al., 2023). These structures form a platform to recruit the adaptor protein ASC via homotypic death domain interactions. ASC consists of two death domains, PYD and CARD, and is therefore able to oligomerize either via PYD-PYD or CARD-CARD interactions to form large filaments (ASC specks) (Hochheiser, Behrmann, et al., 2022). Furthermore, these filaments are able to recruit pro-caspase-1 via CARD-CARD interactions leading to a proximity-induced proteolytic cleavage into the subunits p20 and p10 and thus active caspase-1. The active caspase cleaves pro-inflammatory cytokines (pro-IL-1β and pro-IL-18) into their mature active forms, as well as cleaving GSDMD into its N- and C-termini. The N-terminus of GSDMD inserts into membranes and forms large pores that mediate pyroptosis. The C-terminus acts as a negative regulator, preventing pore formation by the N-terminus in the uncleaved state (Broz et al., 2020; Kopp et al., 2023; Swanson et al., 2019).

Inflammasomes are essential for host defense, but their dysregulation has been implicated in various diseases, including autoimmune diseases, neurodegenerative conditions, and metabolic syndromes. Therefore, understanding the function and regulation of inflammasomes is crucial for developing new therapeutic approaches for targeting inflammation-related diseases.

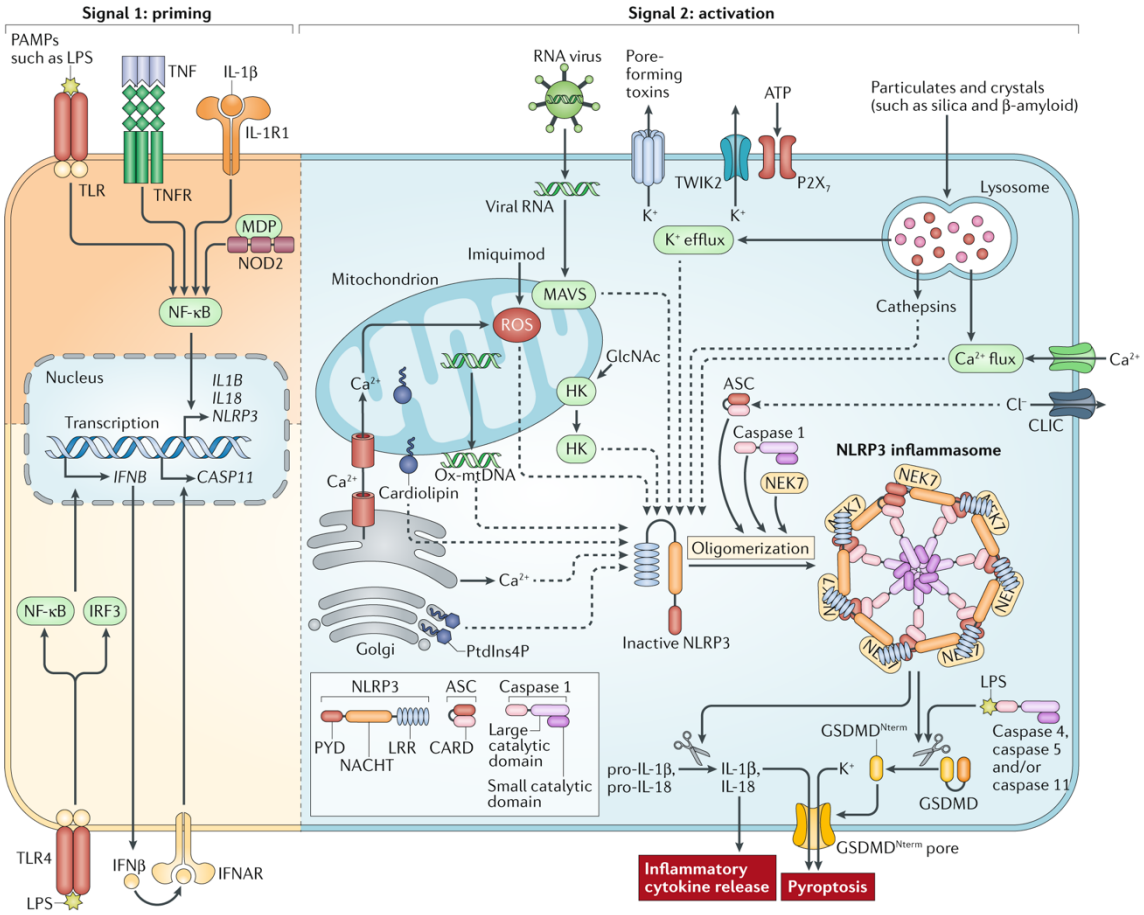

Figure 1-5: Model of NLRP3 inflammasome formation.
The NLRP3 inflammasome formation follows a two-step mechanism including signal 1 (priming) and signal 2 (activation). The priming step is mediated PAMPs or cytokines, leading to the transcriptional upregulation of canonical and non-canonical NLRP3 inflammasome components. Signal 2 (activation) is provided by any of numerous PAMPs or DAMPs, such as particulates, crystals and ATP, that activate multiple upstream signaling events. These include K^+ efflux, Ca^+ flux, lysosomal disruption, mitochondrial reactive oxygen species (mtROS) production, the relocalization of cardiolipin to the outer mitochondrial membrane and the release of oxidized mitochondrial DNA (Ox-mtDNA), followed by Cl^- efflux. RNA viruses activate NLRP3 through mitochondrial antiviral signaling protein (MAVS) on the mitochondrial outer membrane. Formation of the inflammasome activates caspase 1, which in turn cleaves pro-IL-1β and pro-IL-18. Gasdermin D (GSDMD) is also cleaved and inserts into the membrane, forming pores and inducing pyroptosis. Upon detection of cytosolic lipopolysaccharide (LPS), caspases 4, 5 and 11 are activated and cleave GSDMD, triggering pyroptosis. CARD, caspase recruitment domain; CLIC, chloride intracellular channel protein; GlcNAc, N-acetylglucosamine; $GSDMD^{Nterm}$, GSDMD amino-terminal cell death domain; HK, hexokinase; IFNAR, IFNα/β receptor; IL-1R1, IL-1 receptor type 1; IRF3, interferon regulatory factor 3; LRR, leucine-rich repeat; MDP, muramyl dipeptide; NEK7, NIMA-related kinase 7; NF-κB, nuclear factor-κB; P2X7, P2X purinoceptor 7; PtdIns4P, phosphatidylinositol-4-phosphate; PYD, pyrin domain; ROS, reactive oxygen species; TLR, Toll-like receptor; TNF, tumor necrosis factor; TNFR, tumor necrosis factor receptor; TWIK2, two-pore domain weak inwardly rectifying K^+ channel 2 (Swanson et al., 2019).

1.4 AAA+ ATPase proteins – Function of the nucleotide binding domain NBD

The family of NOD-like receptors is characterized by the central NOD domain (Inohara & Nuñez, 2001) that is a central feature in signal transduction ATPases with numerous domains (STAND), first described in 2004 by the group of L. Aravind (Leipe et al., 2004). This class of ATPases is widely distributed within all domains of life, such as bacteria, eucaryotes, and plants (Leipe et al., 2004). Prominent members of this class in the human NLR family are NOD2, NLRP1, or NLRP3, that are mainly involved in inflammatory processes (Danot et al., 2009). Apoptosis-related receptors, including Apaf-1 or CED-4, also belong to the STAND protein class (Ruan et al., 2025; Zou et al., 1997). The bacterial MalT family, involved in transcriptional regulation, is classified as part of the STAND protein family (Marquenet & Richet, 2010).

Proteins within the STAND-family ATPases are involved in many different biological processes depending on their overall architecture. Several different domains were characterized that fulfill certain interactions, such as sensory and effector domains. (**Figure 1-6a**). These domains regulate the mode of action of these receptors. The C-terminal sensory and, in some cases, the effector domains are separated by a spacer (arm), later named HD2 (**Figure 1-6a**). The central NOD domain includes the NBD, HD1, and WHD domains. NBD and HD1 form the active AAA+ (ATPases associated with diverse cellular activities) core, whereas WHD acts as a regulatory domain (Danot et al., 2009).

The NBD core forms a highly-conserved five-stranded α-β-α fold and is characterized by a 5-1-4-3-2 order of the central parallel β-sheets (**Figure 1-6b**). Not just one, but multiple motifs together form the ATPase active site in STAND proteins. The Walker A motif (P-loop) is located at the tip of β1 with a conserved sequence of GxxxxGK(S/T) ('x' denotes for any amino acid). The Walker B motif is located at the tip of β3 with a conserved sequence of hhhhDE ('h' denotes for hydrophobic amino acids). These two motifs are crucial for nucleotide binding and hydrolysis by coordinating the β- and γ-phosphates of ATP and the catalyzing magnesium ion (**Figure 1-6b**) (Danot et al., 2009; Leipe et al., 2004).

Other conserved motifs include glutamate switch (Glu-switch), sensor 1, arginine finger (Arg-finger) and sensor 2. The Glu-switch contains a conserved asparagine residue at the end of β2, which is able to interact with the glutamate in the Walker B motif and thereby regulates ATP hydrolysis. Upon ligand binding, this interaction is interrupted and hydrolysis can take place. At the tip of β4, a polar residue (sensor 1) is located to support the coordination of the nucleotide. The Arg-finger is located on α4 and interacts with the γ-phosphate of the nucleotide bound in a neighboring subunit. Sensor 2 is located in HD1 and includes a highly-conserved proline, that interacts with the nucleotide. In the WHD domain, a conserved histidine at the tip of β8 interacts with the β-phosphate of the bound nucleotide, leading to an autoinhibited state (Danot et al., 2009; Jessop et al., 2021; Marquenet & Richet, 2010; Wendler et al., 2012).

Activation of nucleotide hydrolysis induces the oligomerization into ring-like structures, mostly hexameric assemblies, to induce subsequent signaling cascades. During this process, a nucleotide exchange takes place (Wendler et al., 2012).

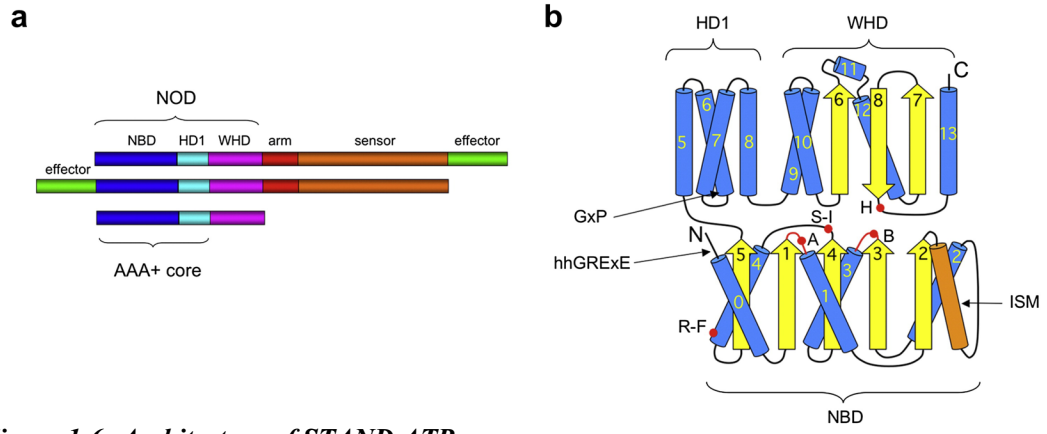

Figure 1-6: Architecture of STAND ATPases.
*(**a**) Domain architecture of STAND proteins. The NOD domain includes NBD, HD1, and WHD. The AAA+ core includes NBD and HD1. (**b**) Topology of the NOD module with conserved features. ISM, initiator-specific motif, a motif specific for the STAND class and the AAA+ initiator clade, which comprises the Orc1/Cdc6 subclade; A, Walker A box; B, Walker B box; S-I, sensor I; R-F, arginine finger; H, WHD conserved histidine (Danot et al., 2009).*

Within the NLR protein family a more specific motif for Walker A and Walker B was characterized, compared to other STAND proteins. The Walker A amino acid sequence includes an additional conserved glycine residue GxxGxGK(S/T) ('x' denotes for any amino acid). Regarding Walker B, the motif occurs in an extended manner with the sequence hhhhDGhDE ('h' denotes for hydrophobic amino acids), involving another acidic residue involved in nucleotide hydrolysis (**Figure 1-7**) (Brinkschulte et al., 2022; Sandall et al., 2020b).

The exact mechanism of nucleotide hydrolysis is an ongoing area of research, but its role in activating and regulating STAND-class proteins is undeniable (Danot et al., 2009).

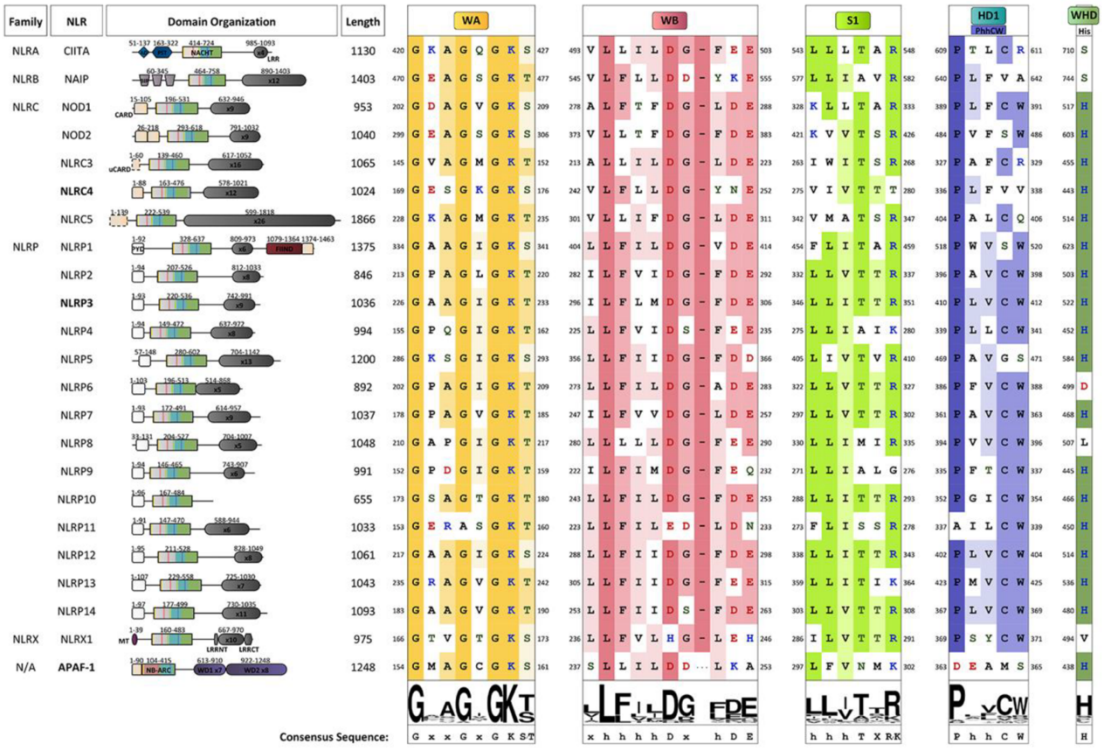

Figure 1-7: Sequence alignment of nucleotide binding features in NLR family.
Multiple sequence alignment of conserved features critical for catalytic activity in the 22 NLR proteins and APAF-1 NBD motifs. The NLR family members are subdivided based on the presence of one of four N-terminal effector domains. The consensus sequence is shown (Sandall et al., 2020b).

1.5 Aims of the thesis

The role of NOD-like receptors in innate immunity is the subject of ongoing scientific research. A better understanding of the underlying mechanisms of regulation and activation could advance our knowledge of NOD-like receptor signaling in innate immunity. The precise cellular and structural mechanisms are poorly understood.

For the nucleotide-binding and oligomerization domain-containing protein 2 (NOD2) a crystal structure was published in 2016 from the organism *Oryctolagus cuniculus (rabbit)* (Maekawa et al., 2016). Even though the sequence similarity and identity between rabbit and human are high, it is important to determine the structure of *human*NOD2, to be able to understand the mechanism in humans and to develop specific drugs targeting *human*NOD2. Based on these results new approaches will be conducted to get insights into the structure of *human*NOD2. Either X-ray crystallography or cryo-electron microscopy should be conducted. For that purpose, *human*NOD2 will be expressed in *Sf9* insect cells without the tandem CARDs to prevent self-oligomerization.

NLRP12 is a poorly studied member of the NLRP subfamily, of great interest due to its close relationship with NLRP3. Previous studies have shown that it acts as either a positive or negative regulator of innate immune signaling (Tuladhar & Kanneganti, 2020; Vladimer et al., 2012). Therefore, a better understanding of how NLRP12 functions is crucial. NLRP12 and NLRP3 are most closely related in the phylogenetic tree and have a high degree of sequence similarity. The PYD structure of NLRP12 was first described in 2011 by NMR spectroscopy (Pinheiro et al., 2011). However, the information on the full-length NLRP12 structure would provide more details into its mechanism of action and could help understanding the function and regulation of NLRP12 in inflammation.

Based on recent research in our institute regarding the crystal structure of the NACHT domain and cryo-EM structure of full-length NLRP3, the aim is to transfer that knowledge to NLRP12 and use X-ray crystallography for structure determination. Small molecule inhibitors could play an important role in this approach. Different compounds, known from NLRP3 research (Coll et al., 2015; Keuler et al., 2022), will be tested in direct binding assays to find inhibitors targeting NLRP12. Additionally, the off-target effect of NLRP3 inhibitors will be screened, as NLRP12 could be a possible low-affinity off-target. Furthermore, generation of NLRP12 specific Nanobodies will be performed, to use them as a crystallization tools.

NLRP10 is receiving increasingly more attention due to its unique architecture within the NLRP family. Recent studies have shown NLRP10's inflammatory response to mitochondrial damage (Próchnicki et al., 2023; D. Zheng et al., 2023), but its activation mechanism is still unknown. The same applies for the protein structure, where again just the PYD structure was solved via NMR spectroscopy (Su et al., 2013). NLR proteins have been shown to oligomerize in different oligomeric states. Also, these assemblies can differ between different species as shown for NLRP3. The aim of this third project is to characterize NLRP10 with regards to its oligomeric states and to understand how oligomerization affects the functions of NLRP10. As one of the properties of NLRs, the ATP hydrolysis function of NLRP10 will be investigated in HPLC ATP hydrolysis assays.

Within this doctoral thesis, the function and role in innate immunity of three different NLR proteins is investigated. This knowledge contributes to a better understanding of the regulatory mechanisms of NOD2, NLRP12, and NLRP10 for further structural and mechanistic research.

2. Biochemical and structural studies of human NOD2

Parts of the here presented work were carried out with other members of the Institute of Structural Biology (University of Bonn). Dr. Michael Marleaux performed the initial molecular biology work, protein purification and SPR measurements. Dr. Inga Hochheiser helped with negative stain electron microscopy sample preparation, grid preparation and imaging at the facility for electron microscopy at the Max Planck Institute for Neurobiology of Behavior – Caesar (Bonn). Later on, this was done in cooperation with Carola Tröger in the group of Dr. Stephan Irsen. Grid preparation for cryo-electron microscopy was performed with Dr. Monika Gunkel at the StruBiTEM facility (University of Cologne). Measurements were performed at the Ernst Ruska Center for microscopy and spectroscopy with electrons (Forschungszentrum Jülich) with the help of Dr. Thomas Heidler. All mass spectrometry analyses were provided by the group of Prof. Dr. Henning Urlaub at the Max Planck Institute for Multidisciplinary Sciences in Göttingen.

2.1 Evolutionary and functional background of human NOD2

NOD2 was first described in 2001 as an NF-κB activator (Ogura et al., 2001) and as an important receptor in the immunology of Crohn's Disease (CD) (J. H. Cho, 2001). It is an intracellular pattern recognition receptor and a sensor of peptidoglycans through the recognition of muramyl dipeptide (MDP) (Girardin et al., 2003; Inohara et al., 2003). NOD2 recruits the receptor-interacting serine/threonine kinase (RIPK2; RICK) via CARD-CARD interactions. Activation of RIPK2 leads to K63 (Lys63)-linked polyubiquitylation of the IKK (inhibitor of κB kinase) complex and subsequent phosphorylation of Iκβ leads to NF-κB release. NOD1 and NOD2 are mainly expressed by two different cell types: antigen-presenting cells (APCs), including macrophages and dendritic cells, and epithelial cells (Strober et al., 2006).

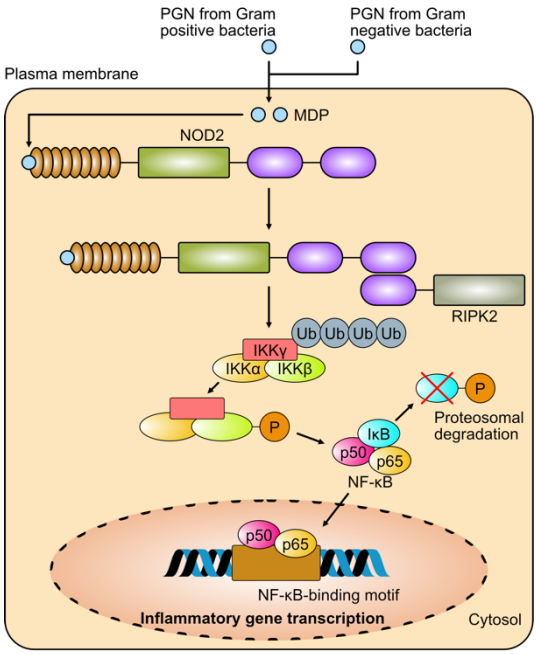

Figure 2-1: Signaling pathway of NOD2. *Muramyl dipeptide (MDP) from gram-positive or negative bacteria is recognized by the leucine-rich repeat (LRR) domain of NOD2 and leads to activation and thereby recruitment of receptor-interacting serine/threonine kinase (RIPK2) through caspase-recruitment domain (CARD)-CARD interactions. This recruitment activates RIPK2 leading to K63 (Lys63)-linked polyubiquitylation of IKKγ. Followed by this, IKKβ, part of the IKK complex, is phosphorylated and subsequently the inhibitor Iκβ is also phosphorylated and degraded. The released nuclear factor-κB (NF-κB) (p50, p65) migrates to the nucleus and binds to DNA motifs to mediate transcription of specific genes. This figure was modified from (Strober et al., 2006).*

Besides being involved in Crohns disease, NOD2 was also found to be associated with the inflammatory diseases Blau syndrome (BS) and early onset sarcoidosis (EOS). Either loss-of-function (CD) or gain-of-function (BS/EOS) mutations were observed resulting in dysregulated inflammation (Borzutzky et al., 2010; Caruso et al., 2014; Strober & Watanabe, 2011).

Although the activation of NOD2 by MDP is an extensively studied process, the underlying mechanism remains elusive. Prior to activation, NOD2 is located in the cytoplasm in an inactive ADP bound state, where the LRR domain shields the NBD. Upon MDP recognition by the LRR domain, NOD2 adapts an open conformation that allows nucleotide exchange and hydrolysis, and thereby activates RIPK2 (Heim et al., 2019; Zurek et al., 2010). In 2012, Grimes et al. demonstrated the direct binding of MDP to NOD2 using surface plasmon resonance (SPR) measurements (Grimes et al., 2012). More recently, an investigation revealed that MDP phosphorylation by a specific kinase is necessary for NOD2 activation (Stafford et al., 2022).

To better understand the underlying mechanism, structural data would be of great interest to elucidate the binding pocket in NOD2 for MDP, as well as the activation mechanism, induced through this binding.

2.2 Domain architecture and functional motifs in human NOD2

Human NOD2 (hNOD2) protein contains 1,040 amino acids resulting in a molecular mass of 115.2 kDa. There are three isoforms known for hNOD2 where isoform one has been defined as the canonical sequence (Uniprot: Q9HC29-1). The coding gene for hNOD2 (*hNod2*) is located on the forward strand of chromosome 16 and contains 12 coding exons. The following gene synonyms are also used: BLAU, CARD15, CD, CLR16.3, IBD1, NLRC2, PSORAS1 (Ensemble: ENSG00000167207.15).

The structure of hNOD2 is yet to be discovered, but a crystal structure (PDB: 5IRN) of rabbit (*Oryctolagus cuniculus, Oc*) NOD2 (*Oc*NOD2) was solved lacking CARD domains (ΔCARDs construct) and two surface exposed loops (Maekawa et al., 2016).

The hNOD2 protein is composed of different domains. Immediately at the N-terminus, a 25 amino acids tail is present, followed by two caspase recruitment domains (tandem-CARDs) (aa 25-124, aa 125-214), that are involved in the interaction with downstream effector proteins like RIPK2 via CARD-CARD interactions and thereby triggering inflammatory signaling (Strober et al., 2006). The FISNA (fish-specific NACHT-associated) domain (aa 215-289) serves as a connection between tandem-CARDs and the NACHT domain. In NLRP3 the FISNA domain contains a polybasic region and was found to induce a conformational change activated by potassium efflux (Tapia-Abellán et al., 2021). The central NACHT domain (aa 290-763) is responsible for ATP-dependent oligomerization facilitated by conformational changes (Mo et al., 2012). In the NBD (aa 290-445) the well-conserved Walker A and extended Walker B motifs for nucleotide binding can be found. The NBD is followed by three helical domains, HD1 (aa 446-504), WHD (aa 505-621) and HD2 (aa 622-763). These domains contain important sensors for nucleotide binding and hydrolysis. The C-terminal ligand sensing LRR domain (aa 764-1040) forms a horseshoe-like structure as typical for this fold (**Figure 2-2**).

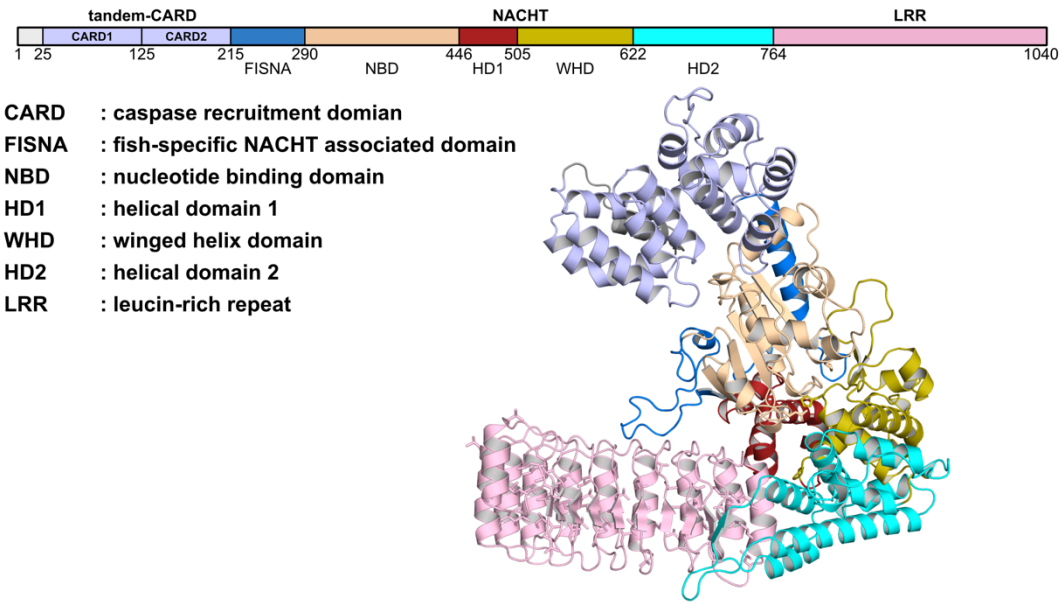

Figure 2-2: Domain architecture of human NOD2.
AlphaFold2 model (Jumper et al., 2021) of human NOD2 with colorized domains and corresponding domain boundaries. The different domains are indicated.

2.3 Characterization of recombinantly expressed NOD2

To investigate human NOD2, it was recombinantly expressed in the *Sf9* insect cell system. Initial purification of N-terminally MBP-tagged wild-type NOD2 (1-1061, $NOD2^{wt}$) by affinity chromatography and subsequent size-exclusion chromatography (SEC) revealed oligomerized and/or aggregated sample eluting in the void volume fraction (**Figure 2-3a**). It was expected that the CARD domains caused this behavior. Thus, a construct without the CARD domains (hNOD2ΔCARDs (215-1040)) was cloned and expressed. Following affinity and overnight TEV cleavage, a SEC was performed and indeed it showed different species (**Figure 2-3b**). Besides the void volume fraction (black), four other species were observed: uncleaved NOD2ΔCARDs (red), cleaved NOD2ΔCARDs (blue), MBP (green), and an unknown oligomeric species (yellow). Protein quality was validated by SDS-PAGE analysis (**Figure 2-3c**). The oligomeric species appeared at the same molecular weight as cleaved NOD2ΔCARDs (~95 kDa). The oligomeric species (yellow) and the monomeric (referring to elution volume) NOD2ΔCARDs species (blue) were analyzed by negative stain electron microscopy. The oligomer showed well distributed round-shaped particles (yellow), whereas the monomer fraction contained small inhomogeneous particles with no apparent symmetry (blue) (**Figure 2-3d**).

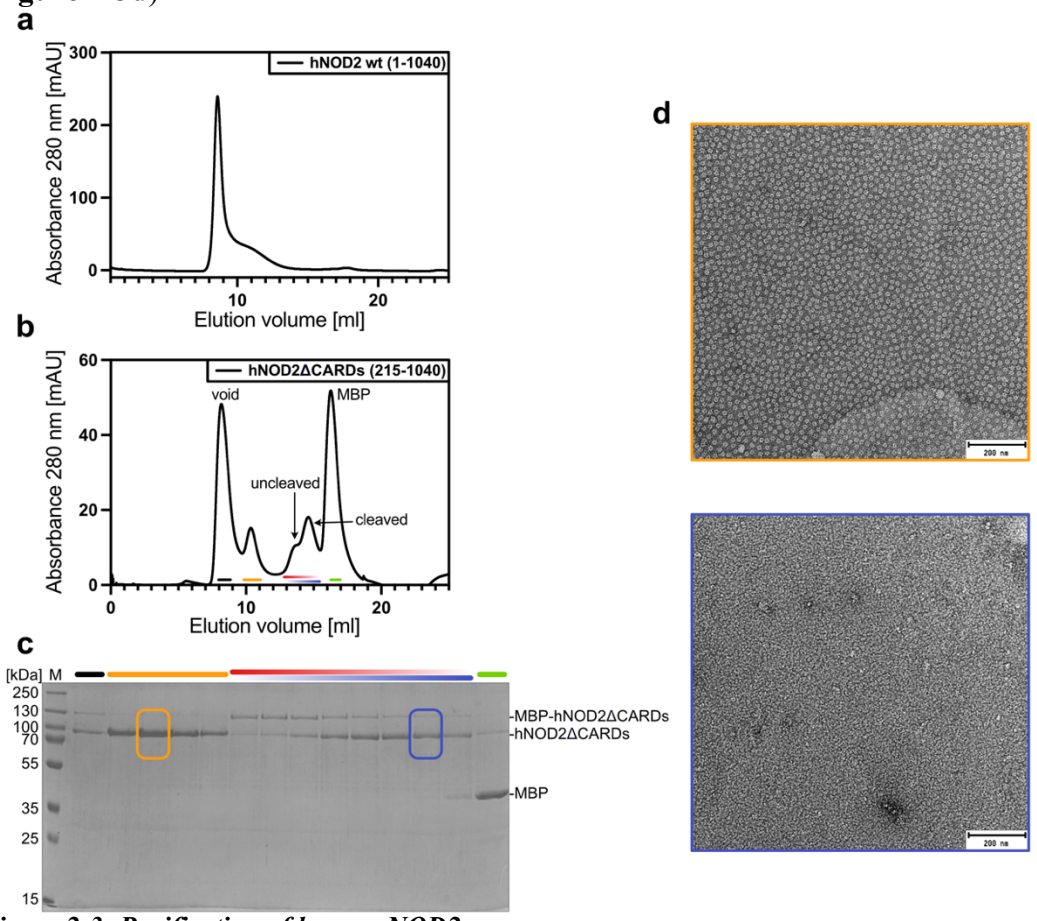

Figure 2-3: Purification of human NOD2.
*(**a**) Chromatogram of $NOD2^{wt}$ injected onto a Superose 6 Increase 10/300 column after affinity purification. The peak at 8 ml elution volume shows $NOD2^{wt}$ sample. The x-axis shows the retention volume in ml and the y-axis the UV absorption at 280 nm in mAU. (**b**) Chromatogram of hNOD2ΔCARDs injected on a Superdex 200 Increase 10/300 column after affinity purification and overnight TEV cleavage. The peaks show different species indicated by different colors. The x-axis shows the retention volume in ml and the y-axis the UV absorption at 280 nm in mAU. (**c**) Coomassie-stained SDS-PAGE analysis with samples from (b), M: marker, samples according to colors. (**d**) Negative stain EM analysis of samples from (b).*

2.4 Identification of VCP as a specific interaction partner

To further analyze the unknown oligomeric species, a different approach was conducted. No TEV cleavage was performed after affinity chromatography, instead the SEC analysis was done immediately. Here, the chromatogram shows three species: void volume (black), oligomer (yellow), and MBP-hNOD2ΔCARDs (215-1040) monomer (green). The corresponding SDS-PAGE analysis revealed two different proteins present in the oligomeric species. The band at ~130 kDa refers to MBP-hNOD2ΔCARDs (215-1040) with a calculated mass of 132.7 kDa, whereas the band at ~95 kDa corresponds to a still unknown protein (**Figure 2-4a**). The stability of the protein complex (yellow) was tested by a second SEC with the pooled sample from run 1 (yellow fractions). In general, the chromatogram showed a similar pattern and the SDS-PAGE analysis revealed the same complex. It was observed that the unknown band appears to be slightly stronger than the band corresponding to NOD2 (**Figure 2-4b**).

In earlier studies by Ghalandary et al. (2022), a protein regulating the inflammatory NOD2 response was identified. This protein is an ATPase family member called valosin-containing protein (VCP), also known to segregate protein molecules from large cellular structures (Ghalandary et al., 2022). To confirm whether VCP was present in the purification of NOD2, a western blot analysis was performed using an α-VCP antibody. In fact, VCP was observed in the oligomeric fraction of either cleaved or uncleaved NOD2 purification (**Figure 2-4c**). In addition, the presence of VCP was confirmed by peptide mass fingerprint analysis. The oligomeric fractions indeed identified VCP, whereas the monomeric fractions referred to NOD2 (**Figure 7-1**).

Size determination was conducted using a SEC-MALS measurement. For this purpose, the oligomeric species was collected and applied to a HPLC for the measurement. The observed molecular weight was 520 kDa, which is suitable for a hexameric assembly of either VCP or NOD2 alone, or as a hetero-oligomeric complex (**Figure 2-4d**). VCP has been described to form hexameric assemblies and numerous structures were determined by cryo-EM or X-ray crystallography (Banerjee et al., 2016; Tang & Xia, 2016). As the expression of NOD2 was done in *Sf9* insect cells with infecting the cells only with the virus encoding for NOD2, the VCP present in the sample was endogenous. Thus, an AlphaFold prediction of VCP (*Sf9*) was performed, leading to a hexameric assembly as well (**Figure 2-4e**). At this point, it was not possible to confirm, whether the observed assemblies in the negative stain image consisted of VCP, NOD2, or both.

To test if VCP is upregulated upon infection of *Sf9* cells with virus expressing NOD2, western blot analysis was performed before and after infection. The blot revealed that there was no change in the level of endogenously expressed VCP upon NOD2 expression (**Figure 2-4f**). This indicates, that recombinantly expressed human NOD2 specifically pulled down endogenously expressed VCP from *Sf9* insect cells in high amount. This points to a strong interaction and is in line with previous findings (Ghalandary et al., 2022).

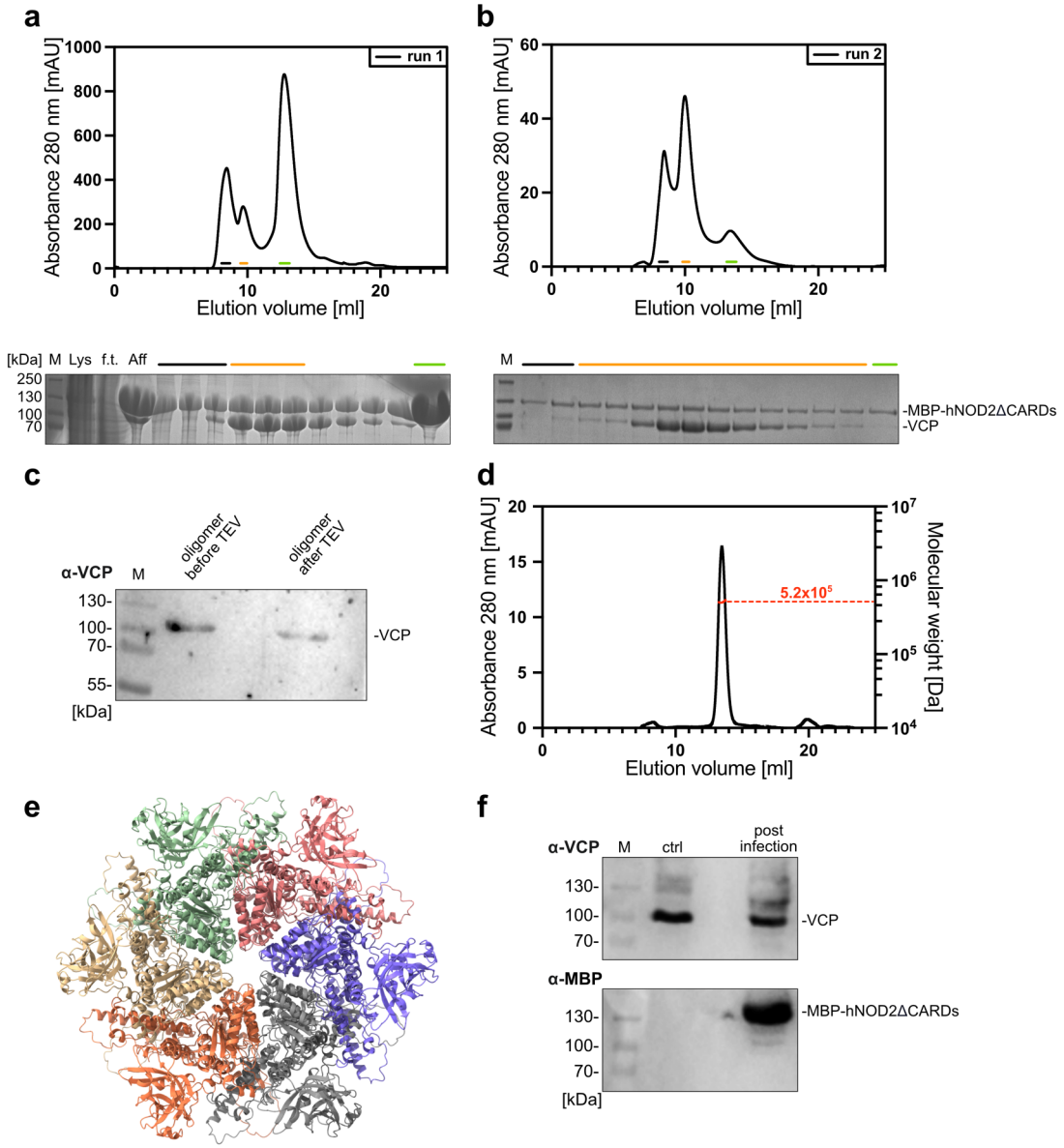

Figure 2-4: Investigation of the oligomeric species in NOD2 purification.
*(**a**) Chromatogram of MBP-hNOD2ΔCARDs injected on a Superdex 200 Increase 10/300 column after affinity purification. The peaks show different species that are indicated. The x-axis shows the retention volume in ml and the y-axis the UV absorption at 280 nm in mAU. Corresponding Coomassie-stained SDS-PAGE analysis is shown below, M: marker, Lys: sample after lysis, f.t.: flow through of affinity chromatogrhaphy, Aff.: sample after affinity chromatography, samples according to colors. (**b**) Chromatogram of the second run of pooled oligomeric fraction from (a), injected on a Superdex 200 Increase 10/300 column. The peaks show different species that are indicated. The x-axis shows the retention volume in ml and the y-axis the UV absorption at 280 nm in mAU. Corresponding Coomassie-stained SDS-PAGE analysis is shown below with indicated samples according to colors. (**c**) Western blot analysis of oligomeric fractions after SEC of either MBP-hNOD2ΔCARDs or hNOD2ΔCARDs with α-VCP antibody. (**d**) SEC-MALS measurement of oligomeric fractions after TEV cleavage during hNOD2ΔCARDs purification using a Superose 6 Increase 10/300 column. The molecular weight is indicated in red. The x-axis shows the retention volume in ml, the left y-axis the UV absorption at 280 nm in mAU, and the right y-axis the molecular weight in Da. (**e**) Structure prediction of a VCP(Sf9) hexamer using the AlphaFold3 server (Abramson et al., 2024). (**f**) Western blot analysis of uninfected (ctrl) and infected Sf9 cells using α-VCP and α-MBP antibody.*

2.5 Structural research of the NOD2-VCP complex

Previously performed negative stain EM revealed homogeneous particles suitable for further structure determination. A tag-cleaved sample taken from the NOD2 purification was applied to either carbon or gold grids at a concentration of 1.4 mg/ml. The screening process revealed better particle distribution on carbon grids than on gold grids, although the particles tended to be located on or near the carbon surface. In total, 1,197 micrographs were collected and further analyzed with the cryo-EM data analysis software CryoSPARC. In the end, a 3D volume representing a hexameric structure was observed at a resolution of 3.5 Å (**Figure 2-5**).

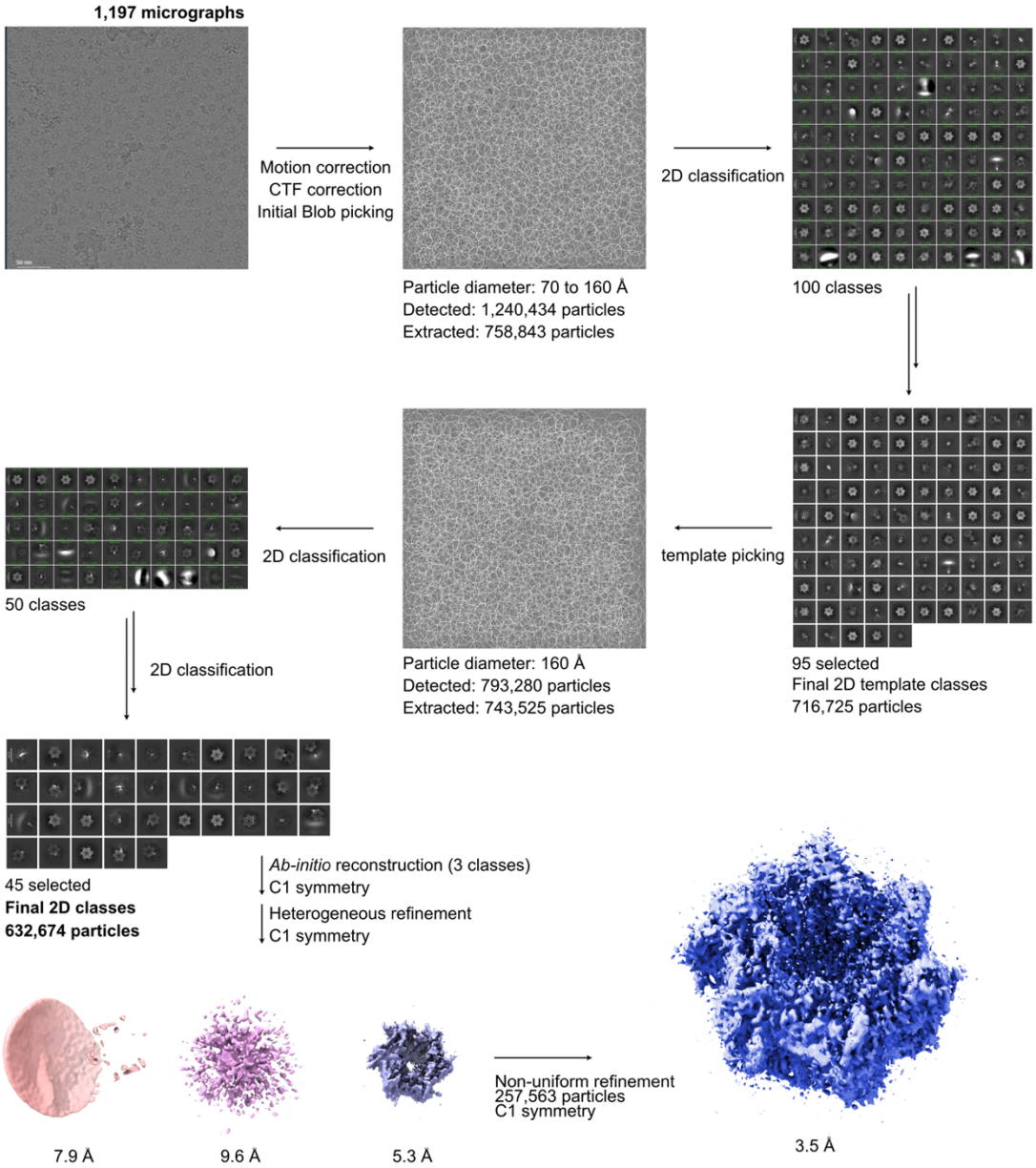

Figure 2-5: Cryo-EM data analysis.
The workflow for analyzing cryo-EM data was performed using CryoSPARC. A total of 1,197 micrographs were analyzed. After motion and CTF correction and initial blob picking, 1,240,434 particles with diameters between 70 and 160 Å were obtained. Several rounds of 2D classifications resulted in 95 selected 2D classes including 716,725 particles. Subsequent template picking with a particle diameter of 160 Å led to 743,525 extracted particles. Again, after several rounds of 2D classifications, finally 632,674 particles were extracted and used for Ab-initio reconstruction in 3 classes (C1) and heterogeneous refinement (C1). Lastly, a non-uniform refinement (C1) was performed with 257,563 particles and resulted in a final resolution of 3.5 Å.

The observed 3D volume revealed differences in resolution, prompting an orientation diagnostic analysis. This analysis indicated resolutions ranging from 3 to 13 Å from different angles (**Figure 2-6a**). This result hints at a preferred orientation problem with the given protein sample and used grid type. The AlphaFold3 prediction of VCP (*Sf9*) aligns well with the 3D volume (**Figure 2-6b**). A detailed view from either the side or the top of the hexamer reveals a higher density on one side (**Figure 2-6c**). This asymmetry could indicate the presence of NOD2 attached to VCP. However, the resolution was not sufficient to resolve any details and needs optimization.

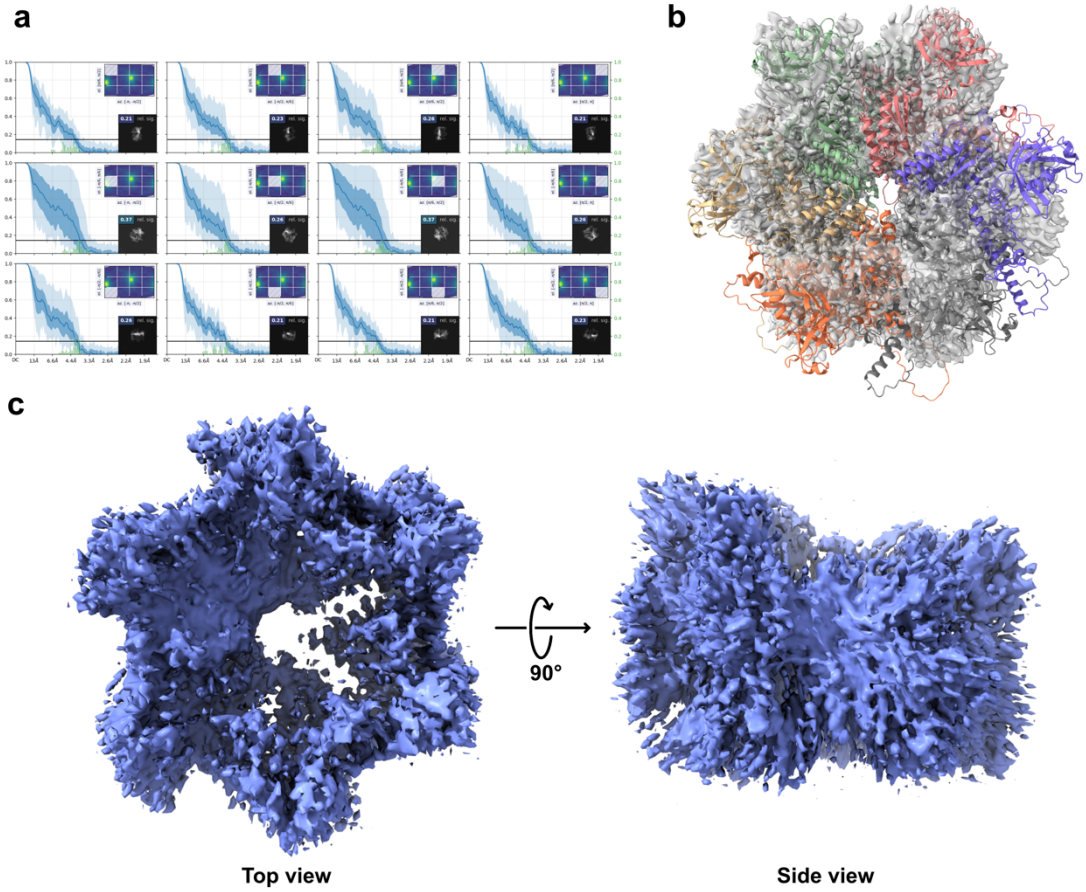

Figure 2-6: Structure analysis of cryo EM data of NOD2-VCP.
*(**a**) Orientation diagnostic analysis of the final 3D volume created in CryoSPARC. Different angles show different resolutions from 3 to 13 Å. (**b**) Alignment of the AlphaFold3 prediction of VCP (Sf9) with the resulted volume upon particle analysis. (**c**) Top- and side view of the hexameric EM structure.*

2.6 Discussion and conclusion

The cytosolic pattern recognition receptor NOD2 plays a central role in the host defense against bacterial pathogens. By recognizing muramyl dipeptide (MDP), a conserved motif derived from bacterial peptidoglycan, NOD2 contributes to the activation of NF-κB and MAPK signaling pathways, ultimately driving the production of pro-inflammatory cytokines (Inohara et al., 2003). Although NOD2 is a well-studied receptor, there is currently only one protein structure available, determined by X-ray crystallography. This structure was solved with *rabbit* NOD2 (*Oryctolagus cuniculus*) (Maekawa et al., 2016).

To gain insights into the structure of *human* NOD2, it was recombinantly expressed in *Sf9* insect cells. The full-length protein construct revealed aggregated species, which was most likely caused by the N-terminal tandem CARD domain. Based on the published crystal structure, the CARD domains were removed, and NOD2 could be purified in a defined species corresponding to a monomer. In addition, a defined oligomeric fraction was detected. Negative stain EM analysis revealed well-distributed, round particles for the oligomer, whereas the monomer showed no visible protein structures. Based on the SDS-PAGE analysis, the sample size of 90 kDa indicated that it was a NOD2 oligomer (**Figure 2-3**).

A purification approach without conducting a TEV cleavage led to the result that the oligomer contains a different protein due to the size difference (**Figure 2-4**). Literature research resulted in the possibility of NOD2 binding to valosin-containing protein (VCP) (Ghalandary et al., 2022). Knockdown of VCP in colon carcinoma cells resulted in impaired NF-κB activity and IL-8 expression in response to MDP stimulation. VCP, also known as p97 or TERA, is an essential and evolutionarily conserved member of the AAA+ ATPase family. As an ATP-dependent molecular chaperone, VCP plays a pivotal role in maintaining protein homeostasis by extracting, unfolding, and remodeling proteins in different cellular environments. Structurally, VCP assembles into a ring-shaped homohexameric complex. Each subunit comprises an N-terminal domain, two conserved ATPase domains (D1 and D2), and a short C-terminal tail. The N-terminal domain mediates interactions with numerous cofactors and ubiquitinated substrates. The D1 and D2 domains provide the mechanical force for protein unfolding and extraction by coordinating ATP binding and hydrolysis. This organization allows VCP to function as a dynamic molecular machine, with conformational changes propagating between subunits to drive substrate processing (Caffrey et al., 2021; DeLaBarre & Brunger, 2003; Jiang et al., 2016).

Western blot analysis proved the presence of endogenous VCP that was pulled down during NOD2 purification because it was not intentionally expressed. Additionally, infection of *Sf9* cells with the NOD2 virus did not upregulate VCP. As previously described, VCP assembles into hexameric assemblies, which aligns with the size determined by MALS measurements. The observed mass of 520 kDa corresponded to six subunits. However, it was unclear whether NOD2 was incorporated into this structure. The observation in SDS-PAGE analysis suggested the presence of both proteins in the oligomeric species (**Figure 2-4**).

Cryo-EM analysis was conducted to resolve the structure and gain more information about the subunits incorporated in the assembly. The best data set resulted in a 3D volume with a resolution of 3.5 Å (**Figure 2-5**). Unfortunately, a preferred orientation was observed meaning the resolution differed significantly at certain angles. The overall density fitted well with a AlphaFold3 prediction of VCP from *Spodoptera frugiperda*

(*Sf9*). However, the 3D density appeared to be asymmetrical, both top-down and sideways, which could potentially allow for the binding of NOD2 (**Figure 2-6**). This possibility is not likely, because of the measured mass referring to a hexamer. Therefore, it would be more probable that one or more subunits are exchanged from VCP to NOD2 building a heterogeneous complex.

In summary, the results presented here confirm the previously described connection between NOD2 and VCP. Due to the low resolution of the 3D density, the subunits within the hexameric assembly could not be identified. The physiological relevance of these protein interactions remains to be seen.

3. Characterization of NLRP12 and binding studies with small molecule inhibitors

Parts of the here presented work were carried out with other members of the institute of structural Biology (University of Bonn). Dr. Michael Marleaux performed the initial molecular biology work of NLRP12 and SPR measurements. Crystallization experiments were performed by Dr. Kanchan Anand. Nanobody generation was done in cooperation with the Core Facility Nanobodies (University of Bonn) together with Jan Tödtmann and Wiebke Aderhold in the group of Dr. Stephan Menzel. MCC950 based small molecules were provided by Dr. Tim Keuler in the group of Prof. Michael Gütschow (University of Bonn).

3.1 Human NLRP12 in innate immunity

NLRP12 is a member of the NOD-like receptor family and the closest homolog of the best-characterized receptor, NLRP3. It was first described in 2002 as a regulator of NF-κB activation and caspase-1-dependent cytokine processing (L. Wang et al., 2002). Several studies have implicated NLRP12 as a negative regulator of pro-inflammatory TLR and TNFR signaling by suppressing the canonical and non-canonical NF-κB and MAPK/ERK pathways (L. Huang et al., 2023; Tuladhar & Kanneganti, 2020) (**Figure 3-1**). Contrary, NLRP12 has been shown to be activated during infection with *Yersinia pestis*, *Plasmodium falciparum* and *Plasmodium vivax*, resulting in inflammasome activation and subsequent cytokine release. However, the activation mechanism and the corresponding ligands remain unknown (Ataide et al., 2014; Vladimer et al., 2012) (**Figure 3-1**).

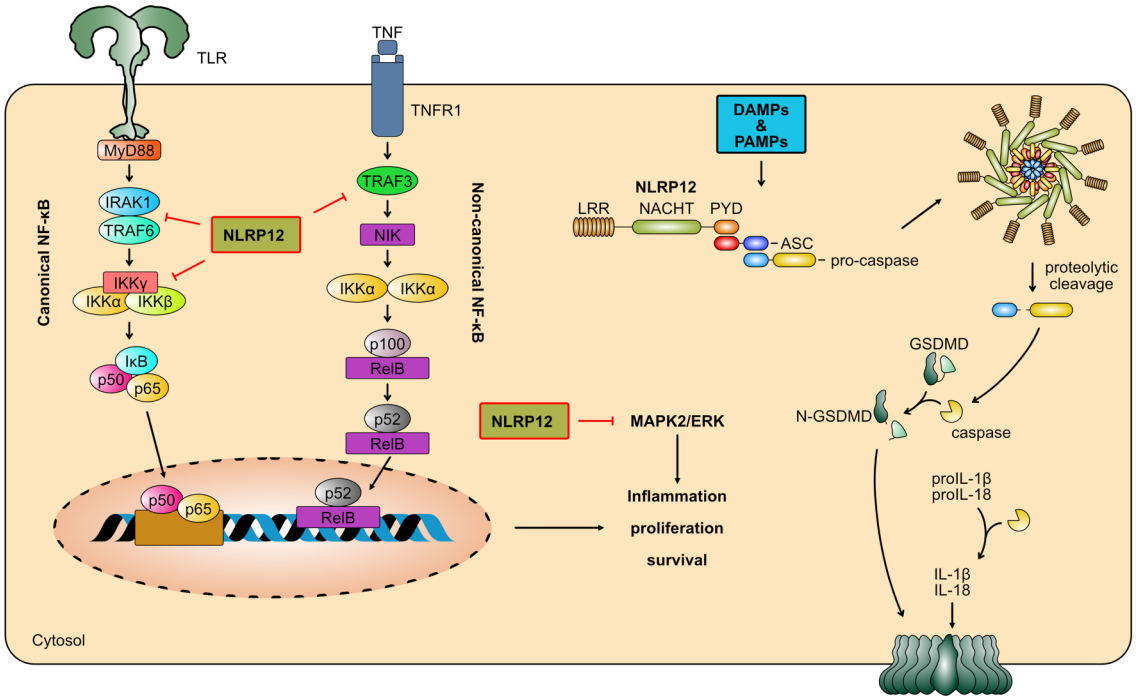

Figure 3-1: Role of NLRP12 in innate immune signaling pathways.
Suppressing effects of NLRP12 in the canonical and non-canonical NF-κB pathways affecting the inflammatory immune response (left). NLRP12 also interferes with the MAPK/ERK pathway (middle). DAMPs and PAMPs trigger inflammasome activation by inducing the association of NLRP12 together with ASC and pro-caspase, resulting in proteolytic caspase cleavage. Active caspase cleaves GSDMD, leading to the formation of membrane pores consisting of GSDMD N-terminus, thereby mediating cytokine release (right). This figure was modified from (L. Huang et al., 2023; Tuladhar & Kanneganti, 2020).

Mutations or dysregulation of the *Nlrp12* gene have been implicated in various inflammatory diseases. NLRP12-associated autoinflammatory disease (NLRP12-AID) is an autosomal dominant systemic autoinflammatory disease (SAID) caused by variants of the *Nlrp12* gene and leads to recurrent fever, arthritis, cutaneous rash, and abdominal pain. Another name for NLRP12-AID is familial cold-induced autoinflammatory syndrome 2 (FCAS2) due to the similar phenotype to FCAS, the mild type of NLRP3-associated autoinflammatory disease (NLRP3-AID) (Miao et al., 2023; Rigante, 2012; H. Wang, 2022). NLRP12 is also involved in other diseases like lung inflammation, multiple sclerosis or Kawasaki disease (Gharagozloo et al., 2018; Y.-H. Huang et al., 2018; Y. Jin et al., 2017).

3.2 Domain architecture and functional motifs in human NLRP12

Human NLRP12 is encoded by the *Nlrp12* gene, located on the reverse strand of chromosome 19. There are seven isoforms described and isoform one has been defined as the canonical sequence (Uniprot: P59046-1). The gene contains 10 coding exons and is also known as: CLR19.3, MONARCH1, NALP12, PAN6, PYPAF7, RNO2 (Ensemble: ENSG00000142405.24). Human NLRP12 is a 1,061 amino acid protein with a molecular weight of 120.2 kDa and a theoretical isoelectric point (pI) of 6.59.

The structural research on NLRP12 is an ongoing matter that has proven to be a challenging task. However, two independent groups published the NLRP12^{PYD} structure determined by NMR spectroscopy and X-ray crystallography (T. Jin et al., 2017; Pinheiro et al., 2011). The structure of the full-length protein remains elusive.

Most of the here presented work is based on the close relationship between NLRP12 and NLRP3. A sequence and structure alignment of the NACHT domains reveals an identity of 55 %, so it is likely that the overall structure of NLRP12 is similar to NLRP3 (**Figure 3-2**).

Figure 3-2: Sequence alignment of NLRP12 and NLRP3.
The amino acid sequences of human NLRP12^{NACHT} (aa 122-679) (Uniprot: P59046) and human NLRP3^{NACHT} (aa 131-694) (Uniprot: Q96P20) were aligned using Clustal Omega (Madeira et al., 2024) and secondary structure assignment was created using ESPript3.0 (Robert & Gouet, 2014). Identical residues are indicated by red filled boxes and similar residues by red letters. Secondary structure elements represent NLRP3 (PDB: 7PZC_A, (Hochheiser, Pilsl, et al., 2022)): α=α-helices, β=β-sheets, η=small helices, TT=strict β-turns.

As almost all other NLRP proteins, NLRP12 is composed of three major building blocks, named PYD, NACHT and LRR. It contains an N-terminal effector pyrin domain (PYD) (aa 1-95), followed by a 24 amino acid linker. The FISNA domain (aa 120-208) similary to NLRP3 is connected to this linker. The polybasic cluster observed in NLRP3, which is involved in inflammasome activation and associated with potassium efflux (Tapia-Abellán et al., 2021), is not present in NLRP12. In NLRP12 there is also a polar cluster containing basic and acidic residues, but its function is not clear. The NACHT domain (aa 209-632), which is highly conserved between NLRP12 and NLRP3 (**Figure 3-2**), builds the central regulatory core accommodating all ATP-hydrolysis features. In the NBD (aa 209-363) the well-conserved Walker A and extended Walker B motifs for nucleotide binding are located. Additionally, sensor 1 and the Arg-finger features are located at the end of the NBD, which is followed by three helical domains, HD1 (aa 364-425), WHD (aa 426-531) and HD2 (aa 532-632). These domains contain important sensors for nucleotide binding and hydrolysis. The C-terminal LRR (aa 772-1061) can be divided into two parts depending on the structure of the different repeats. Compared to NLRP3, the transition LRR (aa 633-771) in NLRP12 is composed of four repeats instead of two, predicted in the AlphaFold2 model (Jumper et al., 2021). Within this domain, a flexible loop (aa 667-698) is located similar to the acidic loop in NLRP3. This acidic loop mediates the contact between two opposing LRRs in an inactive decameric conformation (Hochheiser, Pilsl, et al., 2022). For NLRP12 this loop contains polar residues, but is not as acidic. The canonical part (aa 772-1061) of the LRR in NLRP12 aligns well with the corresponding region in NLRP3, despite the number of repeats being one less in NLRP12. In summary, NLRP12 and NLRP3 share a lot of similarities regarding structure, domain architecture and amino acid sequence, nonetheless the mechanism appears to be fundamentally different in inflammatory immune responses.

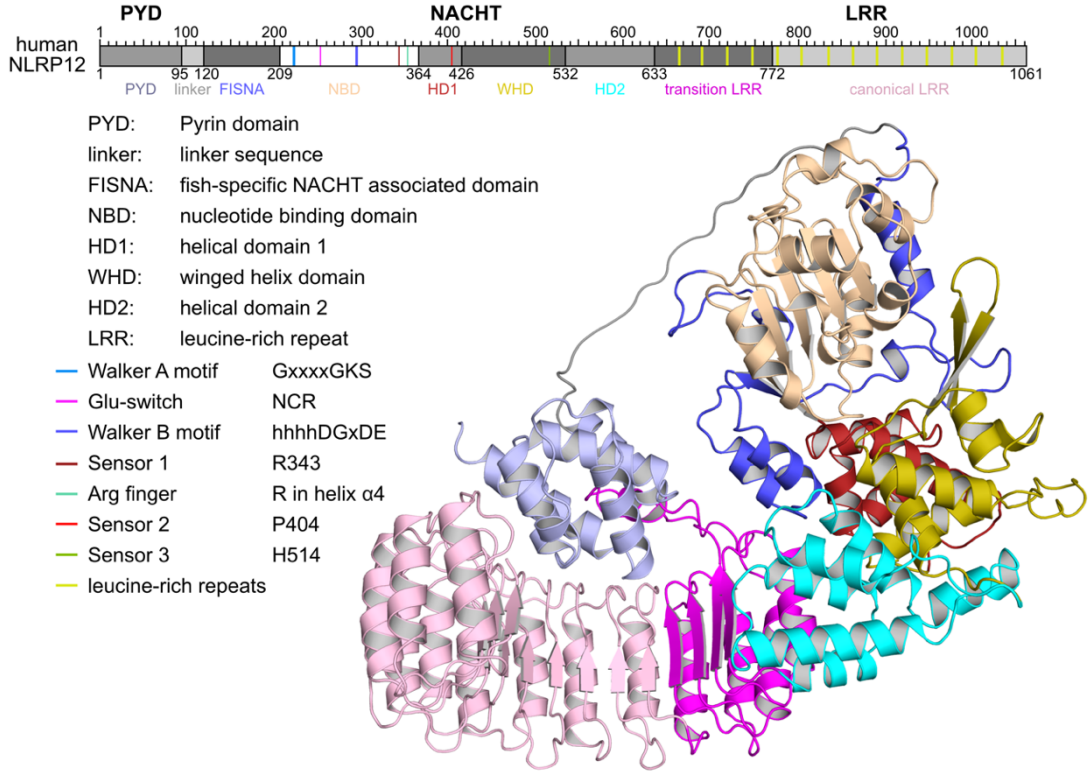

Figure 3-3: Domain architecture of human NLRP12.
Domain architecture and AlphaFold2 model of human NLRP12 with indicated domains (Jumper et al., 2021). The domain boundaries as well as different functional motifs are described.

3.3 Characterization of recombinantly expressed NLRP12

To investigate human NLRP12, it was recombinantly expressed in *Sf9* insect cells. Initial purifications of N-terminally MBP-tagged wild-type NLRP12 (1-1061, NLRP12^{wt}) by affinity chromatography and subsequent size-exclusion chromatography, revealed oligomerized and aggregated sample eluting in the void volume fraction (**Figure 3-4a**). Nevertheless, protein quality was tested by SDS-PAGE analysis (**Figure 3-4b**), which confirmed pure NLRP12^{wt} protein. For structure determination or further analytical experiments, a truncated construct of NLRP12 was designed. In protein crystallography, it is common practice to crystallize only functional domains because unstructured domains tend to aggregate rather than crystallize.

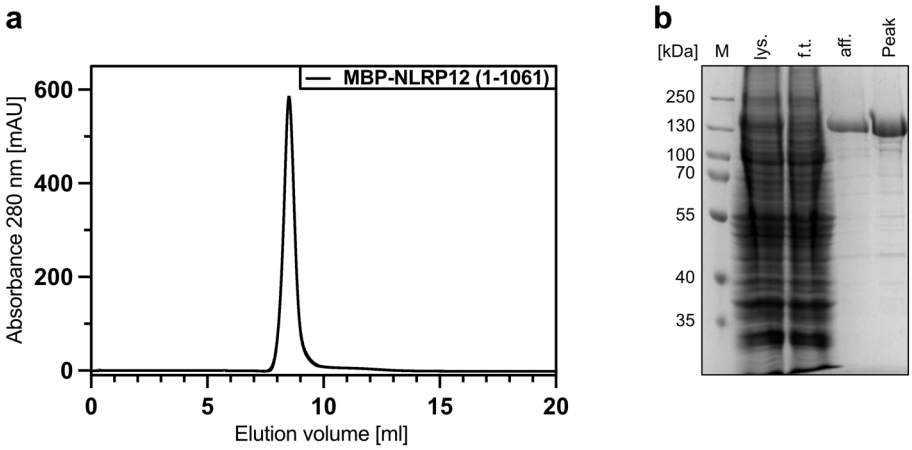

Figure 3-4: Purification of NLRP12wt.
*(**a**) Chromatogram of NLRP12^{wt} injected on a Superose 6 Increase 10/300 column after affinity purification. The peak shows the NLRP12 sample. The x-axis shows the retention volume in ml and the y-axis the UV absorption at 280 nm in mAU. (**b**) Coomassie-stained SDS-PAGE analysis with samples from (a), M: marker, lys.: lysate, f.t.: flow through, aff.: sample after affinity chromatography.*

Together with Dr. Michael Marleaux, we established a NACHT domain construct similar to NLRP3. The boundaries were designed based on secondary structure elements and the amino acid sequence. Two polar and basic residues (arginine) were selected to stabilize the ends. After optimizing the expression and purification conditions, NLRP12^{NACHT} (122-679) was used for further crystallization and small molecule inhibitor binding studies. The N-terminal MBP-tagged NLRP12^{NACHT} (122-679), including a TEV cleavage site between the tag and protein of interest, was purified by affinity chromatography. Overnight TEV cleavage (1/50 w/w) and subsequent size-exclusion chromatography revealed three different species (**Figure 3-5a**). SDS-PAGE analysis showed NLRP12 in the first and second peak, indicating different protein states. The third peak corresponded to cleaved MBP. The second peak corresponded to a molecular mass of around 65 kDa, which fits to that of the monomer of NLRP12^{NACHT} (122-679) (**Figure 3-5b**). This fraction was further analyzed by SEC-MALS to confirm the molecular mass (**Figure 3-5c**).

NLRP12^{NACHT} (122-679) protein could be concentrated up to 10-15 mg/ml and was used for crystallization experiments. Some examples for grown crystals are shown in **Figure 3-5d**. Unfortunately, the crystals showed no diffraction pattern during analysis at DESY Hamburg. Therefore, no further structure determination could be performed.

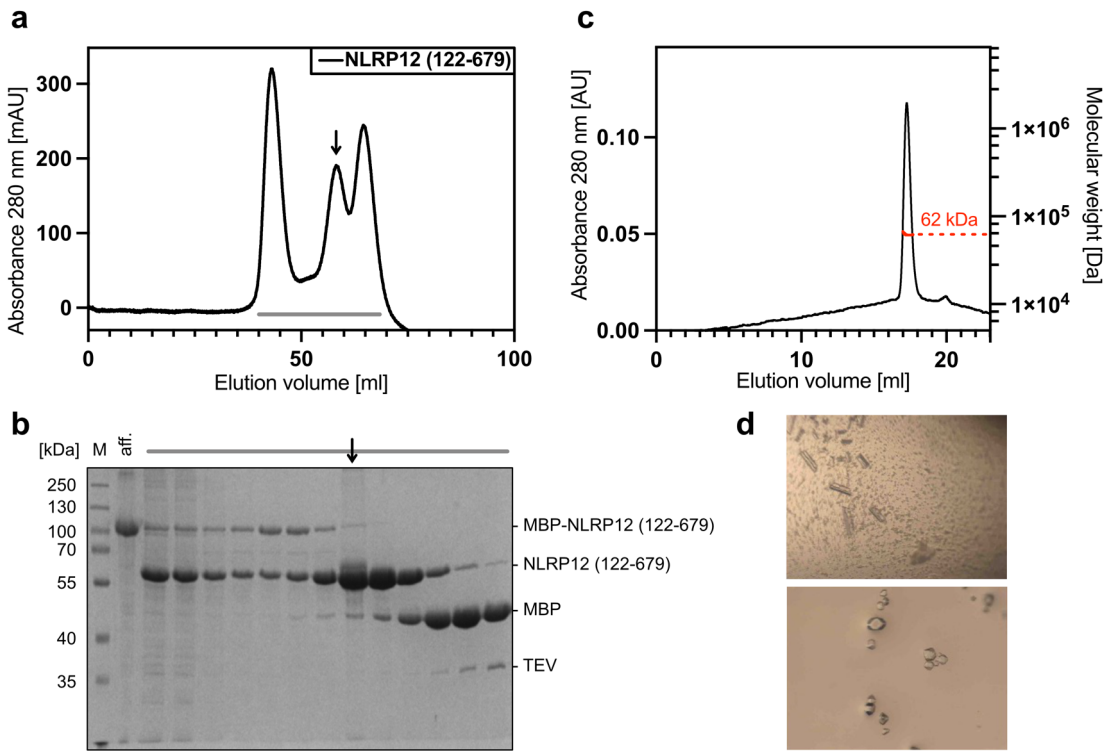

Figure 3-5: Purification and crystallization of NLRP12^{NACHT} (122-679).
*(**a**) Chromatogram of NLRP12^{NACHT} (122-679) injected on a HiLoad 16/600 Superdex 75 pg column after affinity purification and overnight TEV cleavage 1/50 w/w. Fractions for SDS-PAGE analysis are indicated with a grey bar. Monomer fraction is indicated by an arrow. The x-axis shows the retention volume in ml and the y-axis the UV absorption at 280 nm in mAU. (**b**) Coomassie-stained SDS-PAGE analysis with samples from (a), M: marker, aff.: sample after affinity chromatography. Four different proteins are detected. (**c**) MALS measurement of NLRP12^{NACHT} (122-679) (arrow marked) injected onto a Superose 6 Increase 10/300 column with a measured mass of 62 kDa. The theoretical mass is calculated to be 64.7 kDa. (**d**) Crystals of NLRP12^{NACHT} (122-679) grown in commercially available screens (examples grown with Ligand friendly screen).*

In a further attempt, three different constructs for the NLRP12^{NACHT} domain were designed, cloned and expressed in *Sf9* insect cells to test them for protein quality and crystallization ability. For this purpose, three amino acid residues at the C-terminus of the NLRP12^{NACHT} domain were selected to modify protein properties (**Figure 3-6**).

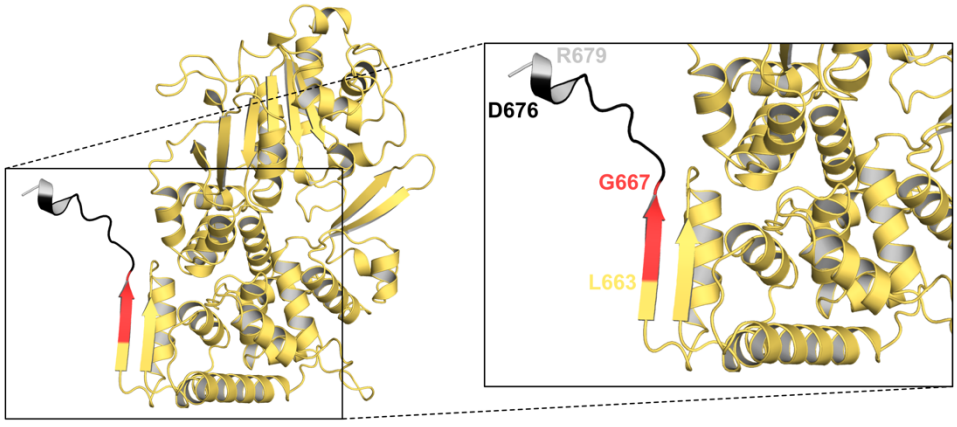

Figure 3-6: Different NLRP12^{NACHT} domain constructs.
NLRP12^{NACHT} domain with indicated amino acids. Grey: 122-679, black: 122-676, red 122-667, yellow: 122-663. Structure model of human NLRP12 modelled with AlphaFold2 (Jumper et al., 2021).

Leucin 663 was selected as a non-polar end, glycine 667 was selected due to its position at the tip of a β-sheet and aspartic acid 676 was selected as an acidic residue to border the construct.

All three constructs were expressed in *Sf9* insect cells as N-terminal MBP tagged fusion proteins and subsequently purified by affinity chromatography, TEV cleavage and size exclusion chromatography. The respective chromatograms are shown in **Figure 3-7a**. Comparable yield of protein was observed for constructs 122-667 and 122-676, whereas 122-663 exhibited low expression yields. All constructs showed pure protein samples in SDS-PAGE analysis and correspond to the expected protein size (**Figure 3-7b**). Protein stability measurements using nanoDSF resulted in a decrease of 5 °C in thermal stability for the construct 122-663, reflecting the low yield of the protein purification of this construct. The other two constructs (122-676, 122-667) showed similar stability to the initial NLRP12^{NACHT} (122-679) construct (**Figure 3-7c,d**). Based on these results, no relevant change in protein behavior for further experiments was expected. Nevertheless, NLRP12^{NACHT} (122-676) was later used for NLRP12 nanobody generation.

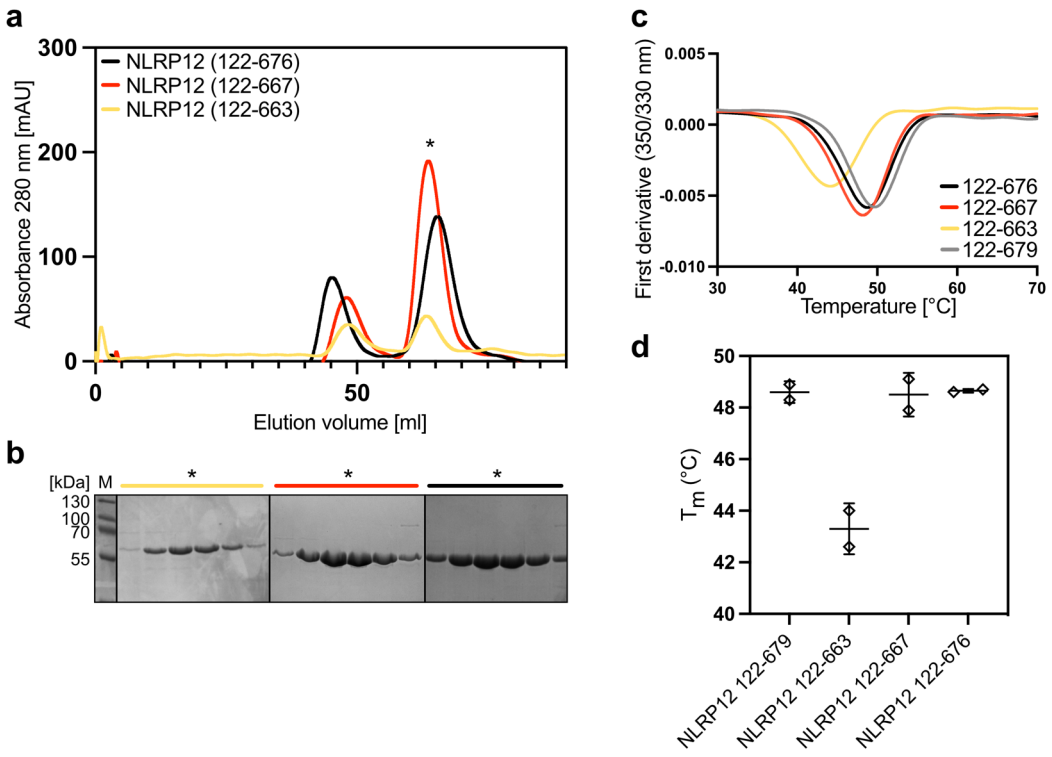

Figure 3-7: Purification and thermal stability measurements of different NLRP12^{NACHT} domain constructs.
*(**a**) Chromatograms of NLRP12^{NACHT} (122-676, 122-667, 122-663) injected on a HiLoad 16/600 Superdex 75 pg column after affinity purification and overnight TEV cleavage 1/50 w/w. Fractions for SDS-PAGE analysis are indicated with an asterisk. The x-axis shows the retention volume in ml and the y-axis the UV absorption at 280 nm in mAU. (**b**) Coomassie-stained SDS-PAGE analysis with samples from (a), M: marker. (**c**) NanoDSF measurements of NLRP12^{NACHT} constructs showing the first derivative of respective melting curves. The x-axis shows the temperature in °C and the y-axis the first derivative of 350/330 nm wavelenghth absorption. (**d**) Summary of nanoDSF measurements showing duplicates for all measurements.*

3.4 Human NLRP12 targeting Nanobodies

Nanobodies have been described to be a helpful tool in the mechanistical and structural investigation of proteins (Manglik et al., 2016; Peter et al., 2022). This approach was used to generate human NLRP12 specific nanobodies to improve the crystallization process and to gain more information about the protein structure. The immunization campaign was done with NLRP12^{NACHT} (122-676) sample (section 3.3). The generation, panning and hit identification process was provided by the Core Facility Nanobodies (University of Bonn) in the group of Dr. Stephan Menzel. A general overview about the nanobody generation process is shown in **Figure 3-8**. This section will not cover these processes and begins with the nanobody characterization.

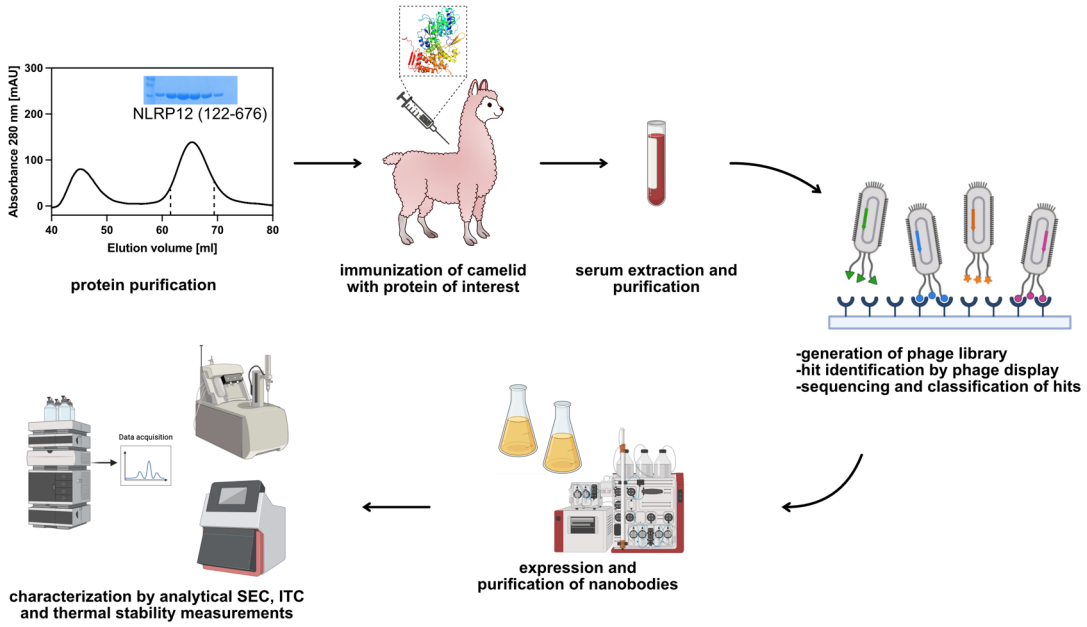

Figure 3-8: Overview on Nanobody generation.
Protein purification was done for camelid immunization. The camelid was immunized with the purified protein and after 12 weeks the blood serum was harvested. After serum extraction and purification, a phage library was generated and potential hits identified by phage display. The resulting hits were sequenced, expressed and further characterized by analytical methods.

The phage display only resulted in one potential NLRP12^{NACHT} Nanobody (NbN12) identified by ELISA. The corresponding nucleotide sequence was cloned into an *E. coli* expression vector, carrying a 6xHis tag and expressed in terrific broth (TB) media. The N-terminal 6xHis tagged fusion protein was purified by Ni^{2+}-NTA affinity chromatography and subsequent SEC. The chromatogram showed a high monomer peak at 70 – 85 ml (blue) (**Figure 3-9a**) with a high purity confirmed by Coomassie-stained SDS-PAGE analyses (**Figure 3-9b**). Interaction studies were performed to investigate binding of NbN12 to NLRP12. All measurements included 30 min incubation time. There was no shift in the melting temperature of protein in the thermal shift assay, suggesting neither stabilization, nor destabilization effect of NbN12 on NLRP12 (**Figure 3-9c**). Analytical SEC revealed single signals for NLRP12 (122-676) and NbN12 eluting in distinct peaks. In case of complex formation, a shift in the elution time should occur, but upon incubation of NLRP12 with the nanobody, no difference was observed (**Figure 3-9d**). Lastly, direct binding was tested in ITC measurements, but no changes in the temperature, and thus enthalpy were detected (**Figure 3-9e**). Taken together, NbN12 did not bind to NLRP12 and was most likely a false positive hit during identification.

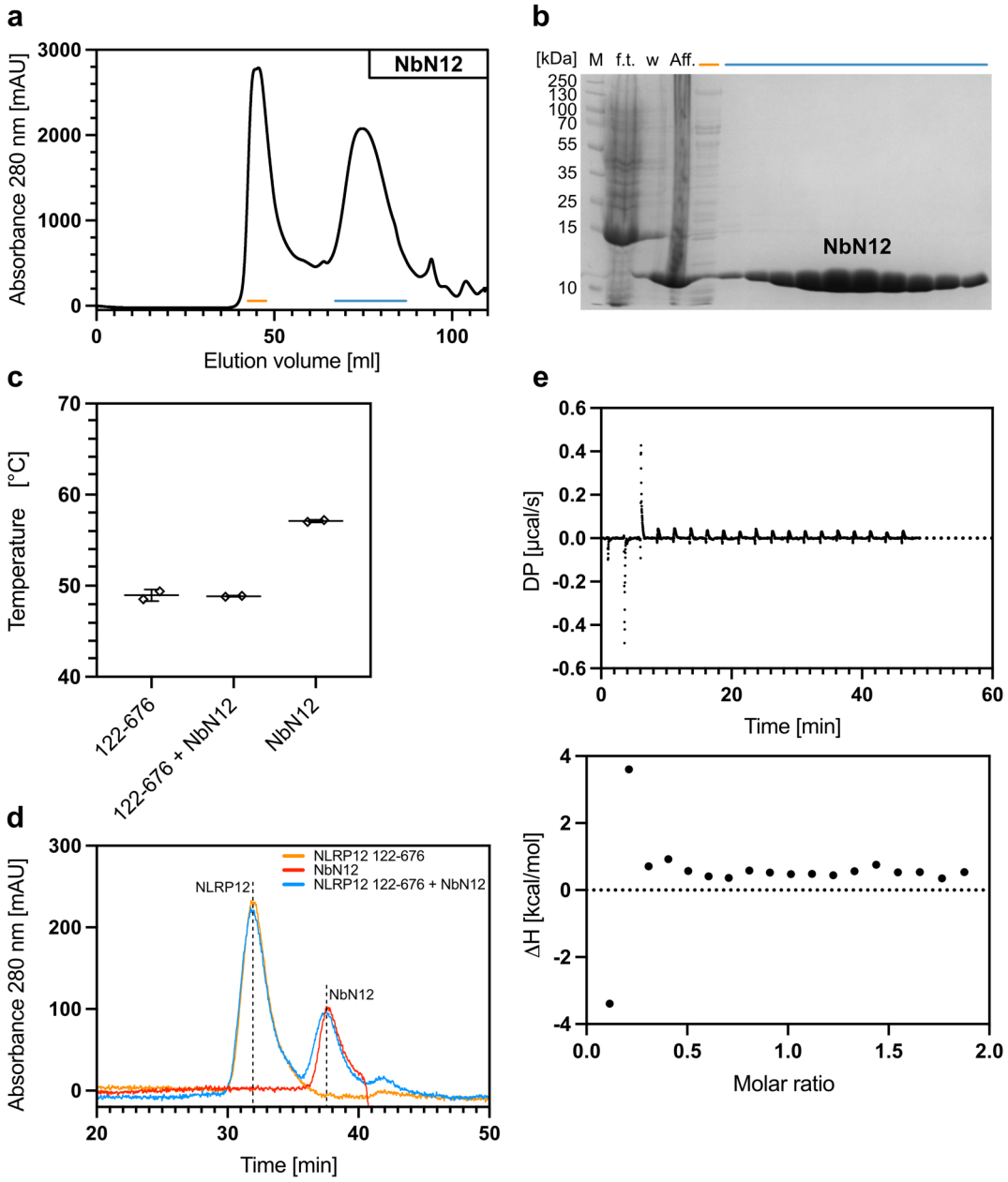

Figure 3-9: Characterization of an NLRP12 specific Nanobody.
*(**a**) Chromatogram of NbN12 injected on a HiLoad 16/600 Superdex 75 pg column after affinity purification with Ni^{2+}- affinity chromatography. Fractions for SDS-PAGE analysis are indicated with colored bars. The x-axis shows the retention volume in ml and the y-axis the UV absorption at 280 nm in mAU. (**b**) Coomassie-stained SDS-PAGE analysis with samples from (a), M: marker, f.t.: flow through, w: wash, Aff.: affinity sample. (**c**) Thermal stability measurements: 30 µM of $NLRP12^{NACHT}$ (122-676) was measured with 30 µM NbN12. Duplicates are shown. (**d**) Analytical SEC using a HPLC system with a Superdex increase 200 3.2/300. NLRP12 (122-676) (yellow), NbN12 (red), and a 1:1 mixture (blue) were injected with 50 µl. (**e**) ITC measurements of NLRP12 (122-676) with NbN12 showed no apparent interaction.*

3.5 Small molecule inhibitor binding studies

Since MCC950 (CRID3) was identified as a potent inhibitor of NLRP3 (Coll et al., 2015), NLRP12 was also tested for its MCC950 binding ability. Thus, recombinantly expressed NACHT domains of both proteins were used in thermal stability measurements to investigate the stabilizing or destabilizing effect upon compound binding. At a concentration of 3 µM, NLRP3 showed a stabilization of 13 °C induced by 30 µM MCC950 binding compared to the control measurement. For NLRP12 this effect was much smaller at similar concentrations, but still showing 2-3 °C stabilization (**Figure 3-10a**). Following these observations, SPR measurements were performed to determine binding affinities of MCC950 to NLRP3/12. Protein samples were recombinantly expressed and biotinylated in *Sf9* insect cells and subsequently purified by affinity chromatography. Biotinylated samples were coupled via biotin-streptavidin coupling to SA sensor chips. Different concentrations of MCC950 were used to determine dissociation constants. With a dilution series starting from 600 nM, a dissociation constant for MCC950 to NLRP3^{NACHT} (131-694) of 27 nM was measured, whereas for NLRP12^{NACHT} (122-679) no dissociation constant could be determined (**Figure 3-10b**).

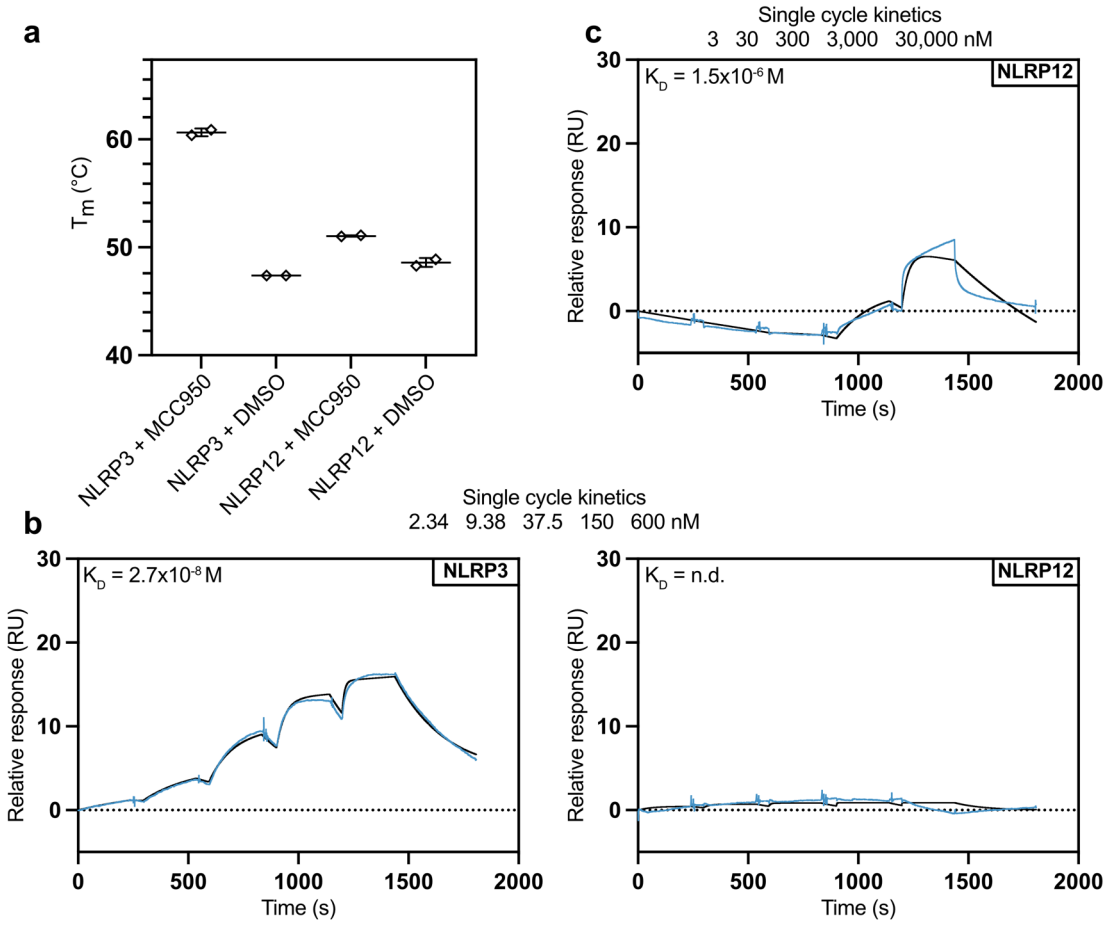

Figure 3-10: MCC950 binding experiments with NLRP3 and NLRP12.
(a) *Thermal stability measurements: 3 µM of NLRP3^{NACHT} (131-694) was measured with 30 µM MCC950 and with 2 % DMSO as control. The same measurement was performed with 3 µM of NLRP12^{NACHT} (122-679). Duplicates are shown.* ***(b)*** *SPR single cycle kinetics sensorgrams of NLRP3^{NACHT} (131-694) and NLRP12^{NACHT} (122-679) with indicated injections of MCC950. The calculated equilibrium dissociation constant K_D was determined using a 1:1 binding model. (c) SPR single cycle kinetics sensorgram of NLRP12^{NACHT} (122-679) with higher concentrations of MCC950. The SPR measurements were performed together with Dr. Michael Marleaux.*

Another dilution series was performed on NLRP12^{NACHT} (122-679) to test for weaker binding affinities. A peak concentration of 30 µM MCC950 was used and each step was diluted 1/10. A dissociation constant of 1.5 µM was calculated, indicating a significantly lower binding affinity compared to NLRP3 (**Figure 3-10c**). Based on these results, NLRP12 mutation studies were designed and performed to potentially increase the binding affinity to MCC950 derivatives.

3.5.1 NLRP12^{NACHT} mutation studies

To gain further mechanistic insight into the binding of MCC950 to NLRP12^{NACHT}, several mutations were introduced into the expected binding interface based on NLRP3 analysis. The MCC950 binding pocket in NLRP3 is formed by five subdomains (NBD, HD1, WHD, HD2, trLRR). The hexahydro-*s*-indacene moiety is surrounded by several hydrophobic residues (Met408, Phe410, Ile411, Leu413, Thr439, Tyr443, Thr525, Phe575, Tyr632 and Met661). The sulfonylurea group is located between Ala228 (Walker A), Arg351 and Arg578 binding via hydrogen bond interactions. Also, Gln624 and Glu629 contribute to the binding by stabilizing a water molecule interacting with the tertiary hydroxy group in MCC950. The characterization of the MCC950 binding pocket in NLRP3 was done by Dr. Michael Marleaux in his dissertation.

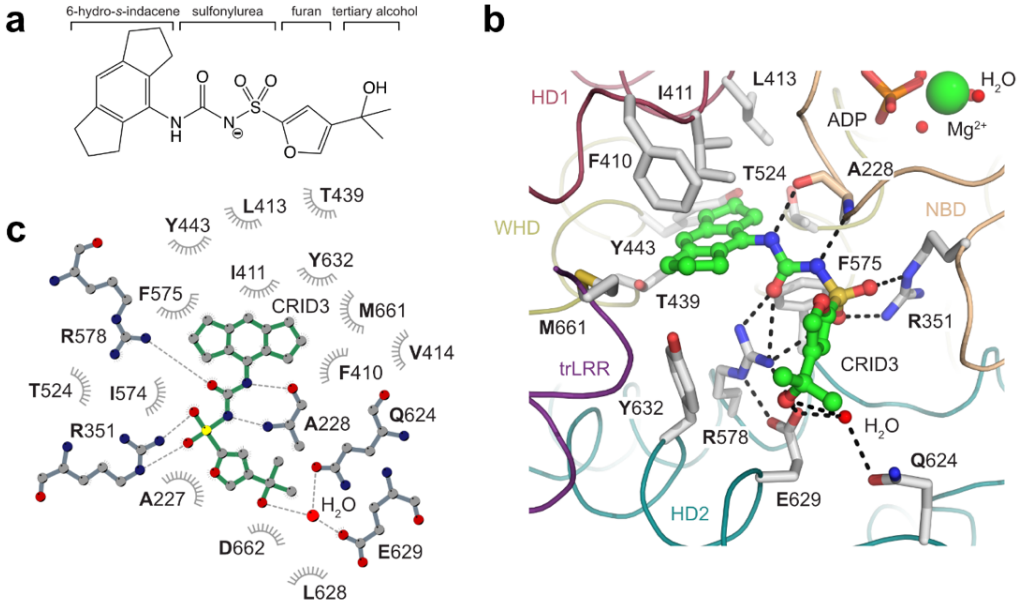

Figure 3-11: MCC950 binding site in NLRP3.
*(**a**) Structural formula of MCC950 with deprotonated nitrogen and depiction of the different moieties. (**b**) Detailed view on important molecular interactions of NLRP3 with MCC950. Important main chains and sidechains are shown as sticks. MCC950 is shown in stick-and-balls representation and with carbons colored green. The magnesium ion is shown as a green sphere. Water molecules are shown as red spheres. Hydrogen bond interactions are shown as dashed black lines. (**c**) Simplified view on the molecular interactions of NLRP3 with MCC950 generated with LigPlot+ (Laskowski & Swindells, 2011). Figure from the dissertation of Dr. Michael Marleaux, 2022 (Biochemical and structural studies of NOD-like receptors and their inhibition by small molecule inhibitors).*

Due to the close relationship between NLRP12 and NLRP3, most of the interacting residues are present in NLRP12 as well. Nevertheless, the binding affinity is significantly weaker. Thus, a detailed analysis of the potential binding pocket was performed based on a sequence alignment (**Figure 3-2**). Therefore, eight residues in NLRP12^{NACHT} were identified and selected to mutate (Val403 in the HD1, Ser516 in the WHD, Ala557 and Leu558 in the HD2, Gly609 and Ser615 in the HD2, Ala642 and Glu646 in the trLRR).

3.5.1.1 NLRP12 MCC950 gain of binding mutants

The previously mentioned eight amino acid residues were mutated in NLRP12^{NACHT} (122-679) to the respective residues in NLRP3 (**Table 3-1**).

Table 3-1: Selected amino acid residues for mutational studies of NLRP12.

Residue NLRP12	Residue NLRP3	Residue NLRP12	Residue NLRP3
Val403	Ile411	Gly609	Ser626
Ser516	Thr525	Ser615	Tyr632
Ala557	Ile574	Ala642	Ser658
Leu558	Phe575	Glu646	Asp662

NLRP12^{NACHT} (122-679) 8xmutant was expressed in *Sf9* insect cells as N-terminal MBP tagged fusion protein and subsequently purified by affinity chromatography, TEV cleavage, and size exclusion chromatography. The majority of eluted protein was observed in the void volume at 45 ml elution volume, followed by a small shoulder and a second peak at 65 ml elution volume (**Figure 3-12a**). NLRP12^{NACHT} (122-679) 8xmutant eluted in the void peak, as well as in the shoulder and MBP in the second peak. The yield was lower compared to wild-type NLRP12^{NACHT} (122-679) and no distinct monomeric fraction was observed (**Figure 3-12b**), indicating an unstable and non-functional protein construct.

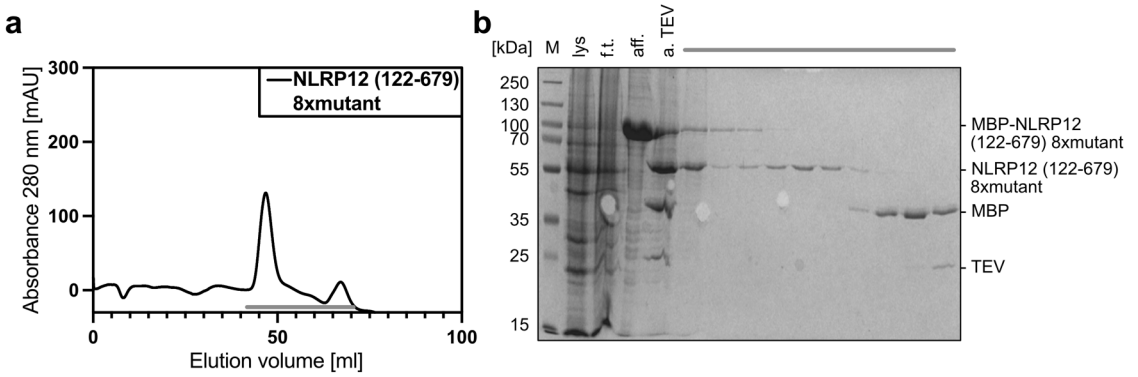

Figure 3-12: Purification of NLRP12^{NACHT} (122-679) 8xmutant.
*(**a**) Chromatogram of NLRP12^{NACHT} (122-679) 8xmutant injected on a HiLoad 16/600 Superdex 75 pg column after affinity purification and overnight TEV cleavage 1/50. Fractions for SDS-PAGE analysis are indicated by a grey bar. The x-axis shows the retention volume in ml and the y-axis the UV absorption at 280 nm in mAU. (**b**) Coomassie-stained SDS-PAGE analysis with samples from (a), M: marker, lys.: lysate, f.t.: flow through, aff.: sample after affinity chromatography, a.TEV: sample after TEV digest.*

3.5.1.2 Identify protein stability to amino acid mutations

To determine whether one or more amino acid mutations were responsible for the non-functional NLRP12^{NACHT} (122-679) 8xmutant construct compared to the wild-type variant, the mutations were analyzed separately. Due to their location in the sequence, either single or double mutations were introduced by several PCR reactions, resulting in five different mutants (V403I, S516T, A557I/L558F, G609S/S615Y, A642S/E646D). All of these were expressed in *Sf9* insect cells as N-terminal MBP tagged fusion proteins and subsequently purified by affinity chromatography, TEV cleavage and size exclusion chromatography. All chromatograms and SDS-PAGE gels are shown in **Figure 3-13**.

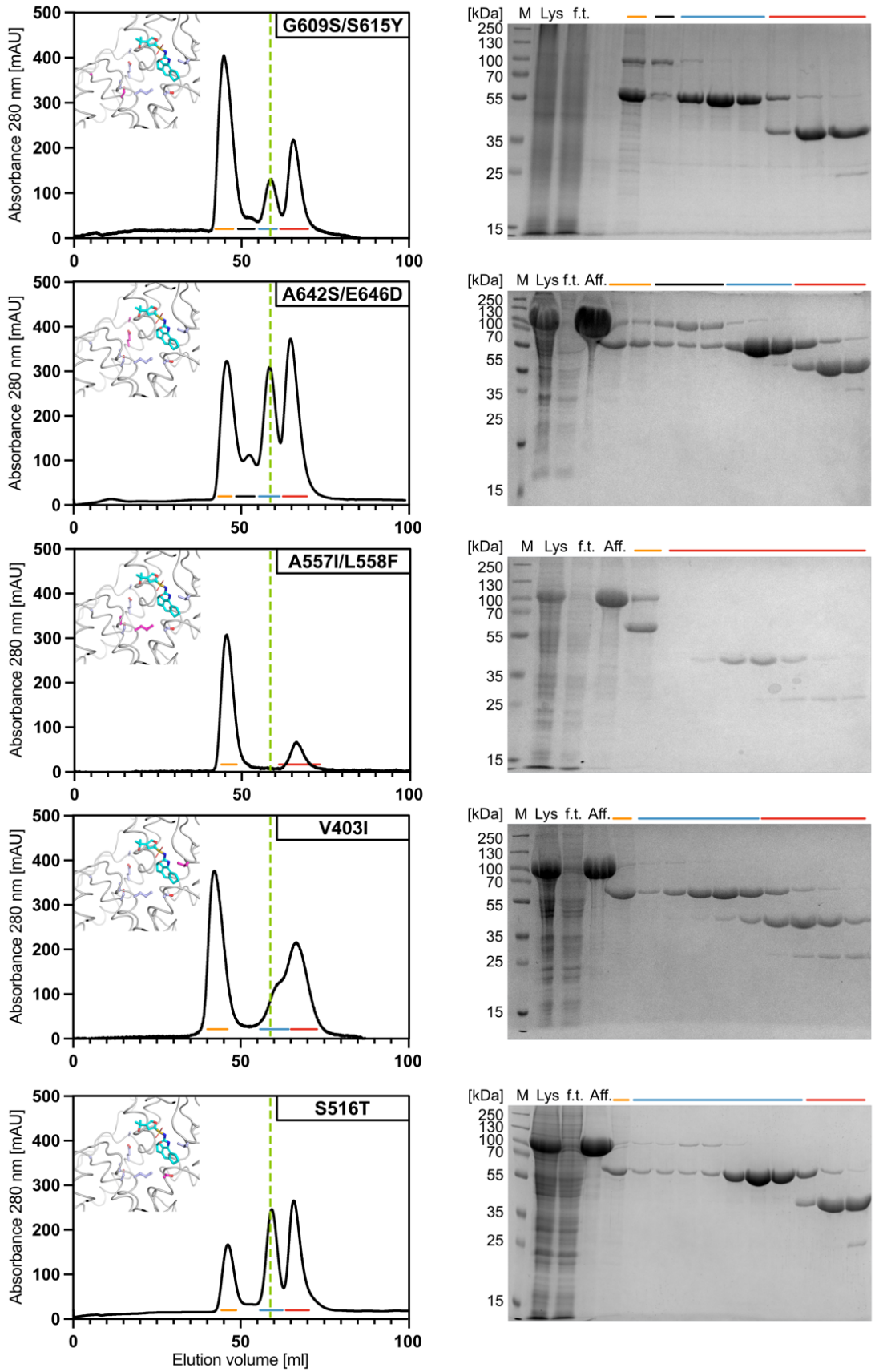

Figure 3-13: Purifications of NLRP12 gain of function mutants for MCC950 binding.
Chromatograms of NLRP12^{NACHT} (122-679) mutants injected on a HiLoad 16/600 Superdex 75 pg column after affinity purification and overnight TEV cleavage 1/50 w/w. Fractions for SDS-PAGE analysis are indicated with clored bars. The x-axis shows the retention volume in ml and the y-axis the UV absorption at 280 nm in mAU. Coomassie-stained SDS-PAGE analysis with indicated samples M: marker, lys.: lysate, f.t.: flow through, aff.: sample after affinity chromatography. Green dashed line indicates monomer fractions. Corresponding mutations are shown in light blue and highlighted in magenta. MCC950 is shown in cyan. NLRP12 AlphaFold2 model based on NLRP3.

A defined monomer peak was observed for the S516T, G609S/S615Y and A642S/E646D mutants. For the V403I mutant, the peak was not as well defined, but monomeric species were still present. The A557I/L558F double mutant showed no monomeric fractions, indicating that at least one of these mutations is responsible for a non-functional protein.

Now that it was clear which of these residues were important for protein integrity, a new mutant was cloned. A detailed analysis of the steric arrangement of the A557I and L558F mutants led to the decision to remove the A557I mutation, as the steric hindrance was expected to cause an incorrect fold based on the AlphaFold2 model (Jumper et al., 2021) of NLRP12. NLRP12^{NACHT} (122-679) 7xmutant was expressed in *Sf9* insect cells as N-terminal MBP tagged fusion protein and subsequently purified by affinity chromatography, TEV cleavage and size exclusion chromatography. A well-defined monomer peak was observed (**Figure 3-14a**) and verified via SDS-PAGE analysis (**Figure 3-14b**).

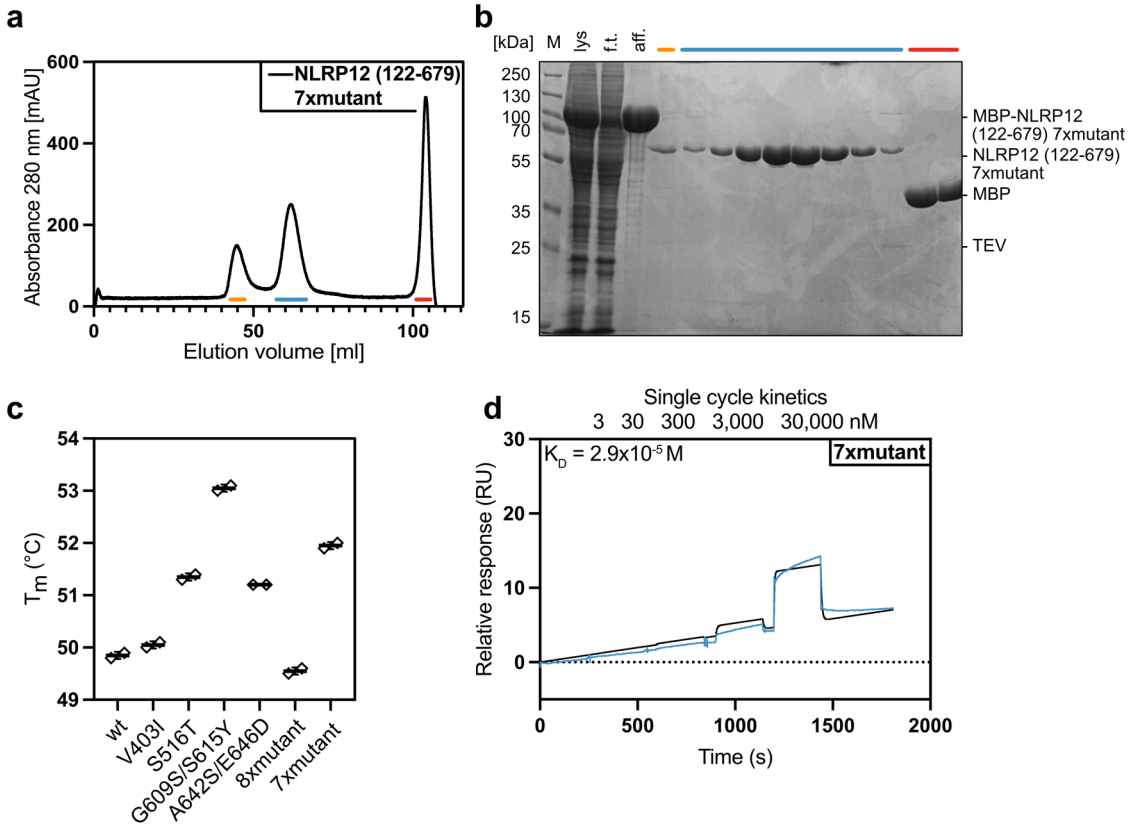

Figure 3-14: Purification and analysis of NLRP12^{NACHT} (122-679) 7xmutant.
*(**a**) Chromatogram of NLRP12^{NACHT} (122-679) 7xmutant injected on a HiLoad 16/600 Superdex 75 pg column with tandem MBPTrap after affinity purification and overnight TEV cleavage 1/50. Fractions for SDS-PAGE analysis are indicated by colored bars. The x-axis shows the retention volume in ml and the y-axis the UV absorption at 280 nm in mAU. (**b**) Coomassie-stained SDS-PAGE analysis with samples from (a), M: marker, lys.: lysate, f.t.: flow through, aff.: sample after affinity chromatography. According fractions are marked with colored bars. (**c**) Thermal stability measurements: 3 µM of NLRP12^{NACHT} mutants were measured with 10 µM MCC950 in all purification buffers. Duplicates are shown. (**d**) SPR single cycle kinetics sensorgram of NLRP12^{NACHT} (122-679) 7xmutant with indicated concentrations of MCC950. SPR measurement was performed together with Dr. Michael Marleaux.*

Thermal stability measurements revealed a destabilization of the 8xmutant as expected from previous experiments. The V403I mutant showed no change to wild-type, whereas all other mutants showed a higher thermal stability in a purification supplemented with 10 µM MCC950 (**Figure 3-14c**). A single cycle kinetics measurement with biotinylated

NLRP12^{NACHT} (122-679) 7xmutant and peak concentration of 30 µM MCC950 resulted in a dissociation constant of 290 µM. The binding to MCC950 is thus still approximately 1,000x weaker than for NLRP3^{NACHT} (**Figure 3-14d**).

Since the NLRP12^{NACHT} mutants did not improve the MCC950 binding, other small molecules based on MCC950 were selected and tested in biomolecular measurements.

3.5.2 MCC950-based compounds studies

Based on the MCC950 studies by (Keuler et al., 2022), we designed and tested new related compounds that were modified in several parts compared to MCC950. The central sulfonylurea moiety was retained and either the 6-hydro-*s*-indacene moiety or the furan moiety was replaced with various groups. The compounds were a kind gift from Dr. Tim Keuler. All compounds were tested in thermal stability measurements (**Figure 3-15**). As shown previously, MCC950 lead to a stabilization of 2.5 °C. Gue-compounds **3624**, **3625**, **3626**, **3627**, **3630** and **4040** showed no stabilizing effect. All of these are lacking the 6-hydro-*s*-indacene moiety, indicating that this part is involved in the interaction with NLRP12. In Gue-compound **3752** the 6-hydro-*s*-indacene moiety is replaced with an octa-hydroanthracene moiety, resulting in a stabilization below 1 °C. Thus, the binding pocket is likely too small for the larger structure. Gue-compound **3649** is lacking the furan group, which is replaced by an iso-propyl group, resulting in a slightly smaller

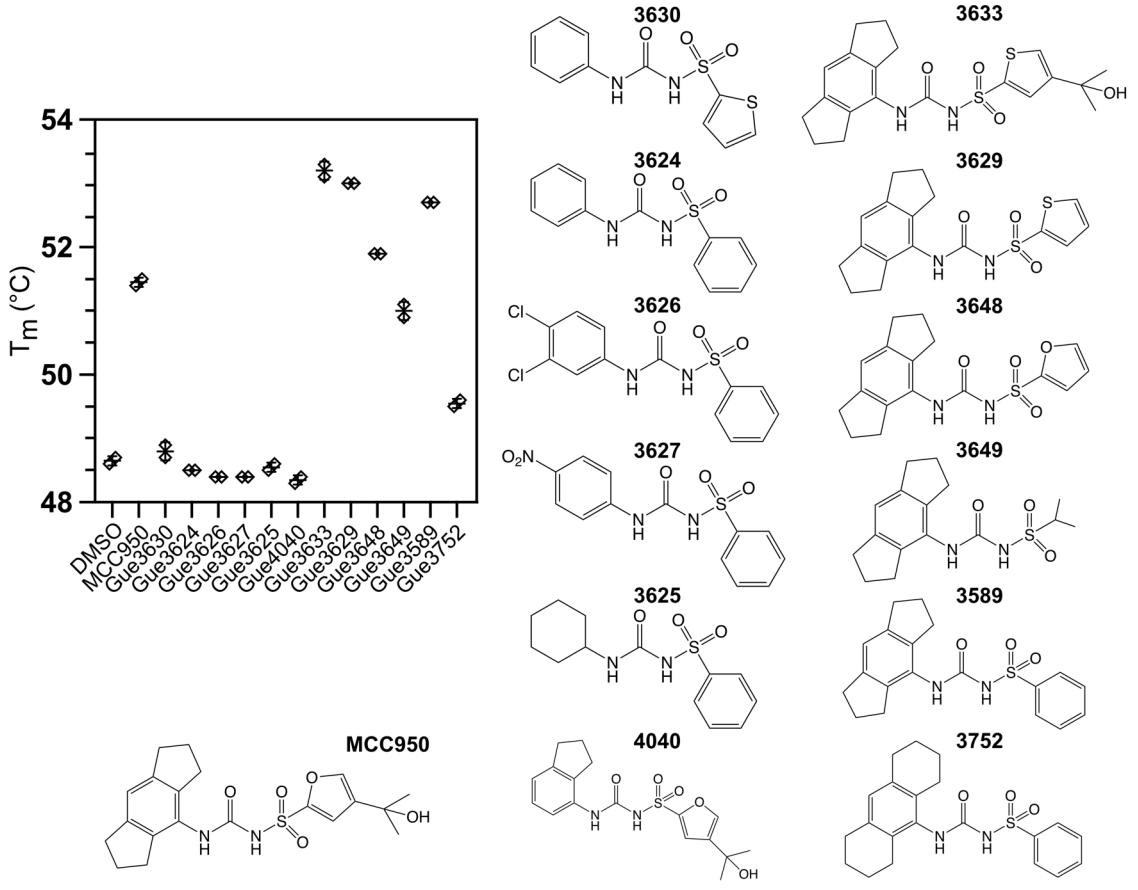

Figure 3-15: MCC950 based compounds tested with NLRP12.
Thermal stability measurements of 3 µM NLRP12^{NACHT} (122-679), measured with 30 µM of the respective small molecules. Duplicates are shown. All Guetschow (Gue) compounds are shown with their number and chemical structure (Keuler et al., 2022). Additionally, MCC950 is shown as a reference.

stabilization of 2 °C compared to MCC950. Gue-compound **3629** and **3648** containing either a furan or thiophene moiety and showed a stabilization of 3.5 °C, indicating the importance of this moiety in the binding. The thiophene analog to MCC950 (Gue **3633**) showed the highest stabilizing effect with 3.5 °C.

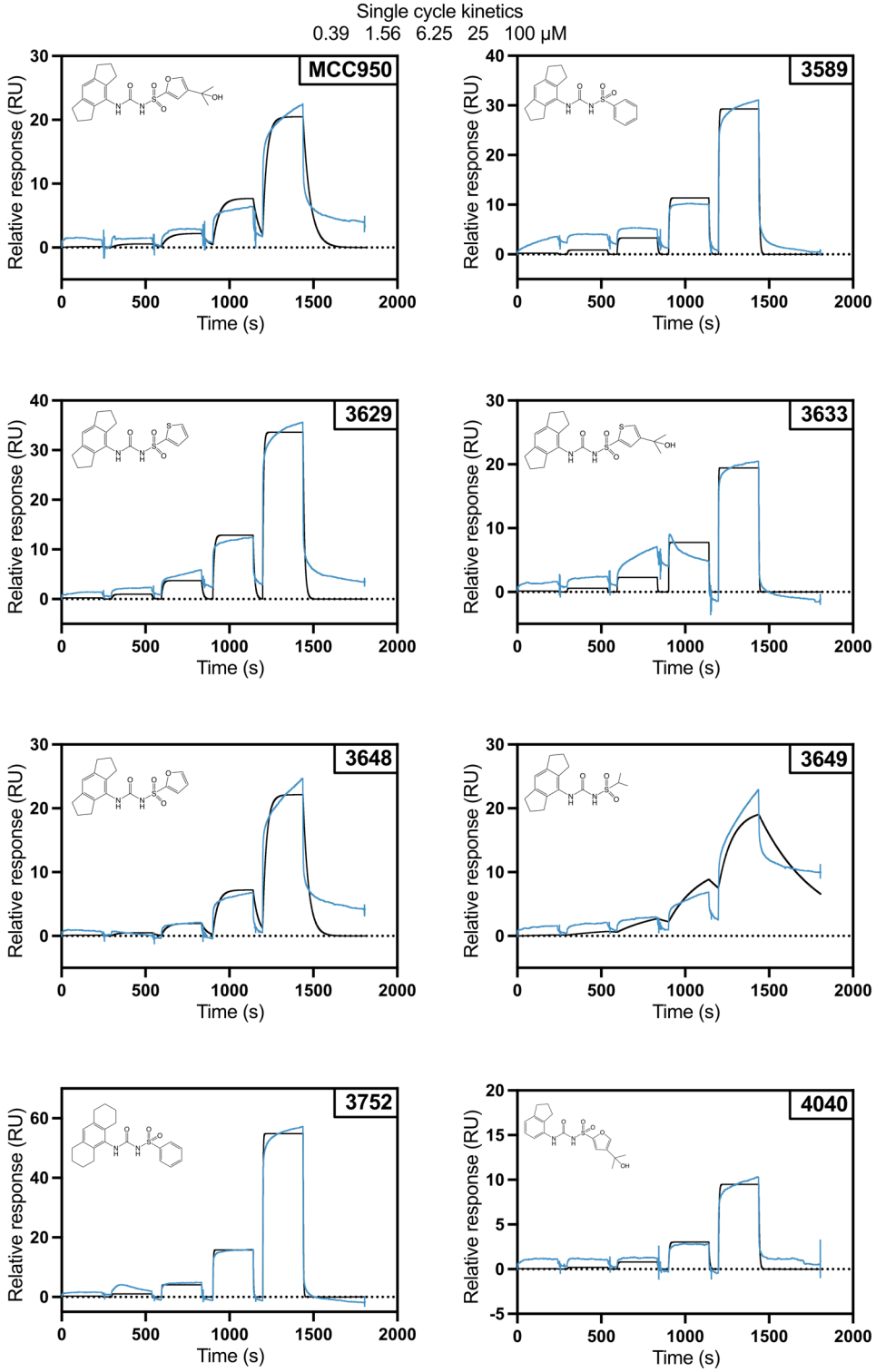

Figure 3-16: SPR measurements of MCC950-based small molecule inhibitors.
SPR single cycle kinetics sensorgrams of NLRP12^{NACHT} (122-679) wt with different small molecule inhibitors. Used concentrations are indicated at the top. Chemical structures are given for each measurement. All compounds were gifted by Dr. Tim Keuler and Prof. Michael Gütschow. SPR measurements were performed together with Dr. Michael Marleaux.

Compounds that showed a stabilizing effect on NLRP12 in thermal shift assays (**Figure 3-15**) were selected to be tested in SPR measurements (**Figure 3-16**). A peak concentration of 100 µM was used for all compounds resulting in dissociation constants in the micro- or millimolar range. Thus, the binding is weak and not sufficient for further experiments.

Ultimately, all of these measurements demonstrate an interaction between MCC950-based small molecule inhibitors and NLRP12, but the effect is significantly smaller than that shown for NLRP3. Therefore, further compound optimization is needed to improve binding affinities and inhibitory effects.

3.6 Discussion and conclusion

Until today NLRP12 is a poorly characterized pattern recognition receptor within the NLR protein family. Since its first description in 2002, the role of NLRP12 in the human immune response is still not well understood (L. Wang et al., 2002). Studies have shown NLRP12 as a suppressor in TLR signaling, but at the same time as an activator for inflammasome signaling upon infections (Coombs et al., 2024; Tuladhar & Kanneganti, 2020; Vladimer et al., 2012).

Because NLRP12 is involved in various inflammatory diseases, such as SAID, FCAS2, and multiple sclerosis, understanding more about its structure and function is of great interest.

The close relationship between NLRP12 and NLRP3 provides a good foundation for further research on NLRP12. Especially in the NACHT domain both amino acid sequences show an identity of 55 %, indicating a high probability for similar functions and structural elements (**Figure 3-2**). NLRP3 was shown to form a decameric assembly in the purification process (Hochheiser, Pilsl, et al., 2022), whereas NLRP12 was found in the void volume as an oligomerized and probably unstructured species (**Figure 3-4**). This sample quality was insufficient for further structure determination. A frequently chosen method for structure determination is to divide the target protein into smaller fragments to improve protein handling. Here, NLRP12 was truncated to its central NACHT domain to reduce the degree of freedom in the protein structure. It was possible to purify $NLRP12^{NACHT}$ as a monomer with high purity and concentration. Unfortunately, crystallization screening did not lead to suitable crystal formation (**Figure 3-5**). All grown and analyzed crystals showed no diffraction pattern during measurement at DESY Hamburg and would need further optimization.

A widely used method to improve crystallization processes is the use of nanobodies, as crystallization chaperones, derived from camelids (Duhoo et al., 2017). An immunization campaign was done for $NLRP12^{NACHT}$ to generate specific nanobodies. The panning process resulted in only one potential binder, that turned out to be a false positive hit during further characterization (**Figure 3-9**). Following this observation, a detailed analysis of the amino acid sequence of *human* NLRP12 and *alpaca* NLRP12 was performed, offering a high conservation between these species (**Figure 7-2**). The predicted structures were also strikingly similar (**Figure 7-3**) (Abramson et al., 2024). In summary, the close relationship between these species suggests that camelids do not respond to *human* NLRP12 treatment due to the presence of endogenous NLRP12, which is a well-known amino acid pattern.

Another frequently used approach is the use of small molecules as interaction partners to enhance protein stability and reduce flexibility. Dr. Michael Marleaux was able to show

in his doctoral thesis (Biochemical and structural studies of NOD-like receptors and their inhibition by small molecule inhibitors, 2022) that binding of MCC950 to NLRP3^{NACHT} is crucial for structure determination by X-ray crystallography. The small molecule inhibitor connects all subdomains of the NACHT domain and thereby rigidifies the entire structure. It was shown that this interaction inhibits NLRP3 activation and blocks conformational changes essential for inflammasome formation (Hochheiser, Pilsl, et al., 2022).

Based on these results for NLRP3, it is likely that NLRP12 also has the ability to adapt different conformations. Since no small molecule inhibitors are known today, an apo crystal structure was attempted. However, the results obtained during crystallization trials indicated that NLRP12^{NACHT} offers high flexibility, so specific interaction partners are needed to improve protein stability for structure determination.

To test whether MCC950 is an off-target binder to NLRP12, it was tested in thermal stability measurements and showed indeed small stabilizing effects (**Figure 3-10**). Compared to NLRP3, however, this effect was rather small. Also, the measured dissociation constant for MCC950 binding to NLRP12 was weaker by a factor of ~50. These experiments suggested that the binding pocket offers crucial differences in single amino acids. A detailed analysis of the MCC950 binding site in NLRP3 revealed eight specific residues that differ compared to NLRP12. After mutation of these residues, the resulting protein was unstable and thus not possible to purify (**Figure 3-12**). Single-mutation analysis revealed that the loss of protein integrity was caused by either the A557I or L558F mutation (**Figure 3-13**). The significant steric modification from alanine to isoleucine was believed to result in the loss of stable monomeric species, so it was removed. Ultimately, this resulted in seven mutations in the NACHT domain of NLRP12, suitable for further characterization. The NLRP12^{NACHT} 7xmutant revealed high protein yield and a slightly higher melting temperature of 2-3 °C upon treatment with 10 µM MCC950 compared to wild-type. However, SPR measurement did not show a reasonable binding affinity leading to the result that the respective residues are not solely responsible for MCC950 binding (**Figure 3-14**).

In the group of Prof. Gütschow (University of Bonn) a series of MCC950 related compounds was synthesized, to investigate their binding ability to NLRP3. It was published that these compounds indeed bound to NLRP3 with a similar binding affinity (Keuler et al., 2022). A selection of twelve MCC950 based compounds was also tested for NLRP12 binding (**Figure 3-15**). Thermal shift assays revealed stabilizing effects of ~3 °C for six out of twelve compounds. Thus, the 6-hydro-*s*-indacene moiety was found to be responsible for the increased melting temperature, indicating the importance of the hydrophobic pocket in the binding site. The stabilization is decreased or lost once this moiety is modified or missing. However, the effect is similar to MCC950 and SPR measurements showed binding affinities in the micro- or millimolar range (**Figure 3-16**).

Taken together, these results showed that NLRP12 provides a compound-binding pocket in the NACHT domain. However, the synthesized molecules tested, which were designed for NLRP3, showed weak affinities to NLRP12. Therefore, NLRP12 is not an off-target receptor for this class of compounds, which proves its specificity for NLRP3. A designated compound screening and design approach must be conducted to create specific small molecule inhibitors for NLRP12.

4. NLRP10 as a unique inflammasome sensor

Parts of the here presented work were carried out in cooperation with Dr. Dennis de Graaf at the Institute of Innate Immunity (University of Bonn). Together with the working group of Prof. Dr. Thomas Kufer (University of Hohenheim) we investigated new NLRP10 interaction partners. Selina Enayat performed several NLRP10 purifications as well as further analytical experiments during her internship and master thesis. Negative stain electron microscopy sample preparation, grid preparation and imaging were done at the facility for electron microscopy at the Max Planck Institute for Neurobiology of Behavior – Caesar (Bonn) together with Carola Tröger in the group of Dr. Stephan Irsen. Grid preparation for cryo-electron microscopy and measurements were performed at the Ernst Ruska Center for microscopy and spectroscopy with electrons (Forschungszentrum Jülich) with the help of Dr. Thomas Heidler. All mass spectrometry analyses were provided by the group of Prof. Dr. Henning Urlaub at the Max Planck Institute for Multidisciplinary Sciences in Göttingen.

4.1 Functional analysis of human NLRP10 and its diseases

Among all the other NOD-like receptors, NLRP10 is remarkably different in its overall protein architecture. The typical C-terminal LRR sensory domain is absent, in its place a flexible predicted C-terminus of unknown function is present. NLRP10 was first described in 2004 as a novel regulator of apoptosis and inflammation (Y. Wang et al., 2004). In mice, NLRP10 has been reported to be expressed in various organs and tissues such as skin, testis, heart, spleen and colon (Y. Cho et al., 2024; Joly et al., 2012; Lautz et al., 2012; D. Zheng et al., 2023), whereas in humans the expression is more present in the skin (Próchnicki et al., 2023). For many years, NLRP10 was thought to act as a negative regulator of inflammatory activity by inhibiting caspase-1 and caspase-1-mediated IL-1β processing, as well as preventing ASC aggregation (Imamura et al., 2010). In 2023, new findings revealed that NLRP10 inflammasome formation occurs upon mitochondrial damage, leading to ASC speck formation and caspase-1-dependent cytokine release (Próchnicki et al., 2023). However, the underlying mechanism of this activation process remains elusive (**Figure 4-1**).

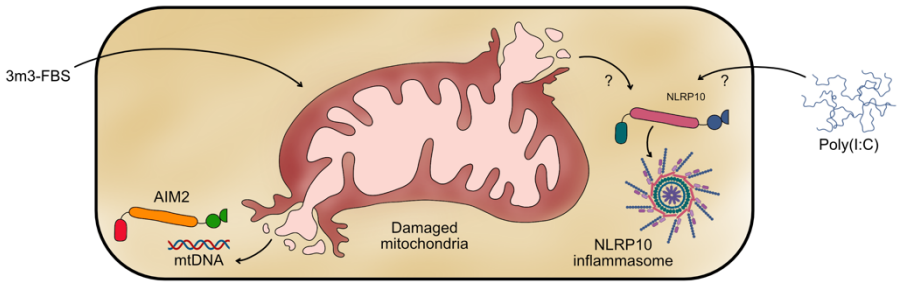

Figure 4-1: Mitochondrial damage leads to NLRP10 inflammasome activation.
Treatment with the chemical compound 3m3-FBS leads to rupture of the mitochondrial membrane, resulting in NLRP10 inflammasome activation. Other TLR ligands such as poly(I:C) are also supposed to mediate this activation. In addition to NLRP10, AIM2 inflammasome formation occurs by released mitochondrial DNA (mtDNA). This figure was modified from (Masters, 2023).

NLR proteins are known to be involved in several skin diseases. Activation of NF-κB and IL-1β release by inflammasome signaling plays a crucial role in inflammatory skin disorders. Vitiligo is an autoimmune skin disease that causes loss of skin pigmentation mediated by dysfunction of NLRP1. The closely related receptors NLRP1, NLRP3, and NLRP12 have been linked to atopic dermatitis, which causes itchy, red and swollen skin (Damm et al., 2013; Mason et al., 2011). Two other prominent examples are blau syndrome (NOD2) (Borzutzky et al., 2010) and cryopyrin-associated periodic syndromes (CAPS) (NLRP3) (Booshehri & Hoffman, 2019).

Due to the occurrence of NLRP10 in human keratinocytes, it is directly linked to skin diseases such as atopic dermatitis (AD). A genome-wide association study identified a single nucleotide polymorphism in *Nlrp10* gene causing AD in the Japanese population (Damm et al., 2013; Hirota et al., 2012). Another inflammatory skin disease caused by NLRP10 is psoriasis. Psoriasis is associated with increased risks for systemic comorbidities, including obesity, atherosclerosis, and cardiovascular disease (Verma et al., 2021).

Since the function and structure of NLRP10 are poorly described, it is a valuable target for future research to gain more insights and develop possible approaches for pharmaceutical applications.

4.2 Domain architecture and functional motifs

Human NLRP10 (hNLRP10) is a NLR family protein encoded by the *Nlrp10* gene, located on the reverse strand of chromosome 11. One sequence is described (Uniprot: Q86W26) with an additional computationally mapped potential isoform. The gene contains two protein coding exons, which is unique among the other NLR members. Other names introduced for this gene are: CLR11.1, NALP10, NOD8, PAN5, PYNOD (Ensemble: ENSG00000182261).

Human NLRP10 spans over 655 amino acids with a molecular weight of 75 kDa and a theoretical isoelectric point (pI) of 6.81. The structure determination of NLRP10 is a currently ongoing matter and in 2013, the NLRP10^{PYD} structure was determined by NMR spectroscopy (Su et al., 2013). The full-length structure has yet to be determined.

In contrast to all other NLRP proteins, NLRP10 possesses a unique domain architecture. The domain boundaries were selected based on the well characterized NLRP3 homologue due to its close relation in the phylogenetic tree. At the N-terminus, the PYD effector domain containing six alpha helices is located (aa 8-97) with an additional 7 aa short flexible loop. The FISNA domain (aa 98-166) builds the connection between the PYD and NACHT domain. For NLRP3 an additional linker is present between PYD and FISNA, which is absent for NLRP10. The central NACHT domain (aa 166-583) is mainly responsible for ATP-dependent oligomerization facilitated by conformational changes (Damm et al., 2013). In the NBD (aa 166-314) the well conserved Walker A and extended Walker B motifs for nucleotide binding are present (Brinkschulte et al., 2022). The NBD is followed by three helical domains, HD1 (aa 315-376), WHD (aa 377-482) and HD2 (aa 483-583). These domains contain important sensors for nucleotide hydrolysis. It does not contain the typical LRR domain, but instead a shorter unstructured C-terminus (aa 584-655), of which the function is unknown.

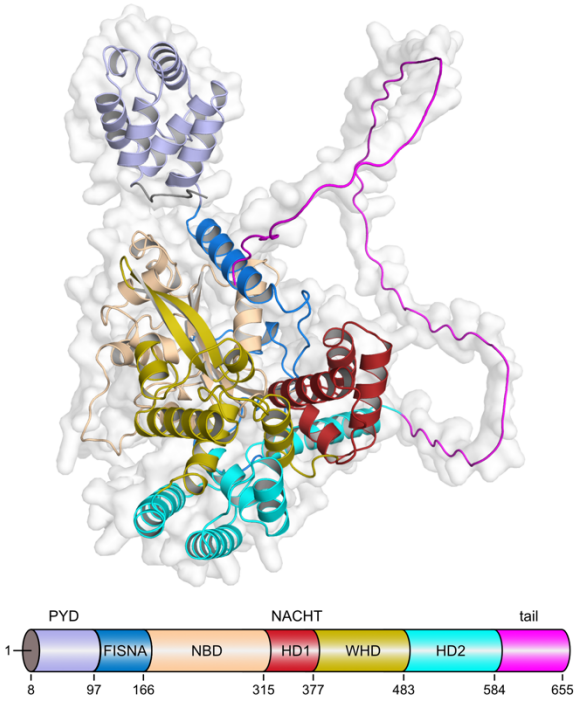

Figure 4-2: Domain architecture of human NLRP10.
AlphaFold2 model by Jumper et al.,2021 of human NLRP10 with colorized domains and corresponding domain boundaries.

4.3 Characterization of human NLRP10

4.3.1 Initial structural analysis of wild-type humanNLRP10

To gain functional and structural insights, NLRP10 was recombinantly expressed in the *Sf9* insect cell system. The N-terminally tagged MBP-fusion protein was purified by affinity chromatography using an MBPTrap with an Aekta Start system followed by size-exclusion chromatography (SEC) (**Figure 4-3a**). The chromatogram revealed two species: peak 1 eluted in the void volume corresponding to a molecular weight of 5,000+ kDa and peak 2 eluted in a higher oligomeric region (**Figure 4-3b**). The protein quality was tested by SDS-PAGE analysis (**Figure 4-3c**) and confirmed pure NLRP10 protein. Negative stain electron microscopy revealed inhomogeneous aggregated samples (**Figure 4-3d**).

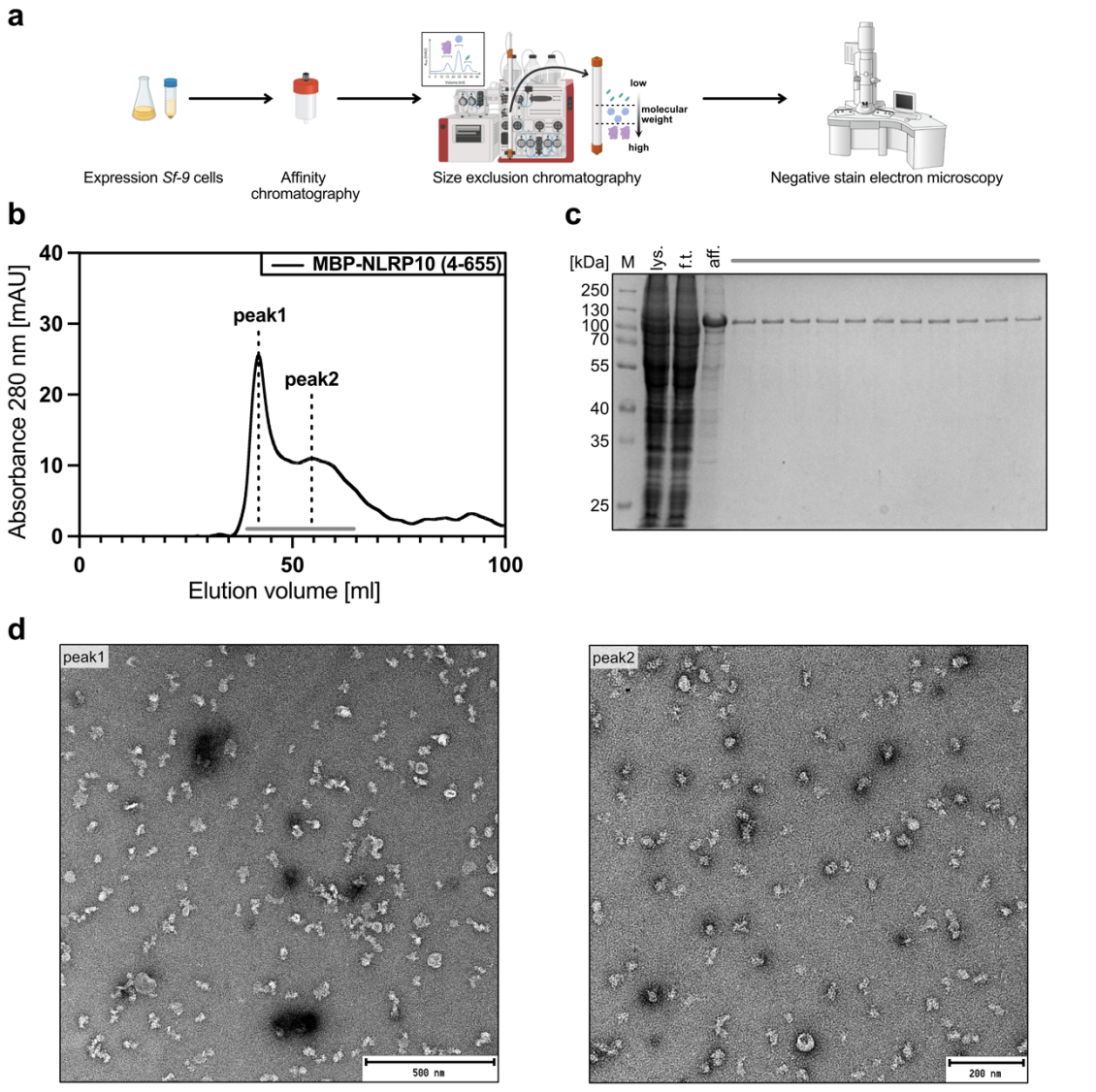

Figure 4-3: Expression and purification of human NLRP10.
*(**a**) Overview of expression and purification method of MBP-tev-NLRP10(4-655) including amylose affinity chromatography and size-exclusion chromatography as well as negative stain electron microscopy. (**b**) Chromatogram of NLRP10 injected on a Superose 6 PG XK 16/70 column after affinity purification. Peak 1 and peak 2 are indicated as well as the fractions for SDS-PAGE analysis by a grey bar. The x-axis shows the retention volume in ml and the y-axis the UV absorption at 280 nm in mAU. (**c**) Coomassie-stained SDS-PAGE analysis with samples from (b), M: marker, lys.: lysate, f.t.: flow through, aff.: sample after affinity chromatography. (**d**) Negative stain EM images after SEC of peak 1 and peak 2.*

Due to aggregation and low protein yield in the purification of wild-type NLRP10, new constructs had to be designed, to create more stable expression constructs.

4.3.2 C-terminal truncations in human NLRP10

4.3.2.1 Structure analysis and construct design

The AlphaFold2 model of NLRP10 (Jumper et al., 2021; Varadi et al., 2023) was used to investigate new constructs for human NLRP10. It is appropriate to design new constructs based on the predicted folding structure to ensure that conserved structural motifs are not disrupted. Therefore, two C-terminal truncations were designed to test for better stability and solubility (**Figure 4-4**). The first construct lacks the flexible C-terminal domain resulting in the boundaries 4-583. The second construct is also missing the C-terminal domain and in addition, the helical domain 2 (HD2) resulting in the boundaries 4-482.

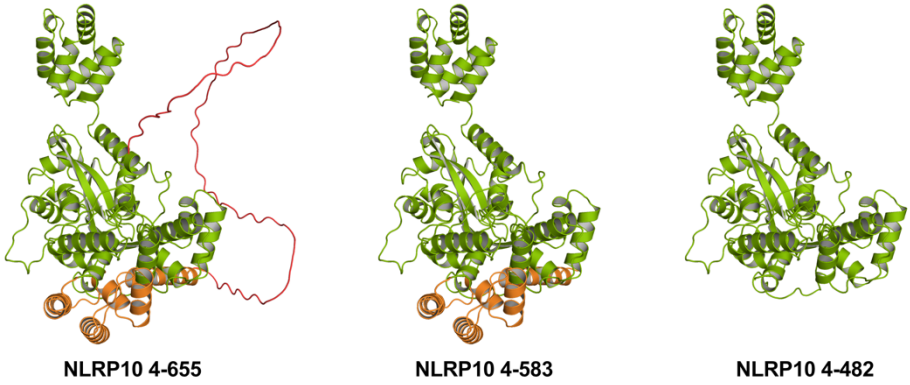

Figure 4-4: New construct design for NLRP10.
AlpahFold2 models of human NLRP10 (Jumper et al., 2021; Varadi et al., 2023) . Three different expression constructs are shown. Green: aa 4-482, green+orange: aa 4-583, green+orange+red: aa 4-655.

4.3.2.2 Expression and purification of C-terminal truncations

Both C-terminal truncation constructs (4-583) and (4-482) were expressed as N-terminally tagged MBP-fusion proteins in the *Sf9* insect cell system. They were purified by MBP affinity chromatography, followed by size-exclusion chromatography (SEC). The SEC profiles are shown in **Figure 4-5a,c**. The respective Coomassie-stained SDS gels proves the purity of purified protein **Figure 4-5b,d**. For construct **4-583** the protein eluted mainly in the void fraction (red), indicating a high degree of aggregation. There was a small shoulder present (green) and a small monomeric fraction (yellow) (**Figure 4-5a,b**). The overall yield was lower than for the second construct. Nevertheless, all fractions contained MBP-tev-NLRP10 (4-583) (MW: 108.3 kDa). For construct **4-482** the aggregated fraction in the void volume (red) was approximately the same amount, but the lower oligomeric/monomeric fractions (yellow) were high in yield (**Figure 4-5c,d**). All fractions contained MBP-tev-NLRP10 (4-482) (MW: 96.3 kDa). These results showed a better solubility and stability for construct **4-482** that could be purified to homogeneity.

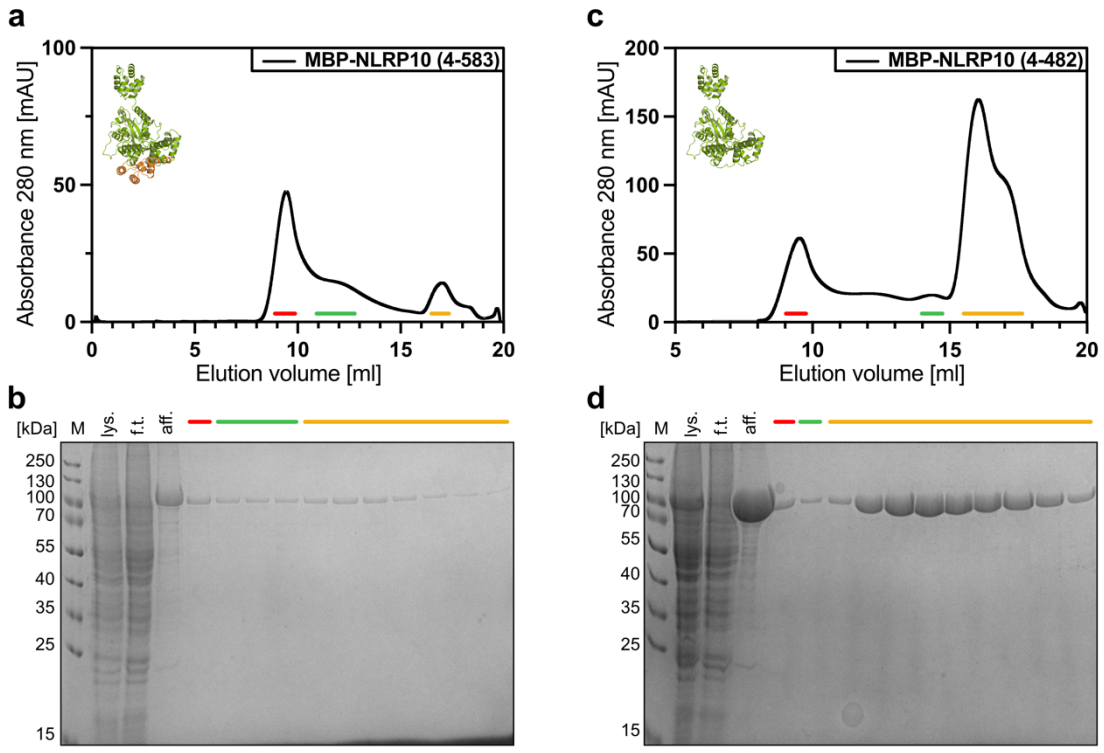

Figure 4-5: Purification of C-terminal truncations in human NLRP10.
*(**a**) Chromatogram of MBP-tev-NLRP10 (4-583) injected on a Superose 6 Increase 10/300 column after affinity purification. Different fractions for SDS-PAGE analysis are indicated by colored bars. The x-axis shows the retention volume in ml and the y-axis the UV absorption at 280 nm in mAU. (**b**) Coomassie-stained SDS-PAGE analysis with samples from (a), M: marker, lys.: lysate, f.t.: flow through, aff.: sample after affinity chromatography. (**c**) Chromatogram of MBP-tev-NLRP10 (4-482) injected on a Superose 6 Increase 10/300 column after affinity purification. Different fractions for SDS-PAGE analysis are indicated by colored bars. The x-axis shows the retention volume in ml and the y-axis the UV absorption at 280 nm in mAU. (**d**) Coomassie-stained SDS-PAGE analysis with samples from (c), M: marker, lys.: lysate, f.t.: flow through, aff.: sample after affinity chromatography.*

For construct **4-482** a double peak was observed at 16-17 ml elution volume. To further analyze this fraction, a new column size was chosen, to achieve a better separation of the two fractions. Thus, a Superdex 200 column was used instead of a Superose 6 column. In

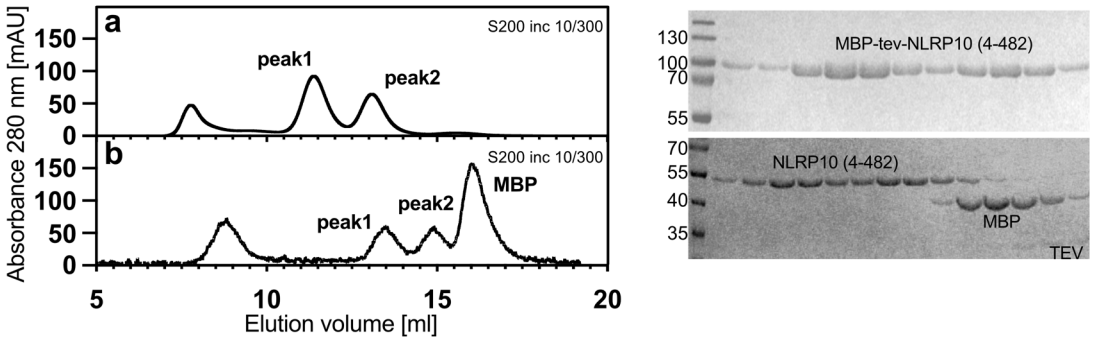

Figure 4-6: Optimization of the NLRP10 (4-482) purification process.
*(**a**) Chromatogram of MBP-tev-NLRP10 (4-482) injected on a Superose 6 Increase 10/300 column after affinity purification. The x-axis shows the retention volume in ml and the y-axis the UV absorption at 280 nm in mAU. On the right, a Coomassie-stained SDS-PAGE analysis shows corresponding samples. (**b**) Chromatogram of MBP-tev-NLRP10 (4-482) after TEV digest overnight injected on a Superose 6 Increase 10/300 column after affinity purification. The x-axis shows the retention volume in ml and the y-axis the UV absorption at 280 nm in mAU. On the right, a Coomassie-stained SDS-PAGE analysis shows corresponding samples.*

Figure 4-6a, the chromatogram showed indeed a separation into two fractions, confirmed by SDS-PAGE analysis. Also, an overnight TEV cleavage maintained the two-peak separation, allowing further experiments regarding crystallization and size determination (**Figure 4-6b**).

4.3.2.3 C-terminal truncated NLRP10 forms a dynamic monomer-dimer equilibrium

The purification of MBP-tev-NLRP10 (4-482) revealed two defined species in size-exclusion chromatography. To further investigate these two species, a SEC-MALS measurement was conducted. Either MBP-tagged NLRP10 (4-482) or TEV cleaved sample was used. For both measurements two species could be observed. The MBP-tagged sample showed molecular weights of 192 kDa for peak 1 and 101 kDa for peak 2. The theoretical calculated molecular mass of an MBP-NLRP10 (4-482) monomer is 96.2 kDa. This result shows the formation of monomers and dimers in solution during the purification of MBP-NLRP10 (4-482). The TEV cleaved sample showed molecular weights of 109 kDa for peak 1 and 55 kDa for peak 2, indicating the same behavior in solution independent of the tag. The theoretical calculated molecular mass of NLRP10 (4-482) monomer is 54.8 kDa (**Figure 4-7a**).

To further analyze the ratio between monomeric and dimeric fractions, different initial concentrations (0.75 mg/ml, 1.5 mg/ml, 3.0 mg/ml) were injected to a Superdex 200 10/300 column. The ratio was related to the protein concentration. The higher the concentration, the more dimeric fraction was observed (**Figure 4-7b**).

Next the influence of the salt concentration in the purification buffer was tested. With higher concentrations of NaCl in the buffer, the monomeric fraction was preferred. Additionally, a shift in the elution volume occurred due to the increased amount of the monomeric fraction (**Figure 4-7c**).

HPLC measurements were used to test the protein stability of the pooled fractions. Peak 1 and peak 2 (**Figure 4-6**) were injected separately to a Superdex 200 3.2/300. It was observed that peak 1 dissociates again to a monomeric species, whereas peak 2 remains monomeric. This was also the case after incubation for one day at 4 °C, indicating no time dependency. Finally, a 4x increase in concentration also showed no change in the HPLC profile (**Figure 4-7d-f**). These measurements have all shown that the dimeric fraction is dissociating into a monomeric fraction. However, this process is not reversible.

The C-terminal truncated construct of NLRP10 was further used to set up crystallization trials because it was possible to reach concentrations up to 10 mg/ml. A couple of commercially available screens were used and some conditions led to small crystal formation. Unfortunately, these crystals didn't show any diffraction patterns upon X-ray analysis at DESY, Hamburg. Consequently, we are currently developing additional optimization strategies to enhance crystal growth and quality.

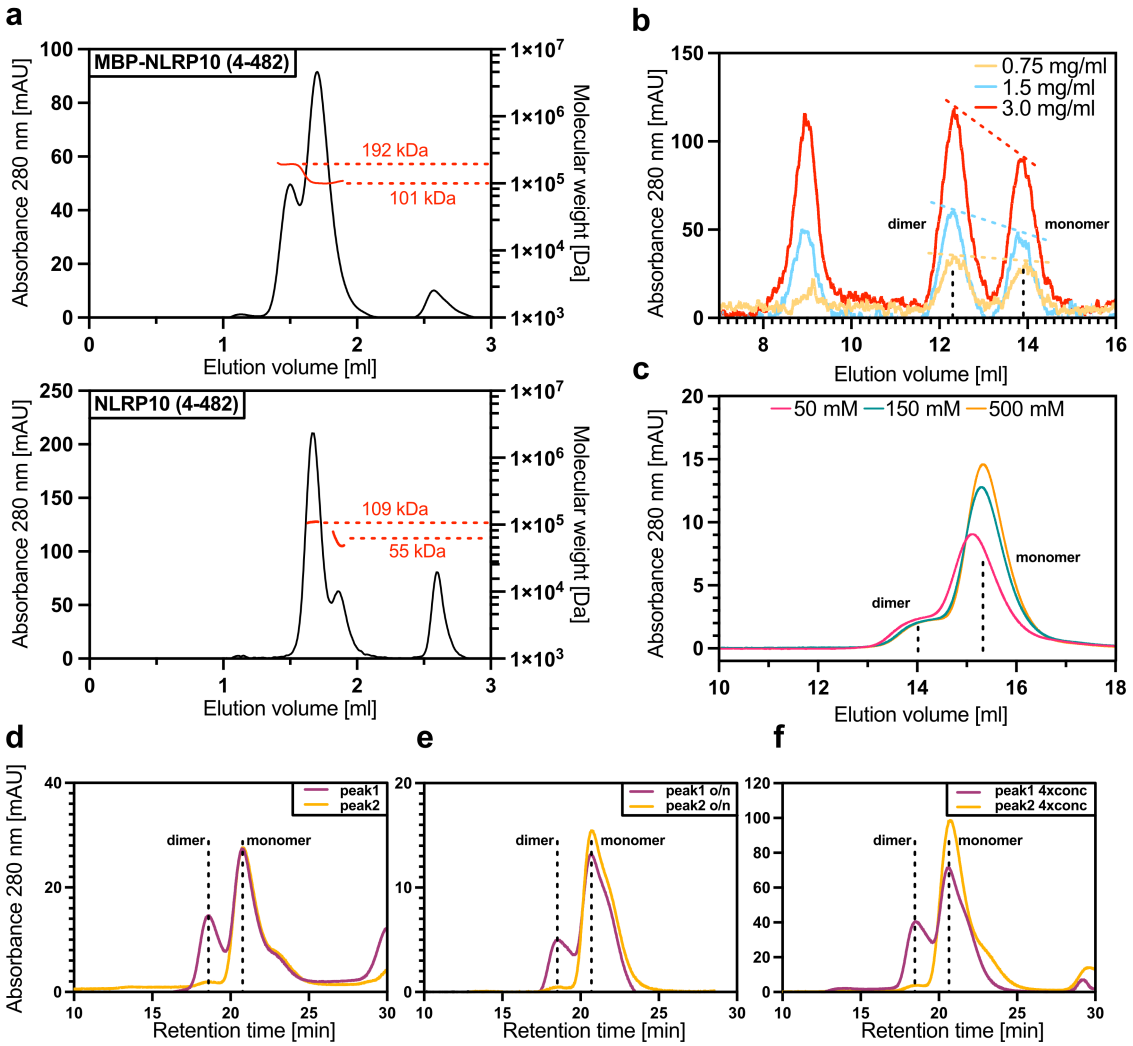

Figure 4-7: NLRP10 (4-482) forms a dynamic monomer-dimer equilibrium.
*(**a**) MALS measurements of either MBP-NLRP10 (4-482) or NLRP10 (4-482) injected on a Superdex 200 5/150 column. The measured molecular weight is indicated in red. The x-axis shows the retention volume in ml and the left y-axis the UV absorption at 280 nm in mAU. The right y-axis shows the molecular weight in Da. (**b**) Several SEC runs with different concentrations (0.75 mg/ml, 1.5 mg/ml, 3.0 mg/ml) of MBP-NLRP10 (4-482). The x-axis shows the retention volume in ml and the y-axis the UV absorption at 280 nm in mAU. (**c**) Several SEC runs with different NaCl concentrations (50 mM, 150 mM, 500 mM) in the purification buffer. NLRP10 (4-482) after TEV cleavage was used. The x-axis shows the retention volume in ml and the y-axis the UV absorption at 280 nm in mAU. (**d-f**) HPLC measurements of MBP-NLRP10 (4-482) injected on a Superdex 200 3.2/300 column. Either pooled peak 1 or peak 2 from previous purifications were used. The x-axis shows the retention volume in ml and the y-axis the UV absorption at 280 nm in mAU.*

4.3.3 Investigation of membrane binding features

To gain deeper insights into the function of NLRP10, the C-terminus was further investigated to examine the influence during the activation process. Therefore, a detailed analysis of the amino acid sequence (aa584 - aa655) was done and a high isoelectric point (pI) of this region was observed. In total 13 basic amino acids (Lys/Arg) are distributed all over the entire C-terminus. All of these residues were mutated to glutamine in order to maintain steric and polar properties. The pI changed from 9.52 to 4.21 in the C-terminus and from 6.85 to 5.71 for the whole protein (**Figure 4-8a**).

N-terminal tagged MBP-NLRP10 (4-655) C-tail mutant was expressed in the *Sf9* insect cell system. It was purified by MBP affinity chromatography, followed by size-exclusion chromatography (SEC). The SEC profile revealed two species, void volume fraction (**1**) and oligomeric fraction (**2**). The Coomassie-stained SDS gel confirms the purity of the purified protein. Both fractions were further analyzed by negative stain EM and showed different homogeneity and particle shape (**Figure 4-8b,c**).

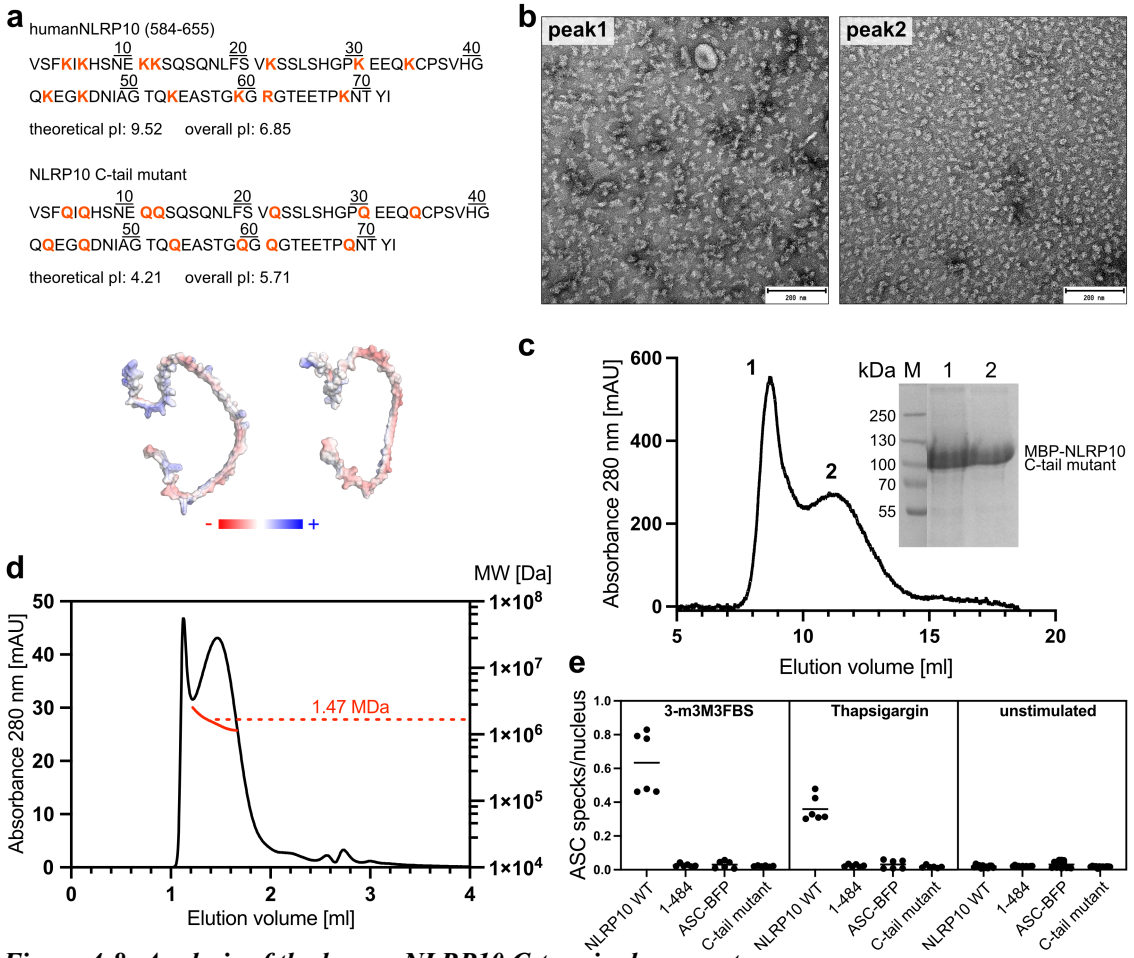

Figure 4-8: Analysis of the humanNLRP10 C-terminal segment.
*(**a**) Sequence analysis of humanNLRP10 C-terminus. Mutated amino acids are highlighted in orange and the calculated isoelectric points (pI) are shown. Graphic illustration of the C-terminus with calculated electrostatics is shown for wt (left) and C-tail mutant (right). (**b**) Negative stain electron microscopy images of MBP-NLRP10 C-tail mutant peak 1 and peak 2. (**c**) Chromatogram of MBP-NLRP10 C-tail mutant injected on a Superose 6 Increase 10/300 column after affinity purification. The x-axis shows the retention volume in ml and the y-axis the UV absorption at 280 nm in mAU. The two resulting species are indicated. On the right, a Coomassie-stained SDS-PAGE analysis shows corresponding samples. (**d**) MALS measurement of MBP-NLRP10 C-tail mutant injected on a Superose 6 Increase 5/150 column with a measured mass of 1.47 MDa. (**e**) ASC speck assay of different constructs using either stimulated or unstimulated cells. ASC specks per nucleus are evaluated.*

A MALS measurement revealed a molecular weight of 1.47 MDa on average. Within the evaluated peak, the molecular weight ranges from 1.6 – 1.2 MDa, indicating an influence by the void volume fraction. The measured weight would refer to a dodecamer (**Figure 4-8d**). The influence of the NLRP10 C-terminus regarding the activation was evaluated by ASC speck measurements performed by Dr. Dennis de Graaf. Samples of NLRP10 wt treated with either 3-m3M3FBS or thapsigargin, which causes mitochondrial damage, showed an ASC specking rate of between 0.4 and 0.6 specks per nucleus. This indicates the NLRP10 mediated inflammasome activation. Neither the deletion of NLRP10 C-terminus (1-484) nor the C-tail mutant resulted in ASC speck formation, indicating that this domain is crucial for inflammasome activation. The ASC-BFP control sample also showed no activation (**Figure 4-8e**).

4.3.4 Characterization of novel NLRP10 binding partners

Not much is known to date about activation triggers or potential binding partners of NLRP10. Therefore, we collaborated with the group of Prof. Dr. Thomas Kufer (University of Hohenheim) and they were able to identify different potential hits by an interactome analysis of NLRP10. Two of the identified proteins belong to the mammalian TELO2-TTI1-TTI2 (TTT) ternary complex, known to assemble and stabilize phosphatidylinositol 3-kinase-related protein kinases (PIKKs) (Y. Kim et al., 2022). Telomere length regulation protein 2 (TELO2) and Tel2-interacting protein 1 (TTI1) were found in the interactome analysis. Additionally, FAS-associated factor 2 (FAF2) was identified. FAF2 was found as a membrane-associated cofactor of p97/VCP that localizes to different organelles such as mitochondria or the endoplasmic reticulum (ER) (Koyano et al., 2024). The cryo-EM structure of the TTT complex and the AlphaFold model of FAF2 are shown in **Figure 4-9**.

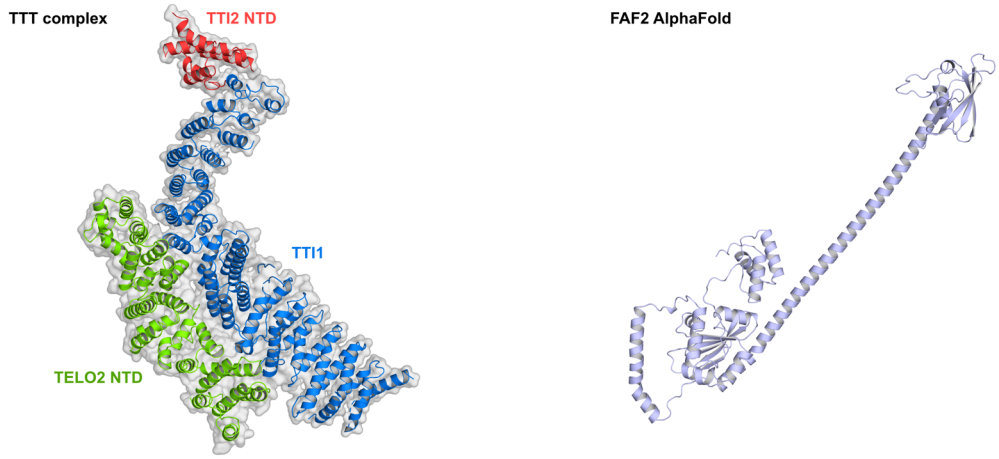

Figure 4-9: Investigated binding partners of NLRP10.
Cryo-EM structure of the human TTT complex at 4.2 Å (left) (PDB: 7F4U) (Y. Kim et al., 2022). Different proteins are colored: TELO2 NTD (green), TTI2 NTD (red) and TTI1 (blue). AlphaFold model of human FAF2 (right) (Varadi et al., 2023).

The first aim was to prove the in-vitro binding of interaction partners to recombinantly expressed humanNLRP10. Therefore, TELO2, TTI1 and FAF2 were cloned in the *Sf9* cell expression vector pACEBac1 to recombinantly express them as GST fusion proteins. A GST tag was selected to create the possibility to use different anchors for later pull-down experiments with MBP-tagged NLRP10.

A co-expression approach was chosen to investigate possible binding of the interaction partners to NLRP10. *Sf9* cells were infected with NLRP10wt virus as well as the individual corresponding interaction partner viruses. They were purified by MBP affinity chromatography, followed by size-exclusion chromatography (SEC). The resulting chromatograms showed a similar profile to the NLRP10wt purification with a sharp void volume peak (peak 1) and a smaller oligomeric shoulder (peak 2). Coomassie stained SDS-PAGE analysis and western blot analysis were performed to visualize different proteins. NLRP10 was observed in all fractions, whereas the interaction partners were mainly detectable in peak 1. Only FAF2 was clearly visible in peak 2, indicating either a better expression or better binding properties (**Figure 4-10**). Nevertheless, all proteins were expressed and detectable upon MBP affinity chromatography supporting the results of the interactome analysis.

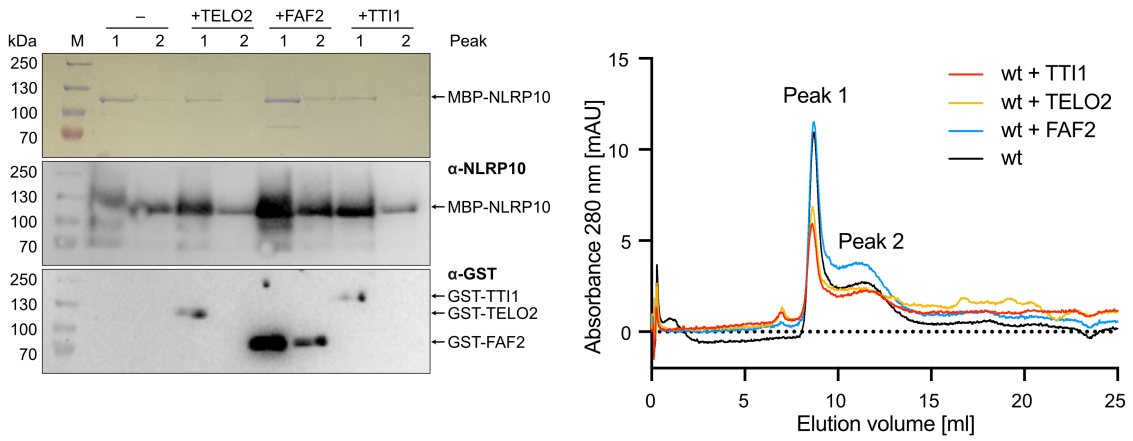

Figure 4-10: Co-expression of humanNLRP10 with potential interaction partners.
Purification of co-expressions of either TELO2, TTI1 or FAF2 (GST) with humanNLRP10 (MBP). SEC chromatograms are shown on the right site with indicated peak 1 and peak 2. The x-axis shows the retention volume in ml and the y-axis the UV absorption at 280 nm in mAU. Coomassie stained SDS-PAGE analysis and western blot analysis is shown on the left. Primary antibodies for NLRP10 and GST were used.

4.3.5 ATPase activity of NLRP10

NOD-like receptors are part of the AAA+ ATPase protein family. ATP hydrolysis plays a crucial role in NLR activity and function and can generate the mechanical force necessary to induce conformational changes, leading to downstream signaling cascades. Within the NLR family, ATP interactions were investigated for various receptors, such as NLRP1 (Bauernfried et al., 2021), NLRP3 (Brinkschulte et al., 2022), and NLRP12 (Ye et al., 2008). Because of its close relation to other members, it was also thought that NLRP10 could hydrolyze ATP. In NLRP10, the typical Walker A and Walker B motifs described for nucleotide hydrolysis, were observed and characterized. Several residues are expected to interact with the nucleotide during the hydrolysis process. K179 is the most prominent in the Walker A motif, and D249, D252, and E253 are the most prominent in the Walker B motif (**Figure 4-11a,b**).

To investigate ATP hydrolysis activity of NLRP10, a HPLC based ATP hydrolysis assay was conducted. Previously purified proteins were incubated with ATP, and conversion from ATP to ADP was monitored over time by UV absorption. The activity of wild-type NLRP10 and NLRP10 (4-482) was measured at peak 1 and peak 2. For wild-type peak 1, a hydrolysis rate of ~ 30 % was measured, whereas peak 2 showed slightly reduced activity of ~ 20 %. For NLRP10 (4-482), the activity was even smaller with ~ 10 % for peak 1 and ~ 5 % for peak 2 (**Figure 4-11c**).

Two mutations in the Walker motifs were cloned and expressed in *Sf9* cells and subsequently measured regarding ATP hydrolysis. The K179A mutation (Walker A) and the D249A mutation (Walker B) both showed a significant decrease in hydrolysis activity of ~10 % compared to the wild-type NLRP10 (**Figure 4-11d**). The mutations of D252 and E253 are currently under investigation.

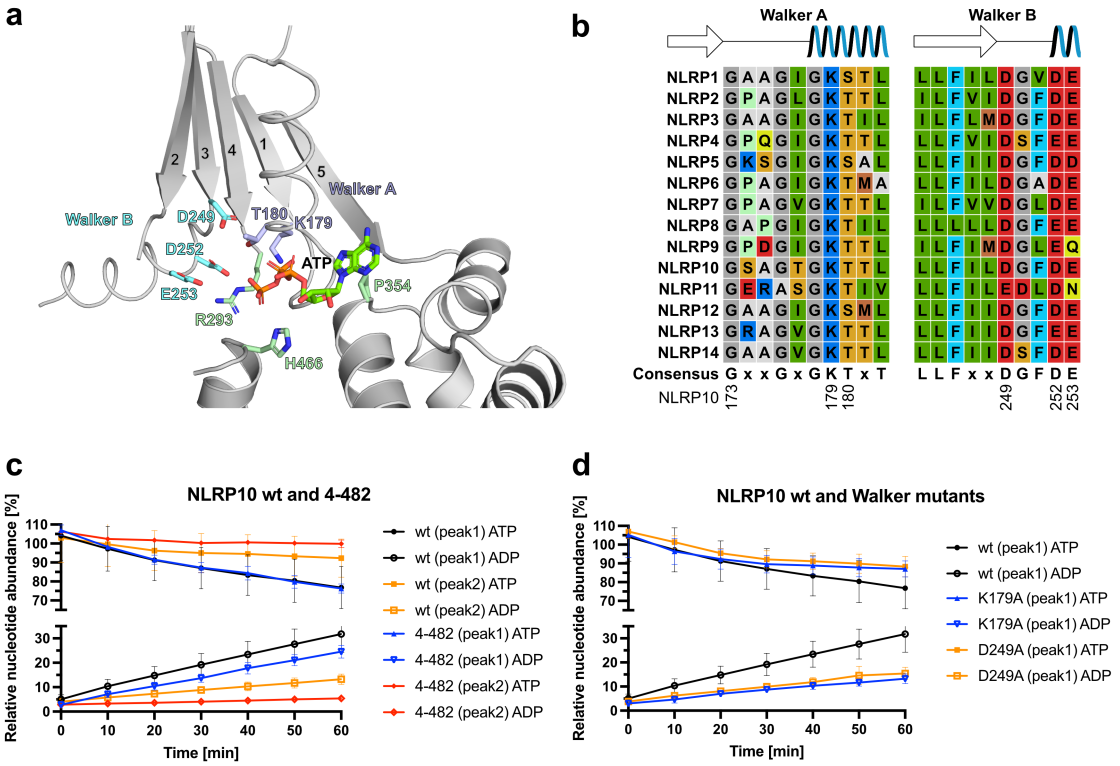

Figure 4-11: Analysis of Walker A/B binding motifs in NLRP10 and ATP hydrolysis measurements. *(**a**) A cartoon of the nucleotide-binding site of NLRP10 including ATP is shown based on the structure prediction of AlphaFold. The Walker A and B motifs as well as two sensors are indicated. The figure is based on previous results for NLRP3 (Brinkschulte et al., 2022). (**b**) Sequence alignments of the Walker A and B motifs of all NLRP proteins. The consensus is shown and important residues are indicated. (**c**) Wild-type NLRP10 and NLRP10 (4-482) were analyzed by RP-HPLC. Peak 1 and peak 2 are plotted for ATP and ADP. All measurements are normalized to an ATP and ADP standard. (**d**) Wild-type NLRP10 and Walker A and B mutants were analyzed by RP-HPLC. All measurements are normalized to an ATP and ADP standard.*

4.3.6 PYD mutational studies

The pyrin domain of different NLRP family members such as NLRP3 and NLRP6 was shown to be involved in the oligomerization and thereby activation of the respective receptors (Hochheiser, Behrmann, et al., 2022; Shen et al., 2019). The formation of a nucleation platform for ASC, which leads to the formation of large ASC filaments, is dependent on a specific arrangement of these PYD domains. The overall fold of PYD domains is highly conserved and builds a 6-α-helical bundal fold. Also, the amino acid sequences show similarities, albeit the NLR PYDs have a higher consensus (**Figure 4-12**).

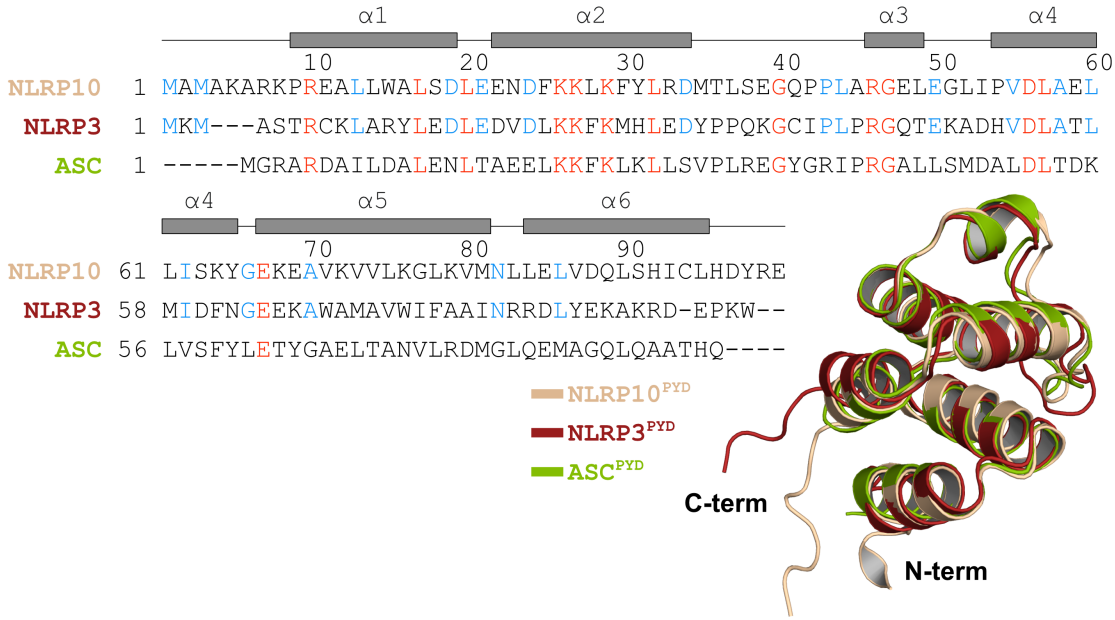

Figure 4-12: PYD sequence alignment.
Sequence alignment of NLRP10^{PYD}, NLRP3^{PYD} and ASC^{PYD}. The secondary structural elements of NLRP10 are indicated. Identical residues between all proteins are marked in red. Identical residues between NLRP10 and NLRP3 are marked in blue. The identity between NLRP10^{PYD} and NLRP3^{PYD} is 33 %. A structure alignment of indicated PYDs is shown.

Two members of the NLRP protein family, NLRP3 and NLRP6, can form PYD filaments on their own. This ability has not been described for the other members. DLS measurements were performed to investigate the self-oligomerization of different NLR-PYDs. NLRP3^{PYD} and NLRP6^{PYD} showed a strong oligomerization after a few minutes. For ASC-mCherry the oligomerization rate was smaller, but still present. NLRP1^{PYD} and NLRP10^{PYD} showed no oligomerization within one hour (**Figure 4-13a**). Thus, it is likely that the inflammasome formation follows a different mechanism compared to NLRP3 and NLRP6.

In order to gain insights into the interaction between NLRP10^{PYD} and ASC^{PYD}, the amino acid sequence of NLRP3 and NLRP10 was compared (**Figure 4-12**) and together with the structure prediction of NLRP10, two residues (Lys27 and Glu85) were selected to be mutated. These residues are supposed to be in the correct location to form the ASC binding interface. The mutations were designed as a charge inversion (Lys27→Glu, Glu85→Arg) to disrupt a potential interface (**Figure 4-13b**).

The N-terminally tagged MBP-NLRP10 (4-655) K27E/E85R mutant was expressed in the *Sf9* insect cell system. It was purified by MBP affinity chromatography, followed by

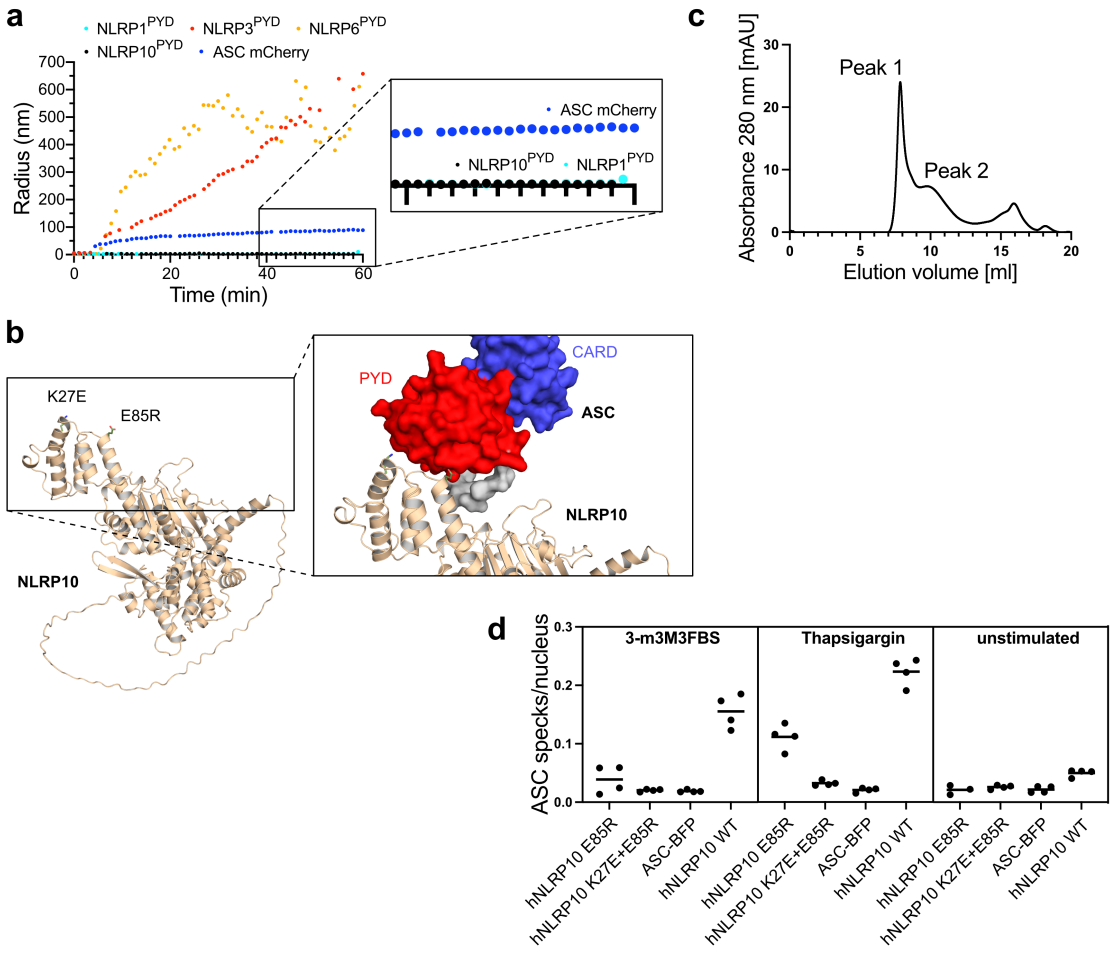

Figure 4-13: NLRP10^{PYD} mutations and ASC speck formation.
*(**a**) DLS measurements of several NLR PYD domains (NLRP1, NLRP3, NLRP6 and NLRP10) and ASC-mCherry. Measurements were performed for 1 hour at 25 °C. The x-axis shows the measurement time in min and the y-axis the particle radius in nm. Measurements of NLRP3, NLRP6 , and ASC were provided by Isabell Jamitzky. (**b**) AlphaFold prediction of NLRP10 with ASC with indicated residues in the potential binding interface. (**c**) SEC chromatogram of MBP-NLRP10 (4-655) K27E/E85R injected on a Superose 6 Increase 10/300 column. The x-axis shows the retention volume in ml and the y-axis the UV absorption at 280 nm in mAU. (**d**) ASC speck assay of either single or double NLRP10^{PYD} mutant. Samples were either stimulated with 3-m3M3FBS or thapsigargin or unstimulated. ASC-BFP and NLRP10wt were used as controls. ASC specks per nucleus are evaluated.*

size-exclusion chromatography (SEC). The SEC profile revealed two species, void volume fraction (**1**) and oligomeric fraction (**2**), similar to NLRP10 wt. Since there is no change regarding the elution profile, it is likely that the PYD mutations did not affect the protein behavior in solution (**Figure 4-13c**).

The influence of the NLRP10^{PYD} regarding the activation was evaluated by ASC speck measurements performed by Dr. Dennis de Graaf. Samples of NLRP10 wt treated with either 3-m3M3FBS or thapsigargin showed an ASC specking rate of around 0.2 specks per nucleus. In contrast, the single mutation E85R showed reduced ASC specking and the double mutation K27E/E85R showed no ASC specks. The same was observed for the ASC-BFP control (**Figure 4-13d**). These results suggest that the interaction to ASC is mediated by K27 and E85 similarly as it is found in NLRP3, although it was not possible to observe the self-assembly of NLRP10^{PYD} into a filament.

4.4 Discussion and conclusion

Over the last few years, NLRP10 gained more and more attention in innate immunity research, but knowledge of its function on a molecular level is currently very limited. The number of publications on NLRP10 (64) is relatively low compared to other NLRPs, such as NLRP1 (1,179) or NLRP3 (26,353) (pubmed.ncbi.nlm.nih.gov, Sept. 2025). Various skin diseases, including atopic dermatitis and psoriasis, are primarily associated with NLRP10, but the mode of action is elusive. Therefore, it is of great interest to gain more insights in the protein biochemistry of NLRP10.

To investigate structural and functional aspects of the NLRP10 protein, it was recombinantly expressed in *Sf9* insect cells. The MBP-tagged fusion protein occurred in two species, void volume (peak 1) and oligomeric shoulder (peak 2). Tag cleavage led to reduced protein solubility and stability, so it was not accomplished for further applications. Initial particle analysis by negative stain EM revealed aggregated and unstructured particles, not suitable for further structure determination (**Figure 4-3**). It was likely that the flexible predicted C-terminus caused the high degree of protein aggregation. Thus, two truncated constructs were designed to test the influence of the C-terminus regarding protein behavior during purification. The construct NLRP10 (4-482), lacking the C-terminus and HD2, resulted in high yields of either monomeric and dimeric species. In contrast, NLRP10 (4-583), lacking the C-terminus, showed the same elution profile as full-length NLRP10 (4-655), so the HD2 is involved somehow in the aggregation process (**Figure 4-5**, **Figure 4-6**). The usage of truncated protein constructs is a commonly used approach to gain better access to protein structures by X-ray crystallography or cryo-EM (Dekker et al., 2021; McBride et al., 2022; Shi et al., 2024). Initial crystallization trials for NLRP10 (4-482) led to small crystal formation, insufficient for analysis. Further optimization is needed, and also small molecules or other binders could improve the crystallization process.

This C-terminal domain of NLRP10 is predicted to be flexible and is thought to be crucial in NLRP10 activation. It is a unique feature among the NLR family, where all other members carry a highly conserved LRR region (Sundaram et al., 2024). It is of great interest to know more about this specific domain, to understand its role for either NLRP10 inhibition or activation. Therefore, a detailed sequence analysis revealed a high positive charge in the C-terminus, caused by twelve lysine and one arginine residue. This charge could lead to binding of any negatively charged entity within the respective cells, such as nucleic acids or membranes. Mutation of the 13 positively charged residues to glutamines led to a drastic increase in protein yield, as well as more particle homogeneity in negative stain EM analysis. Nevertheless, the elution profile was of similar shape compared to wild-type NLRP10 (**Figure 4-8**).

Negative stain EM analysis of wild-type NLRP10 revealed the presence of larger particles, some of which were round, indicating potential liposomes or other membrane particles derived from cell lysis. The reduction of these particles in the C-tail mutant was attributable to the loss of membrane binding ability by removing the positive charges. Additionally, membrane binding explains the lower yield of wild-type NLRP10 during purification, because it likely sticked to the cell pellet, thereby separating it from the supernatant. The idea of membrane binding is supported by recent publications about activation of NLRP10 by mitochondrial damage (Próchnicki et al., 2023; D. Zheng et al., 2023). Thus, it would be possible that NLRP10 senses damaged mitochondrial membranes in the cytoplasm and thereby gets activated. Furthermore, ASC speck activation assays showed complete loss of speck formation (**Figure 4-8**).

Both, C-terminal truncation and C-tail mutant, did not show ASC oligomerization upon treatment with mitochondria damaging agents. Thus, the platform for ASC nucleation was not present anymore, supporting the hypothesis of membrane binding as an oligomerization platform.

Nucleotide hydrolysis function was shown to be important for NLR protein functions and conformational rearrangements (Bauernfried et al., 2021; Brinkschulte et al., 2022; Ye et al., 2008). NLRP10 was also tested for ATP hydrolysis in HPLC based assays. It was observed that wild-type NLRP10 was active either in peak 1 or peak 2. Both fractions represent oligomeric samples. In contrast, NLRP10 (4-482) exhibited reduced activity, particularly in the monomeric fraction (peak 2) (**Figure 4-11**). This finding is consistent with previous observations regarding other NLRs. However, the hydrolysis activity of NLRP10 is lower compared to NLRP3 (Brinkschulte et al., 2022). A reduced hydrolysis rate was observed for two Walker mutants, indicating the importance of the steric arrangement in the nucleotide binding pocket. Further experiments are needed to investigate how these mutations affect the mechanism and function of NLRP10 activation.

The inflammasome complex formation of NLR proteins is highly regulated and dependent on rigorous oligomerization. Either the PYD or the CARD domain of ASC is interacting with the respective effector domains in the oligomeric NLR complex. In the human NAIP/NLRC4 inflammasome this interaction is mediated by CARD-CARD interactions (Matico et al., 2024), whereas in the NLRP3 inflammasome the interaction takes place between the PYD domains (Xiao et al., 2023).

To investigate whether NLRP10 does also form an inflammasome mediating ASC oligomerization via PYD-PYD interactions, a detailed analysis of the $NLRP10^{PYD}$ was implemented. An alignment between $NLRP10^{PYD}$ and $NLRP3^{PYD}$ showed numerous similar residues (**Figure 4-12**), and a detailed analysis of the NLRP3 inflammasome suggested two prominent amino acids (Lys24 and Asp82) indispensable for ASC binding (Hochheiser, Behrmann, et al., 2022). In the NLRP10 sequence the respective residues are Lys27 and Glu85 and a structure alignment displayed the similar location and orientation compared to NLRP3. Again, ASC speck assays were conducted to investigate the influence of these two residues during activation. It was observed that a charge inversion mutant (K27E and E85R) led to complete inhibition of ASC oligomerization, indicating a similar oligomerization mechanism in the transition from $NLRP10^{PYD}$ nucleation seeds to ASC^{PYD} filament elongation as shown for NLRP3 (Hochheiser, Behrmann, et al., 2022; Xiao et al., 2023).

It was noticed that NLRP10 is missing the loop between the PYD and FISNA domains, and different AlphaFold predictions modeled the connection as a long straight helix. This results in a loss of flexibility and is another indication that NLRP10 needs a nucleation platform to adapt a suitable arrangement for ASC oligomerization. Compared to $NLRP3^{PYD}$ and $NLRP6^{PYD}$, the $NLRP10^{PYD}$ did not form filaments on their own, even at high concentrations (**Figure 4-13**). Thus, NLRP10 does need a cell entity, such as a membrane, to form an inflammasome complex. In contrast, NLRP3 and NLRP6 are capable of forming inflammasomes independently in the cytosol upon activation by specific triggers.

Taken together, the previously discussed results led to a proposed activation mechanism for the NLRP10 inflammasome (**Figure 4-14**). The first step would be the display of a cell membrane, likely negatively charged. One such possibility is the negatively charged inner mitochondrial membrane, which would be present upon

mitochondria rupture. It contains a high amount of cardiolipin, characteristic for this membrane. NLRP10, present in the cytosol, is able to attach to the membrane and form oligomers as nucleation platform for ASC. Since the PYD does not oligomerize itself, it is probable that the NACHT domains build interactions between each other to create the right symmetry for ASC oligomerization. Once the platform is created, ASC will polymerize and activate caspase-1. Subsequently, pro-inflammatory cytokines and gasdermins are cleaved resulting in pyroptosis. This pathway is well described for NLRP3 activation (Swanson et al., 2019).

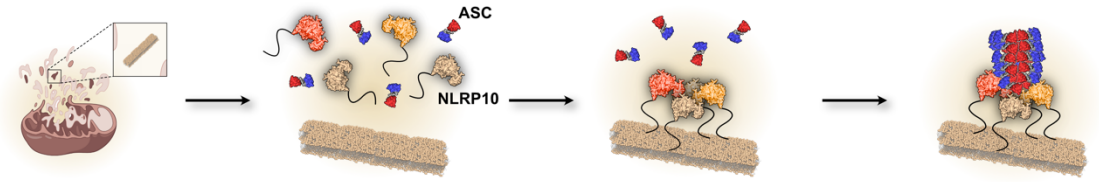

Figure 4-14: Proposed activation mechanism of NLRP10.
Mitochondrial damage leads to display of the negatively charged inner mitochondrial membrane. NLRP10 attaches to the membrane and forms an oligomer as a nucleation platform for ASC. ASC polymerization takes place to induce further signaling cascades.

Since all purifications of full-length NLRP10 constructs resulted in a similar size exclusion chromatography profile, MALS measurements were performed to determine the size of the oligomeric shoulder (peak 2). The C-tail mutant revealed a molecular weight of 1.2-1.6 MDa (**Figure 4-8**). Also, measurements for the PYD mutants in full length NLRP10 showed similar values. The size refers to a hypothetical dodecamer. STAND proteins, including NLRP10, have been shown to form hexameric assemblies (Wendler et al., 2012). Therefore, it is possible that NLRP10 forms a dodecamer consisting of two hexamers in an inactive state. Once activated by a membrane, NLRP10 could form a hexamer arranged by its positively charged C-terminus and creates a platform for ASC oligomerization (**Figure 4-15**).

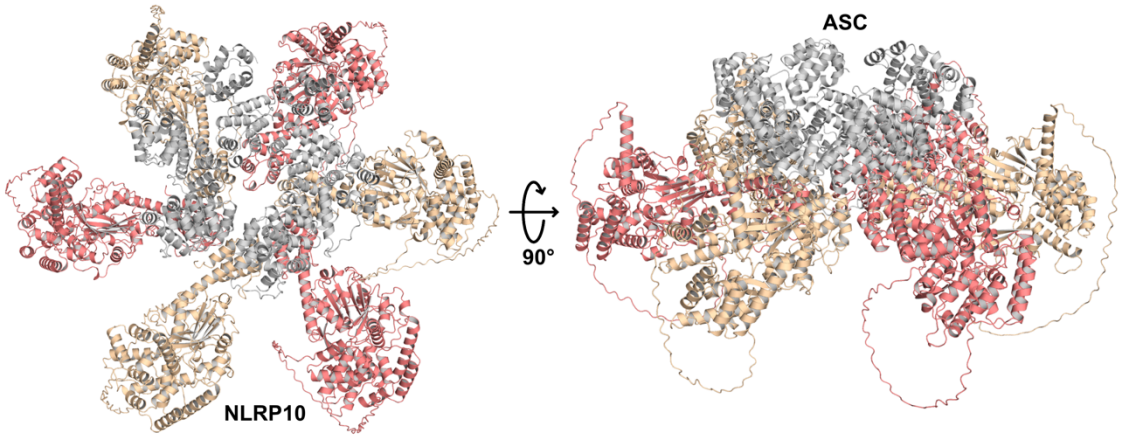

Figure 4-15: Model of NLRP10 hexamer.
AlphaFold3 model of a NLRP10 hexamer in complex with six units of ASC. The model shows a 6-fold symmetry with ASC interacting with NLRP10 PYDs in the center. NLRP10 is colored in yellow and red, ASC is colored in grey (Abramson et al., 2024).

4.5 Outlook

This thesis showed that NLRP10 forms an inflammasome complex that induces ASC oligomerization when treated with agents that damage mitochondria. However, the structure of NLRP10 remains elusive. The quality and homogeneity of the samples were insufficient for structure determination and require improvement. One promising approach would be to use small binding proteins or small molecules to improve protein stability. In chapter 2, the usage of nanobodies as crystallization tools for NLRP12 was not successful due to endogenously present protein. Thus, it is likely that camelids will not respond to NLRs in general, meaning that other approaches must be conducted.

Within the past two years, a new computational method got more attention, using de novo protein design to generate proteins with specified structural and/or functional properties (Ingraham et al., 2023; Watson et al., 2023; Yao & Wang, 2025). Artificial intelligence (AI)-based protein design offers the possibility to create specific binding proteins (AI-binder) to designated epitopes (Broske et al., 2025).

Initial design of AI-binder for NLRP10 (4-482) was performed together with Dr. Gregor Hagelüken to possibly support the crystallization process and the stabilization of either monomeric or dimeric species. A set of 500 AI-binder with high scores was computed, classified, and modelled. In **Figure 4-16**, six example structures are shown. The characterization of these AI-binders is an ongoing process.

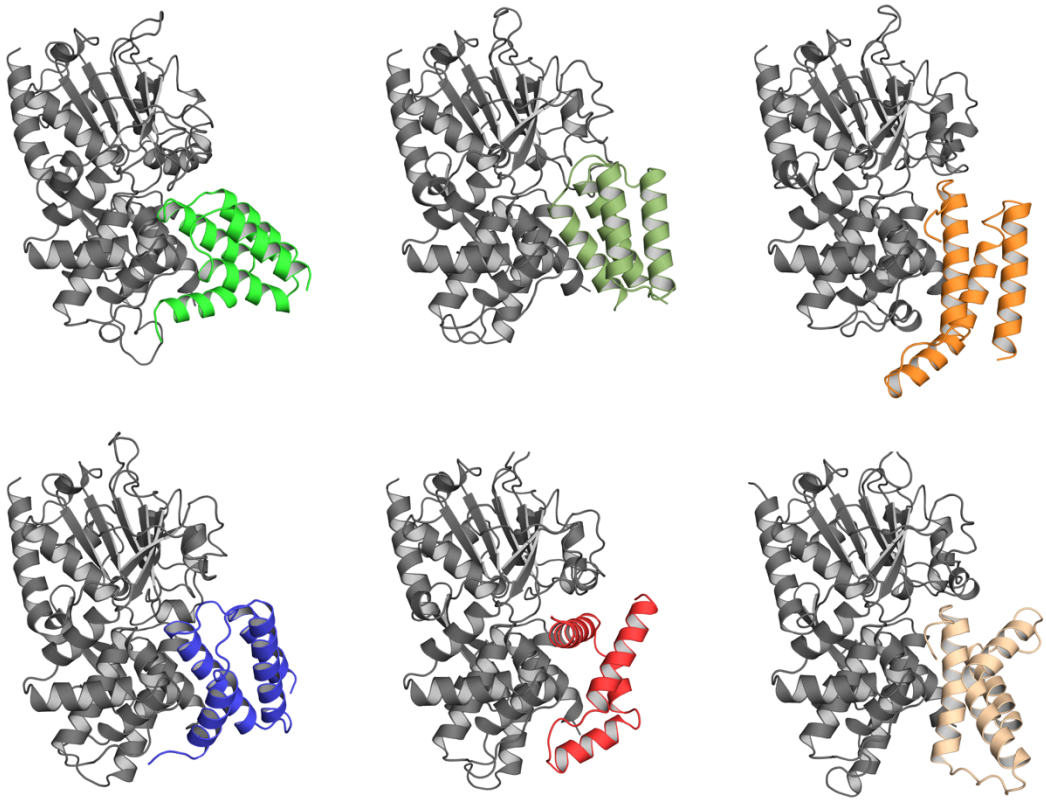

Figure 4-16: AI-binder design for NLRP10.
Display of six representative computed AI-binders specific for NLRP10. The construct used for calculation contains aa 96-482. NLRP10 is represented in grey, AI-binder are shown with different colors and consist of α-helical bundles.

Currently, there are no known small molecules that interact with NLRP10. Our collaboration partners investigated small molecules associated with NLRP10 and identified 3α-Aminocholestane as a potential binder. Initial structure prediction (chai discovery server) revealed a binding site next to the ATP binding pocket. This location is similar to the MCC950 binding site found in NLRP3 (Hochheiser, Pilsl, et al., 2022) and connects different subdomains in the central NACHT domain (**Figure 4-17a**). The surface representation revealed a tight pocket in which 3α-Aminocholestane was modeled (**Figure 4-17b**).

We are currently investigating the influence of the small molecule 3α-Aminocholestane during expression of NLRP10 in *Sf9* insect cells. Furthermore, the crystallization process could be improved, and binding studies could be conducted to get more insights into this possible binding mode.

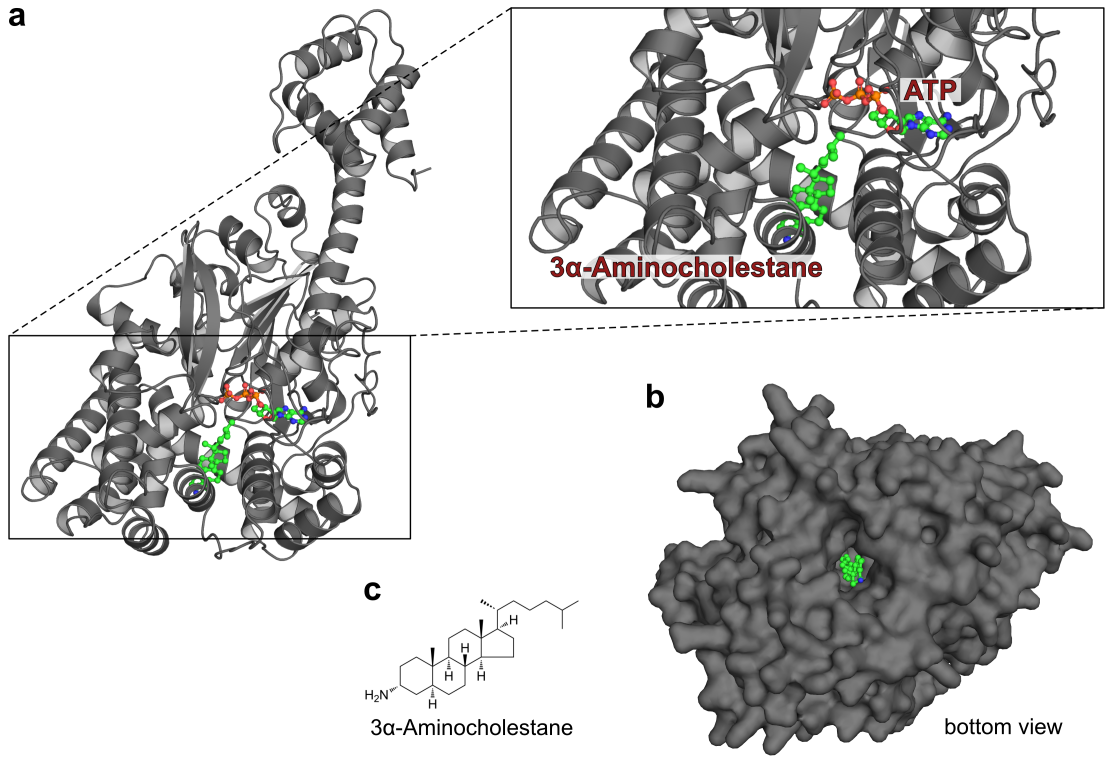

Figure 4-17: 3α-Aminocholestane as a potential small molecule binder.
*(**a**) Structure prediction of NLRP10 with ATP and 3α-Aminocholestane using the chai discovery server. (**b**) Surface representation with bottom view of NLRP10 showing a suitable binding pocket for 3α-Aminocholestane. (**c**) Structural formula of 3α-Aminocholestane.*

In the future, NLRP10 will be a valuable target for research on innate immunity to learn more about signaling pathways and structural elements. Elucidating biochemical processes is of great interest in improving pharmaceutical applications.

5. Methods

5.1 Molecular biology methods

5.1.1 Polymerase chain reaction

The polymerase chain reaction (PCR) is a biomolecular method to amplify protein coding sequences in vitro from DNA templates. Specific oligonucleotide primers containing different restriction sites were designed to allow ligation into the multiple cloning site (MCS) of a selected expression vector. The primer list is given in **Table 6-6**.

A thermocycler was used to perform the reactions following different cycles of denaturation, annealing and elongation shown in **Table 5-1**. Primer melting temperatures were calculated using the NEB TM Calculator tool (tmcalculator.neb.com). A standard PCR protocol is shown in **Table 5-2**.

Table 5-1: Standard PCR reaction mixture.

Components	Final concentration
DNA template	50-100 ng
dNTPs	200 µM
Primer $_{forward}$	2.5 µM
Primer $_{reverse}$	2.5 µM
Q5 reaction buffer (5x)	1x
Q5 high GC enhancer (5x)	1x
Q5 polymerase	0.02 U/µl
ddH_2O	up to 50 µl

Table 5-2: Standard PCR protocol.

Phase	Temperature (°C)	Time (s)	Cycles
Initial denaturation	98	180	1
Denaturation	98	10	5
Annealing	T_M-2	30	
Elongation	72	30/kb	
Denaturation	98	10	25
Annealing	$T_{M, +overhang}$-2	30	
Elongation	72	30/kb	
Final elongation	72	120	1

5.1.1.1 Site-directed mutagenesis

In comparison to the standard PCR reaction, another method was used to create single or multiple mutations in DNA templates of interest, called site-directed mutagenesis. In this work a modified version of the QuickChange™ mutagenesis introduced by (Liu & Naismith, 2008) was conducted. Therefore, a primer pair was designed, containing an overlapping (pp) and non-overlapping (no) region. The modified base pairs are located in the overlap. The respective reaction mixture and protocol are shown in **Table 5-3** and **Table 5-4**.

Table 5-3: Site-directed mutagenesis reaction mixture.

Components	Final concentration
DNA template	50-100 ng
dNTPs	200 µM
Primer $_{forward}$	2.5 µM
Primer $_{reverse}$	2.5 µM
Pfu polymerase buffer (10x)	1x
Pfu polymerase	0.02 U/µl
ddH_2O	up to 50 µl

Table 5-4: Site-directed mutagenesis protocol.

Phase	Temperature (°C)	Time (s)	Cycles
Initial denaturation	95	300	1
Denaturation	95	120	3
Annealing	$T_{M, pp}$-5	60	
Elongation	72	30/kb	
Denaturation	95	10	25
Annealing	$T_{M, no}$-5	60	
Elongation	72	30/kb	
Denaturation	95	120	2
Annealing	42	60	
Elongation	72	30/kb	
Final elongation	72	600	1

5.1.2 Restriction enzyme digestion

Restriction enzymes are bacterial or archaeal endonucleases that recognize specific, usually palindromic, double-stranded DNA sequences. The enzymatic cleavage reaction produces 5' and 3' sticky ends in preparation for subsequent ligation. Restriction enzymes were used to digest PCR reaction products, to linearize target vectors and to digest template DNA in site-directed mutagenesis. Further, they were used for test restriction digestion before Sanger sequencing.

The applied digestion setup is shown in **Table 5-5** and was performed at 37 °C for 1-2 h. Digested DNA was further analyzed by agarose gel electrophoresis or purified using the ExtractMe DNA Clean-Up Kit following the manufacturer's protocol.

Table 5-5: Standard restriction enzyme digestion protocol.

Components	Final concentration
DNA sample	variable
CutSmart buffer (10x)	1x
Restriction enzymes	1 U/µl
ddH_2O	up to 20 µl

5.1.3 Ligation of DNA

The digested DNA amplicon was ligated into selected linearized target vectors using T4 DNA ligase from bacteriophage T4. To catalyze phosphodiester bond formation of the two compatible sticky ends, approx. 50 ng of linearized vector was mixed with a 7 to 10-fold molar excess of insert. The reaction mixture was incubated at 16 °C overnight and afterwards the T4 ligase was heat inactivated 68 °C for 10 min. Half of the ligation product was transformed into chemically competent *E. coli* cells. The standard ligation protocol is shown in **Table 5-6**.

Table 5-6: Standard DNA ligation protocol.

Components	Final concentration
DNA vector	approx. 50 ng
DNA insert	7-10x molar excess
T4 ligation buffer (10x)	2 µl
T4 DNA ligase	1 µl (20 U/µl)
ddH_2O	up to 20 µl

5.1.4 Agarose gel electrophoresis

Agarose gel electrophoresis was used to separate DNA samples according to their size. Thus, samples (with 6x DNA gel loading dye) were loaded into an agarose gel (1 % agarose in 1xTAE buffer) mixed with UV-excitable DNA-binding dye peqGREEN. For each run a DNA reference ladder (100 bp or 1 kb) was added. The gel was placed in an electrophoresis chamber filled with 1xTAE buffer and was run for 40 min at 110 V. DNA samples were detected by UV excitation and imaged using a ChemiDocTM XRS+ imaging system. In case the DNA was needed for further applications, the ExtractMe DNA Clean-up & Gel-Out Kit was used to isolate the DNA according to the manufacturers protocol. The concentration was determined with a NanoDrop 2000 spectro-photometer at λ=260 nm.

5.1.5 Transformation into bacteria

Plasmid DNA was transformed into chemically competent *E. coli* NEBβ10 or DH5α cells for vector amplification or in chemically competent *E. coli* DH10 *Multi*Bac^{Turbo} cells to generate a bacmid shuttle vector for *Sf9* insect cell expression. For bacterial expression of recombinant protein, the expression vector was transformed into chemically competent *E. coli* BL21 (DE3) cells. All competent cells were prepared according to standard protocols using glycerol or $CaCl_2$ and were stored in aliquots at -80 °C.

Competent cells were thawed on ice and mixed with 50-100 ng of plasmid DNA. After 10 min incubation on ice, the mixture was incubated at 42 °C for 42 sec and afterwards immediately cooled on ice. 800 µl of LB medium was added and the bacteria were cultivated for 1-2 h at 37 °C and 800 rpm. After this incubation, which is needed to allow the cells the expression of the antibiotic resistance genes encoded on the transformed plasmid, the cell suspension was centrifuged at 5,000 r.c.f. for 5 min. Excess media was discarded, the cell pellet was resuspended in the remaining media and the suspension was streaked out on an LB agar plate supplemented with the appropriate antibiotics. The plates were incubated at 37 °C overnight.

5.1.6 Preparation of plasmid DNA and sequencing

To amplify plasmid DNA, 50-100 ng DNA were transformed into *E. coli* DH5α as described in chapter **5.1.5**. Single colonies were transferred from the agar plate to 3 ml LB media supplemented with respective antibiotics. After overnight incubation at 37 °C, 150 rpm, the plasmid DNA was extracted and subsequently purified using ExtractMe Plasmid mini kit (Blirt) or the Plasmid DNA purification kit (Machery-Nagel) according to the manufacturers protocol. The resulting plasmid DNA concentration was determined using a NanoDrop 2000 spectrophotometer at 260 nm absorbance. The purity of the DNA was determined by measuring the 260/280 nm and 260/230 nm ratios.

To confirm the plasmid DNA sequences, Sanger sequencing was conducted performed by GATC Biotech AG, Ebersberg, Germany or MicroSynth AG, Göttingen, Germany. The sequencing results were analyzed using SnapGene software.

5.1.7 Production of the bacmid shuttle vector

The DH10 MultiBac^{Turbo} strain was transformed in the *Multi*Bac^{Turbo} bacmid, which carries a modified baculoviral genome. This bacmid includes a Tn7 attachment site embedded within a *lacZα* reporter gene. All *Sf9* expression plasmids were derived from the pACEBac1 transfer vector, which contains Tn7 transposition elements. Once an expression vector was introduced, the Tn7 elements, along with the target protein-coding sequence, were inserted into the baculoviral genome, thereby disrupting the *lacZα* reporter gene. This disruption enables detection via blue/white screening using the chromogenic substrate X-Gal (5-bromo-4-chloro-3-indolyl β-D-galactopyranoside).

For screening, transformed bacteria were plated on LB agar supplemented with ampicillin, kanamycin, gentamycin, and tetracycline (all 1:1000). Additionally, X-Gal (100 µg/ml) and IPTG (isopropyl-β-D-thiogalactopyranoside, 40 µg/ml) were added before incubation at 37 °C for at least 48 hours to achieve blue/white colony differentiation. Single white colonies, carrying the gene of interest, were picked and inoculated in 3 ml LB medium with respective antibiotics. After overnight incubation, cells were harvested by centrifugation at 4,000 r.c.f. for 5 min and the bacmid shuttle vector was isolated using the ExtractMe Plasmid Mini Kit. The DNA was precipitated by addition of 800 µl ice-cold isopropanol and collected by centrifugation at 20,000 r.c.f. and 4°C for 30 min. The isopropanol was removed and the DNA pellet was carefully washed with 500 µl ice-cold 70 % ethanol. Another centrifugation at 20,000 r.c.f. and 4°C for 10 min was conducted to achieve the DNA pellet. The following steps were carried out in a sterile tissue culture hood (chapter **5.2.1**).

5.2 Recombinant protein expression

5.2.1 Recombinant protein expression in *Sf9* insect cells

5.2.1.1 Preparation of recombinant baculovirus

Bacmid shuttle vectors (chapter **5.1.7**) were transfected into *Sf9* insect cells to generate infectious baculovirus particles for subsequent protein expression.

Sf9 insect cells were cultivated as a suspension culture in SF900^{TM} SFM III medium at 27 °C and 100 rpm. They were divided to 0.5x10^5 cells/ml every 3 or 4 days after determining the cell density using 0.4 % trypan blue in an EVE^{TM} automatic cell counter.

To start virus production, 0.3x10^5 cells/ml were used to prepare a 6-well plate with 2 ml per well and allowed adherent growth. 5 µl TransIT^{TM}-Insect transfection reagent

was added to 100 µl media and then mixed with the prepared bacmid vector (chapter **5.1.7**) dissolved in 100 µl media. After 10 min incubation time, the 200 µl mix was added to the previously prepared wells and incubated at 27 °C for 72 h. This results in the virus stock 0 (**V_0**).

4 – 10 % filtered supernatant of V_0 was used to infect 20 – 50 ml suspension culture of *Sf9* insect cells with $0.5x10^5$ cells/ml and incubated at 27 °C, 100 rpm for 72 h. Infected cells could be monitored by cell count and cell size. Upon infection, cell division should be stopped and cells should grow in size. Cells were harvested by centrifugation at 500 r.c.f. for 5 min to collect the supernatant by filtration (0.2 µm) and stored as virus stock 1 (**V_1**) at 4 °C. Final propagation into virus stock 2 (**V_2**) was done by infection of 50 ml suspension culture of *Sf9* insect cells with $1.0x10^6$ cells/ml using 3 % (v/v) of V_1. After 72 h incubation at 27 °C and 100 rpm, cells were again harvested by centrifugation at 500 r.c.f. for 5 min to collect the supernatant by filtration (0.2 µm) and stored as V_2 at 4 °C.

5.2.1.2 Expression culture of *Sf9* insect cells

Recombinant protein expression was performed in *Sf9* insect cells with $1.5x10^6$ cells/ml. 3 % (v/v) of V_2 was used to infect a suspension culture of usually 250 ml, 500 ml or 1 l. Cells were monitored pre- and post-infection regarding cell count, diameter and viability. Expressions were set up for 48 or 72 h at 27 °C and 100 rpm. Afterwards, cells were collected by centrifugation at 1000 r.c.f., 4 °C for 20 min and subsequently the pellet was washed with cold PBS and transferred into a falcon tube. After another centrifugation step, the pellet was snap-frozen in liquid nitrogen and stored at -80 °C for subsequent purification.

5.2.2 Recombinant protein expression in *E. coli*

The desired expression plasmid was transformed into *E. coli* BL21 (DE3) or WK6 cells according to chapter **5.1.5**. Single colonies were picked from LB agar plates to inoculated 50-100 ml LB medium, containing respective antibiotics, to grow a starter culture at 37°C and 150 rpm shaking overnight. Part of this starter culture was stored at - 80 °C with 50 % glycerol as a glycerol-stock for later expressions. The starter culture was used to inoculate an expression culture (1-6 l) to obtain an optical density $(OD)_{600}$ value of 0.1 to 0.2. The expression culture was grown at 37 °C and 150 rpm shaking until OD_{600} reached ~ 0.8. Afterwards the expression culture was supplemented with 0.5 M IPTG to induce expression and kept at 16 °C and 150 rpm shaking overnight. Cells were harvested by centrifugation at 4,000 r.c.f. for 20 min. The pellet was collected and stored at -80 °C for later purification.

5.3 Recombinant protein purification

5.3.1 Cell lysis

Previously expressed and frozen cells were resuspended in lysis buffer (5x volume to weight) and gently thawed on ice. The suspension was supplemented with 1 mM PMSF and 1 µg/ml DNaseI to protect from endogenous proteases and endogenous DNA. After the pellet was resolved, cells (*Sf9* or *E.coli*) were lysed by sonication on ice (*Sf9*: 5 s on-time, 10 s off-time, 5 min at 40 % int.; *E.coli*: 5 s on-time, 5 s off-time, 5 min at 40 %

int.). Centrifugation at 10 °C, 70,000 r.c.f. for 30-60 min was applied to clear cell lysates followed by filtration with a syringe filter (0.45 µm or 0.8 µm pore size) to prepare for subsequent affinity chromatography.

5.3.2 Affinity chromatography

Initial protein purification was performed using affinity chromatography (AC), taking advantage of different specific affinity tags that bind to respective immobilized ligands on a stationary phase. All expression constructs in this work were provided with N-terminal affinity tags, 6x-His (6x-histidine), GST (glutathione-S-transferase) or MBP (maltose-binding protein) tag. Either HisTrap, GSTrap or MBPTrap columns were used with a fast protein liquid chromatography (FPLC) system (Äkta Prime Plus or Äkta Start) or gravity-flow columns with respective bead material. The flow through was collected, followed by a wash step, and finally the target protein was eluted with a matching elution buffer. The whole purification process was carried out on ice or in cooling cabinets at 4 °C. Protein concentrations were determined using a NanoDrop spectrophotometer at 280 nm wavelength. Specific protein parameters were calculated with an online tool (https://web.expasy.org/protparam). The purity was estimated via the 260/280 nm ratio.

5.3.3 Affinity tag cleavage

To remove the affinity tag from the expressed proteins, a sequence coding for a Tobacco Etch Virus (TEV) protease cleavage site (amino acid sequence: ENLYFQGS) was cloned between the expression construct and the tag. Thus, after affinity chromatography, TEV protease (in-house preparation) was added typically in a 1/50 ratio at 4 °C overnight. Samples were further purified using size-exclusion chromatography.

5.3.4 Size-exclusion chromatography

Size-exclusion chromatography (SEC) was performed to finally purify target proteins from other particles or proteins like affinity tags or TEV protease. Also, different species like monomer, dimer and oligomer could be separated due their size. Particle travel with individual speed through the porous gel matrix depending on their hydrodynamic radius. Therefore, smaller particles can enter more pores and need more time to pass the column than bigger particles. Numerous different size-exclusion chromatography columns were used during this work (**Table 6-10**). For selected purifications, a tandem affinity chromatography column was attached to the SEC column to remove the previously cleaved affinity tag. All columns were used with a fast protein liquid chromatography (FPLC) system (Äkta Prime Plus or Äkta Pure) in a cooling cabinet at 4 °C. Bevor sample injection, the columns were equilibrated with 1.2 column volume (CV) SEC buffer. Fractions were collected by an automated fraction collector and analyzed by SDS-PAGE analysis. Finally selected fractions were pooled, concentrated and snap-frozen in liquid nitrogen for further usage.

5.3.5 Protein purification protocols

5.3.5.1 Human NOD2 wt (1-1040)

Protein construct	MW (kDa)	pI	Abs. 1 %
MBP-NOD2 wt (1-1040)	156.7	5.96	12.07
NOD2 wt (1-1040)	115.4	6.30	10.51

Lysis buffer		SEC buffer	
Tris pH 8.0	25 mM	Tris pH 8.0	25 mM
NaCl	500 mM	NaCl	500 mM
Glycerol	10 %	Glycerol	10 %
DTT	1 mM	DTT	1 mM

Elution buffer: Lysis buffer supplemented with 10 mM maltose.

NOD2 (1-1040) was expressed as an N-terminally tagged MBP-fusion protein in *Sf9* insect cells. The cell pellet was resuspended in lysis buffer with PMSF and DNaseI and subsequently lysed by sonication. The lysate was cleared by centrifugation at 70,000 r.c.f., 10 °C for 45 min and filtration, before using an MBPTrap affinity chromatography (1 ml/min). Thereafter, the column was washed with lysis buffer until baseline level and target protein was eluted in 1 ml fractions using elution buffer. Protein containing fractions were pooled, concentrated and injected onto a pre-equilibrated Superose 6 Increase 10/300 column. Protein quality was analyzed by SDS-PAGE analysis and void peak fraction was pooled, concentrated and snap-frozen in liquid nitrogen.

5.3.5.2 Human NOD2ΔCARDs (215-1040)

Protein construct	MW (kDa)	pI	Abs. 1 %
MBP-NOD2ΔCARDs (215-1040)	132.8	6.22	11.12
NOD2ΔCARDs (215-1040)	91.4	7.15	8.74

Lysis buffer		SEC buffer	
Tris pH 8.0	25 mM	Tris pH 8.0	25 mM
NaCl	500 mM	NaCl	500 mM
Glycerol	10 %	Glycerol	10 %
DTT	1 mM	DTT	1 mM

Elution buffer: Lysis buffer supplemented with 10 mM maltose.

NOD2 (1-1040) was expressed as an N-terminally tagged MBP-fusion protein in *Sf9* insect cells. The cell pellet was resuspended in lysis buffer with PMSF and DNaseI and subsequently lysed by sonication. The lysate was cleared by centrifugation at 70,000 r.c.f., 10 °C for 45 min and filtration, before using an MBPTrap affinity chromatography (1 ml/min). Thereafter the column was washed with lysis buffer until baseline level and target protein was eluted in 1 ml fractions using elution buffer. Protein containing fractions were pooled and TEV digestated at 4 °C overnight. The sample was injected onto a pre-equilibrated Superdex 200 Increase 10/300 GL column. Protein quality was analyzed by SDS-PAGE analysis and protein containing fractions were pooled, concentrated and snap-frozen in liquid nitrogen.

5.3.5.3 Human NLRP12 wt (1-1061)

Protein construct	MW (kDa)	pI	Abs. 1 %
MBP-NLRP12 wt (1-1061)	161.6	6.08	12.04
NLRP12 wt (1-1061)	120.2	6.59	10.55

Lysis buffer		SEC buffer	
Hepes pH 7.5	100 mM	Hepes pH 7.5	25 mM
NaCl	50 mM	NaCl	50 mM
Glycerol	20 %	Glycerol	20 %
		Maltose	2 mM

Elution buffer: Lysis buffer supplemented with 10 mM maltose.

NLRP12 (1-1061) was expressed as an N-terminally tagged MBP-fusion protein in *Sf9* insect cells. The cell pellet was resuspended in lysis buffer with PMSF and DNaseI and subsequently lysed by sonication. The lysate was cleared by centrifugation at 70,000 r.c.f., 10 °C for 45 min and filtration, before using an MBPTrap affinity chromatography (1 ml/min). Thereafter the column was washed with lysis buffer until baseline level and target protein was eluted in 1 ml fractions using elution buffer. Protein containing fractions were pooled, concentrated and injected onto a pre-equilibrated Superose 6 Increase 10/300 column. Protein quality was analyzed by SDS-PAGE analysis and void peak fraction was pooled, concentrated and snap-frozen in liquid nitrogen.

5.3.5.4 Human NLRP12^{NACHT} (122-679), (122-663), (122-667) and (122-676)

Protein construct	MW (kDa)	pI	Abs. 1 %
MBP-NLRP12 (122-679)	106.1	5.57	13.20
NLRP12 (122-679)	64.8	5.99	11.16
MBP-NLRP12 (122-663)	104.4	5.58	13.14
NLRP12 (122-663)	63.0	6.02	11.00
MBP-NLRP12 (122-667)	104.8	5.61	13.22
NLRP12 (122-667)	63.5	6.06	11.15
MBP-NLRP12 (122-676)	105.7	5.49	13.25
NLRP12 (122-676)	64.4	5.84	11.23

Lysis buffer		SEC buffer	
Tris pH 7.8	20 mM	Hepes pH 7.8	25 mM
NaCl	150 mM	NaCl	150 mM
$MgCl_2$	10 mM	$MgCl_2$	10 mM
ADP	1 mM	ADP	1 mM
β-ME	5 mM	TCEP	1 mM
		Arginine	150 mM

Elution buffer: SEC buffer supplemented with 10 mM maltose.

NLRP12^{NACHT} was expressed as an N-terminally tagged MBP-fusion protein in *Sf9* insect cells. The cell pellet was resuspended in lysis buffer with PMSF and DNaseI and subsequently lysed by sonication. The lysate was cleared by centrifugation at 70,000 r.c.f., 10 °C for 45 min and filtration, before using an MBPTrap affinity chromatography (1 ml/min). Thereafter the column was washed with lysis buffer down to the baseline

level and the target protein was eluted in 1 ml fractions using elution buffer. Protein containing fractions were pooled and TEV digestated at 4 °C overnight. The sample was injected onto a pre-equilibrated HiLoad 16/600 Superdex 75 PG column. Protein quality was analyzed by SDS-PAGE analysis and protein containing fractions were pooled, concentrated and snap-frozen in liquid nitrogen.

5.3.5.5 Human NLRP12^{NACHT} (122-679) mutants

Protein construct	MW (kDa)	pI	Abs. 1 %
MBP-NLRP12 (122-679) mutant	106.1	5.57	13.20
NLRP12 (122-679) mutant	64.8	5.99	11.16

Lysis buffer		SEC buffer	
Tris pH 7.8	20 mM	Hepes pH 7.8	25 mM
NaCl	150 mM	NaCl	150 mM
$MgCl_2$	10 mM	$MgCl_2$	10 mM
ADP	1 mM	ADP	1 mM
β-ME	5 mM	TCEP	1 mM
		Arginine	150 mM

Elution buffer: SEC buffer supplemented with 10 mM maltose.

NLRP12^{NACHT} mutants were expressed as an N-terminally tagged MBP-fusion protein in *Sf9* insect cells. The cell pellet was resuspended in lysis buffer with PMSF and DNaseI and subsequently lysed by sonication. The lysate was cleared by centrifugation at 70,000 r.c.f., 10 °C for 45 min and filtration, before using an MBPTrap affinity chromatography (1 ml/min). Thereafter the column was washed with lysis buffer until baseline level and target protein was eluted in 1 ml fractions using elution buffer. Protein containing fractions were pooled and TEV digestated at 4 °C overnight. The sample was injected onto a pre-equilibrated HiLoad 16/600 Superdex 75 PG column. Protein quality was analyzed by SDS-PAGE analysis and protein containing fractions were pooled, concentrated and snap-frozen in liquid nitrogen.

5.3.5.6 Nanobody NbN12

Protein construct	MW (kDa)	pI	Abs. 1 %
His-NbN12	16.4	7.82	21.56

Lysis + SEC buffer		wash buffer	
Tris pH 8.0	50 mM	Hepes pH 7.8	25 mM
NaCl	50 mM	NaCl	150 mM
		Imidazole	20 mM

Elution buffer: SEC buffer supplemented with 500 mM imidazole.

NbN12 was expressed as a C-terminally tagged His-fusion protein in *E. coli* WK6 cells. The cell pellet was resuspended in lysis buffer and subsequently lysed by sonication. The lysate was cleared by centrifugation at 70,000 r.c.f., 10 °C for 45 min and filtration. Pre-equilibrated Ni-NTA resin (5 ml) was added to the lysate and incubated overnight at 4 °C on a roll incubator. A gravity flow column was used to collect the flow through and

wash the resin with 20-fold excess of wash buffer. Threefold excess of elution buffer was used to elute the nanobody. The sample was concentrated to 5 ml and injected onto a pre-equilibrated HiLoad 16/600 Superdex 75 PG column. Protein quality was analyzed by SDS-PAGE analysis and protein containing fractions were pooled, concentrated and snap-frozen in liquid nitrogen.

5.3.5.7 Human NLRP10 wt (4-655) and Walker mutants

Protein construct	MW (kDa)	pI	Abs. 1 %
MBP-NLRP10 wt (4-655)	116.2	5.99	11.33
NLRP10 wt (4-655)	74.8	6.85	8.53
MBP-NLRP10 C-tail mutant (4-655)	116.1	5.44	11.34
NLRP10 C-tail mutant (4-655)	74.8	5.70	8.53

Lysis buffer		SEC buffer	
Tris pH 7.5	25 mM	Tris pH 7.5	25 mM
NaCl	300 mM	NaCl	300 mM
β-ME	5 mM	β-ME	5 mM
Glycerol	5 %	Glycerol	5 %

Elution buffer: Lysis buffer supplemented with 10 mM maltose.

NLRP10 (4-655) was expressed as an N-terminally tagged MBP-fusion protein in *Sf9* insect cells. The cell pellet was resuspended in lysis buffer with PMSF and DNaseI and subsequently lysed by sonication. The lysate was cleared by centrifugation at 70,000 r.c.f., 10 °C for 45 min and filtration, before using equilibrated amylose affinity resin (1 h, 4 °C). A gravity flow column was used to collect the flow through and wash the resin with 20-fold excess of buffer. Threefold excess of elution buffer was used to elute the NLRP10 protein. Protein containing fractions were pooled, concentrated and injected onto a pre-equilibrated Superose 6 Increase 10/300 column. Protein quality was analyzed by SDS-PAGE analysis and void peak fraction as well as oligomeric fraction were pooled, concentrated and snap-frozen in liquid nitrogen.

5.3.5.8 Human NLRP10 (4-482) and (4-583)

Protein construct	MW (kDa)	pI	Abs. 1 %
MBP-NLRP10 (4-482)	96.3	5.53	12.79
NLRP10 (4-482)	54.9	6.03	10.07
MBP-NLRP10 (4-583)	108.3	5.64	12.02
NLRP10 (4-583)	66.9	6.14	9.31

Lysis buffer		SEC buffer	
Tris pH 7.8	20 mM	Hepes pH 7.8	20 mM
NaCl	150 mM	NaCl	150 mM
β-ME	5 mM	TCEP	1 mM
ADP	0.5 mM	ADP	0.5 mM
$MgCl_2$	10 mM	$MgCl_2$	10 mM
		Arginine	150 mM

Elution buffer: Lysis buffer supplemented with 10 mM maltose.

NLRP10 (4-482) and 4-583) were expressed as N-terminally tagged MBP-fusion proteins in *Sf9* insect cells. The cell pellet was resuspended in lysis buffer with PMSF and DNaseI and subsequently lysed by sonication. The lysate was cleared by centrifugation at 70,000 r.c.f., 10 °C for 45 min and filtration, before using an MBPTrap affinity chromatography (1 ml/min). Thereafter the column was washed with lysis buffer until baseline level was reached and target protein was eluted in 1 ml fractions using elution buffer. Protein containing fractions were pooled and TEV digestated at 4 °C overnight. The sample was injected onto a pre-equilibrated Superdex 200 Increase 10/300 GL column. Protein quality was analyzed by SDS-PAGE analysis and protein containing fractions were pooled, concentrated and snap-frozen in liquid nitrogen.

5.3.5.9 Human NLRP10 wt (4-655) co-expressions

Protein construct	MW (kDa)	pI	Abs. 1 %
GST-TELO2	118.7	5.63	8.83
TELO2	91.7	5.54	6.58
GST-TTI1	148.9	5.68	8.80
TTI1	122.0	5.63	7.11
GST-FAF2	79.5	5.59	10.97
FAF2	52.6	5.45	8.14

Lysis buffer		**SEC buffer**	
Tris pH 7.5	25 mM	Tris pH 7.5	25 mM
NaCl	300 mM	NaCl	300 mM
β-ME	5 mM	β-ME	5 mM
Glycerol	5 %	Glycerol	5 %

Elution buffer: Lysis buffer supplemented with 10 mM maltose.

NLRP10 (4-655) was co-expressed as an N-terminally tagged MBP-fusion protein together with potential binding partners in *Sf9* insect cells. The cell pellet was resuspended in lysis buffer with PMSF and DNaseI and subsequently lysed by sonication. The lysate was cleared by centrifugation at 70,000 r.c.f., 10 °C for 45 min and filtration, before using equilibrated amylose affinity resin (1 h, 4 °C). A gravity flow column was used to collect the flow through and wash the resin with 20-fold excess of buffer. Threefold excess of elution buffer was used to elute the NLRP10-binding partner complex. Protein containing fractions were pooled, concentrated and injected onto a pre-equilibrated Superose 6 Increase 10/300 column. Protein quality was analyzed by SDS-PAGE analysis and void peak fraction as well as oligomeric fraction were pooled, concentrated and snap-frozen in liquid nitrogen.

5.3.5.10 NLR PYDs

Protein construct	MW (kDa)	pI	Abs. 1 %
GST-NLR PYDs	39	5.80	14.05
NLR PYDs	12	5.70	8.60

Lysis buffer		**SEC buffer**	
Tris pH 7.8	50 mM	Tris pH 7.8	50 mM
NaCl	150 mM	NaCl	150 mM
β-ME	5 mM	β-ME	5 mM

Elution buffer: SEC buffer supplemented with 10 mM glutathione.

NLR PYDs were expressed as N-terminally tagged His-fusion proteins in *E. coli* BL21 cells. The cell pellets were resuspended in lysis buffer and subsequently lysed by sonication. The lysate was cleared by centrifugation at 70,000 r.c.f., 10 °C for 45 min and filtration. Pre-equilibrated glutathione agarose resin (5 ml) was added to the lysate and incubated overnight at 4 °C on a roll incubator. A gravity flow column was used to collect the flow through and wash the resin with 20-fold excess of wash buffer. Threefold excess of elution buffer was used to elute the PYDs. The sample was concentrated to 5 ml and injected onto a pre-equilibrated HiLoad 16/600 Superdex 75 PG column. Protein quality was analyzed by SDS-PAGE analysis and protein containing fractions were pooled, concentrated and snap-frozen in liquid nitrogen.

5.4 Analytical methods

5.4.1 SDS-PAGE analysis

To investigate protein quality, purity and integrity, sodium dodecyl sulfate (SDS) polyacrylamide gel electrophoresis (PAGE) was used, to separate proteins by their size. SDS sample buffer containing reducing agent to remove cysteine bridges, was used to denature samples by incubation at 92 °C for 5 min. The negatively charged detergent SDS binds to the proteins, resulting in denaturation and masking the intrinsic charge. After that, the samples were loaded to self-made discontinuous polyacrylamide gels as described in **Table 5-7**. A Mini-Protean Tetra Cell (Bio-Rad) electrophoresis system was used to perform SDS-PAGE analysis. The chamber was filled with SDS running buffer and gels were run at a constant voltage of 250 V for 35 min. To stain gels, Coomassie staining solution was conducted upon 1 min boiling. 10 min incubation with gentle mixing was followed by boiling for 5 min in destaining solution and incubation for 1 h at room temperature with gentle mixing. Stained gels were imaged using a ChemiDoc™ XRS+ (Bio-Rad) imaging system. For subsequent Western Blot analysis, no staining steps were applied.

Table 5-7: Recipe for polyacrylamide gel preparation (1 gel).

Gel type	Ingredient	Volume
5 % stacking gel	Acrylamide (30 %)	225 µl
	Stacking gel buffer	175 µl
	TEMED	1.3 µl
	APS (10 %)	13.25 µl
	H_2O	900 µl
12 % separation gel	Acrylamide (30 %)	2.1 ml
	Separation gel buffer	1.46 ml
	TEMED	1.76 µl
	APS (10 %)	58.88 µl
	H_2O	1.69 ml
15 % separation gel	Acrylamide (30 %)	2.63 ml
	Separation gel buffer	1.46 ml
	TEMED	1.76 µl
	APS (10 %)	58.88 µl
	H_2O	1.16 ml

5.4.2 Western Blot analysis

Western Blot analysis was conducted to specifically detect certain proteins. Different primary antibodies were used either detecting protein tags or specific target proteins. All secondary antibodies were horseradish peroxidase (HRP) conjugated derived from different organisms. Previously prepared SDS-PAGE samples (chapter **5.4.1**) were transferred to a nitrocellulose membrane in a semi-dry blotting chamber supported by blotting filters. All parts were pre-equilibrated in transfer buffer and arranged as followed: 3x filter, membrane, SDS gel, 3x filter. The blotting process was done at a constant current of 0.16 A per blot for 45 min. Thereafter, the blotting membrane was blocked with PBS-T with 5 % (w/V) milk powder for 1 h at room temperature and gentle agitation, followed by 3x 5 min washing with PBS-T. Primary antibodies were added according to

the manufacturers protocol and incubated at 4 °C and gentle agitation overnight. Again 3x 5 min washing with PBS-T was conducted before incubating with the second antibody according to the manufacturers protocol for 1 h at room temperature and gentle agitation. Subsequently, the membrane was washed 3x 5 min with PBS before treatment with Western Blotting detection reagent (Invitrogen). Analysis and documentation were done with a ChemiDoc™ XRS+ (Bio-Rad) imaging system.

5.4.3 Mass spectrometry

Peptide mass fingerprint was performed to identify unknown protein samples or investigate post-translational modifications (PTMs). Therefore, samples from SDS-PAGE analysis (chapter **5.4.1**) were cut out and sent to the group of Prof. Dr. Henning Urlaub at the Max Planck Institute for Multidisciplinary Sciences in Göttingen. They purified the samples from the gel and proteolytically digested the samples into peptides. These were further analyzed in a mass spectrometer. Results were evaluated using databases to identify proteins and PTMs. The evaluation in our lab was done with Scaffold 5 software.

5.4.4 Nano differential scanning fluorimetry

Nano differential scanning fluorimetry (nanoDSF) is an analytical method to determine protein stability. Thermal unfolding events of proteins can be monitored during a linear temperature ramp by measuring intrinsic fluorescence at 350 and 330 nm wavelength. Due to changes in the environment of tryptophane and tyrosine residues, they become surface exposed and change the fluorescence signal. The melting curve results in a determined melting temperature T_M, indicating half-unfolded protein. This method can be also used to test protein-protein interactions or small molecule binding. All measurements were performed using a Prometheus NT.48 thermal nanoDSF device with the corresponding software (NanoTemper Technologies). At least 3 µM protein in 10 µl sample volume was prepared for a single measurement, but generally duplicates were collected. For interaction studies 30 min incubation time was implicated. A temperature ramp from 20 to 90 °C was applied with a heating rate of 1.5 °C/min. The melting temperature was automatically calculated as the inflection point of the first derivative of the 350/330 nm ratio by the associated software.

5.4.5 Dynamic light scattering

Dynamic light scattering (DLS) is an analytical method to determine particle diameters in solution. Protein particles scatter the incoming laser beam due to their hydrodynamic radii. Measurements can be performed at a certain timepoint or in a time-dependent manner.

Protein samples were centrifuged at 14,000 r.c.f. prior to measurement. The DynaPro NanoStar DLS device (Wyatt Technology) was used with single use cuvettes. Sample concentration should be more than 1 mg/ml in 10 µl volume. Three measurements were done at a sample temperature of T=25 °C and three measurement cycles of each 20 single data acquisitions with acquisition times of t=3 s. For time dependent measurements, additional collections were set up in defined time periods. Setup and evaluation were done with the Dynamics® software (Wyatt Technology).

5.4.6 SEC-MALS analysis

This analytical method combines size exclusion chromatography (SEC) with multi-angle light scattering (MALS) and was used to determine the molar mass of protein samples at defined elution volumes. Therefore, the scattered light at defined angles is measured which is directly proportional to the product of molar mass and concentration. Concentration is either determined by the refractive index (RI) or UV absorption.

The used setup was built up by a 1260 Bioinert Infinity LC system together with a miniDawn 3141MD3 and an Optilab rEX 650 device for online MALS (661 nm) and RI (658 nm) detection. Prior to 20-50 µl injection, samples were centrifugated at 10,000 r.c.f for 10 min. Either Superose 6 or Superdex 200 columns (10/300 or 5/150) were used. Evaluation was performed using Astra 8 software.

5.4.7 Isothermal titration calorimetry

Isothermal titration calorimetry (ITC) is a biophysical method to determine binding constants of any two or more molecules that release or absorb heat upon binding. A calorimetric measurement is performed to measure biomolecular interactions. This includes enthalpy (ΔH), entropy (ΔS), stoichiometry (n) and affinity (K_A). This allows the calculation of K_D by employing basic thermodynamics.

ITC measurements were performed with a MicroCal PEAQ ITC and corresponding control- and evaluation software. Therefore, the cell was loaded with 300 µl and the syringe reservoir with 70 µl of the reactants. It was aimed to achieve a molar ratio of syringe to cell of 1:10. The measurements were carried out with a total of 19 injections and a constant temperature of 25 °C. The first injection started with 0.4 µl, whereas the subsequent 18 injections contained 2 µl. The measurements were performed with aimed concentrations of 50 µM (cell) vs. 500 µM (syringe).

5.4.8 HPLC based ATP hydrolysis assay

An in vitro ATPase high-performance liquid chromatography (HPLC) assay was used to determine ATP hydrolysis rates. This method measures the amount of hydrolyzed nucleotide by an ATPase-active protein via absorption at 254 nm using an HPLC system. This process was carried out for 1 hour, with samples taken every 10 minutes to enable time-dependent analysis of ATP hydrolysis. Since nucleotides are polar molecules in a soluble, mobile phase, a reverse-phase HPLC with a nonpolar C18-silica column was used. The different nucleotide species (ATP, ADP, and AMP) were separated based on their retention time. Tetrabutylammonium bromide (TBA-Br) was used to create an ion-pair interaction between the positively charged ammonium and negatively charged polar phosphate groups, forming a complex. Due to the number of phosphate groups, a greater or lesser amount of TBA-Br is complexed, thereby raising or lowering the polarity. The buffer in this assay (**Table 5-8**) contains a small amount of acetonitrile to wash the nucleotides through the column.

Table 5-8: Composition of ATPase HPLC assay buffer.

HPLC assay buffer pH 7.5	
K_2HPO_4	30 mM
KH_2PO_4	70 mM
TBA-Br	10 mM
NaN_3	0.2 mM
Acetonitrile	4 %

Table 5-9 depicts the sample preparation. The reaction vial was immediately transferred to the HPLC auto sampler, and the first sample was collected. The following six samples were measured automatically at 10-minute intervals. The results were obtained using the analysis software.

Table 5-9: Sample preparation for ATPase HPLC assay.

Component	Final concentration
Protein	3 µM
$MgCl_2$	5 mM
ATP	100 µM
Protein buffer	Up to 90 µl volume

5.4.9 SPR spectroscopy

Surface plasmon resonance (SPR) spectroscopy is a label-free optical technique widely used to quantify biomolecular interactions in real time. It measures changes in the refractive index near a sensor surface when an analyte binds to an immobilized ligand. This enables the determination of kinetic parameters and equilibrium affinities without the need for chemical labeling. SPR is particularly well-suited for studying protein-protein, protein-small molecule, and protein-nucleic acid interactions under near-physiological conditions, making it a valuable tool in basic research and drug discovery.

SPR experiments were performed on a Biacore™ 8K instrument (Cytiva) equipped with a streptavidin-functionalized sensor chip (Series S sensor chip SA). The chip contains 8 channels, each with a measuring and reference flow cell. Measurements were performed at 25 °C with a running buffer containing: 10 mM HEPES pH 7.4, 200 mM NaCl, 0.5 mM ADP, 0.5 mM TCEP (tris[2-carboxyethyl]phosphine) or dithiothreitol (DTT), 2 mM MgCl2, 1 g/L carboxymethyl dextran (CMD) 0.05 % Tween20, 2 % DMSO. The chip was conditioned with three consecutive injections of 1 M NaCl in 50 mM NaOH at a flow rate of 10 µl/min for 1 min and the protein sample was immobilized on the measuring flow cell at 1-2 µl/min for 900-3600 s. The flow system was washed using 50 % isopropanol in 1 M NaCl and 50 mM NaOH. Free streptavidin binding sites on both flow cells were saturated by four consecutive injections of Biotin-PEG (1 µM, Mn = 2,300 Da) at 10 µl/min for 2 min. Single-cycle kinetic measurements were performed with increasing concentrations of the analytes (flow: 30 µl/min, association: 120-240 s, dissociation: 60/360-600 s). Binding parameters were obtained from the processed data by fitting a 1:1 interaction model using Biacore Insight Evaluation software supplied with the device.

5.4.10 Electron microscopy

Negative stain electron microscopy (EM) was employed to evaluate protein sample quality, focusing on aggregation, heterogeneity, and overall integrity prior to further structure determination. In this technique, proteins are adsorbed onto an electron-transparent support grid (EM grid) and stained with an amorphous layer of heavy metal salts to enhance electron scattering, thereby improving image contrast. Next, the sample is visualized using a transmission electron microscope (TEM). In this process, electrons interact with the specimen to generate an image that is recorded by a detector. For negative-stain EM, carbon-coated copper grids were glow-discharged to increase hydrophilicity. The grids were then incubated for 1 minute with 5 µl of the target protein sample. Excess sample was removed with blotting paper. The grid was washed by sequentially immersing it in three individual 20 µl drops of the corresponding purification buffer. Each time, residual liquid was blotted away. The grid was stained with 2 % uranyl acetate for 30 seconds, after which the stain was carefully blotted off, and the grid was air-dried. Imaging was carried out on a JEOL JEM-2200FS TEM operating at 200 kV and equipped with a CMOS camera (TemCam-F416). Micrographs were collected at magnifications ranging from 20,000× to 100,000×.

Cryo-electron microscopy (cryo-EM) was employed to determine the three-dimensional structure of protein complexes at high resolution. Purified samples were concentrated to various concentrations (0.5 – 2 mg/ml, 4 µl) and applied to glow-discharged Quantifoil grids (R 1.2/1.3 holey carbon copper or gold). Excess liquid was blotted (2-8 sec) under controlled temperature and humidity conditions using a Vitrobot Mark IV (Thermo Fisher Scientific), then the samples were rapidly vitrified in liquid ethane cooled by liquid nitrogen. The grids were stored in liquid nitrogen until imaging.

Screening and data collection was performed on a Talos Arctica or a Krios Titan cryo-transmission electron microscope (cryo-TEM) (Thermo Fisher Scientific) operated at 200 or 300 kV. Data collection was done either at the StruBiTEM facility (University of Cologne) or at the Ernst Ruska Center for microscopy and spectroscopy with electrons (Forschungszentrum Jülich). Data analysis was performed with cryoSPARC.

6. Materials

All used chemicals, enzymes and other consumables, as well as used hardware and software are listed below. Moreover, this section contains a summary of plasmids, primer and all buffers and crystallization screens that have been used during this study.

6.1 Chemicals

The chemicals used in this work were purchased from the following suppliers: Carl Roth (Karlsruhe, Germany), Sigma-Aldrich (St Louis, USA), Applichem (Darmstadt, Germany), Thermo Fisher Scientific (Waltham, USA), Merck Millipore (Burlington, USA), VWR (Darmstadt, Germany), Jena Bioscience (Jena, Germany), Serva (Heidelberg, Germany), MedChemtronica (Sollentuna, Sweden), and Linde plc (Dublin, Ireland).

6.2 Consumables

Table 6-1: List of consumables with corresponding supplier.

Consumables	**Supplier**
96-deep well block (2 ml)	VWR
96-well microplates, round bottom	Greiner
Adhesive foil for crystallization plates	Molecular Dimensions
Blotting paper	Whatman plc
Falcon tubes (15 ml, 50 ml)	Greiner
Filter paper (0.22 µm)	Merck Millipore
Microcuvette kit for the NanoStar, disposable	Wyatt Technologies
MRC 2 Well Crystallization Plate (96-well)	Jena Bioscience
PCR tubes	Sarstedt
pH indicator paper	Carl Roth
Pipette tips (20 µl, 200 µl, 1000 µl)	VWR
Prometheus standard capillaries	NanoTemper Technologies
Reaction tubes (0.5 ml, 1 ml, 2 ml)	Eppendorf
Series S sensor chip SA	Cytiva
Serological pipettes (5 ml, 10 ml, 25 ml, 50 ml)	Sarstedt
SuperSignal™ West Pico PLUS Chemiluminescent Substrate	Invitrogen
Syringe filters (0.22 µm and 0.45 µm)	Carl Roth
Syringes (5 ml, 10 ml, 20 ml)	Carl Roth
Petri dishes	Labomedic
EVE™ cell counting slides	NanoEntek
Amicon™ ultracentrifugal filter	Merck Millipore
6-well tissue culture plate	Sarstedt
Carbon-coated EM grids	Plano
peqGreen DNA stain	VWR
DNA gel loading dye	New England Biolabs
BIAdesorb solutions	Cytiva
BIAnormalization solution (70 %)	Cytiva

6.3 Enzymes, marker, and kits

Table 6-2: List of enzymes, marker, and kits with corresponding suppliers.

Enzymes, marker, kits	Supplier
Restriction enzymes	New England Biolabs
CutSmart buffer	New England Biolabs
Q5 High Fidelity DNA Polymerase	New England Biolabs
GC enhancer	New England Biolabs
Q5 polymerase buffer	New England Biolabs
T4 DNA ligase	New England Biolabs
T4 DNA ligase buffer	New England Biolabs
DNaseI	Applichem
TEV protease	Institute of Structural Biology (Bonn)
PageRuler plus prestained protein ladder	Thermo Fisher Scientific
1 kbp DNA ladder	Carl Roth
100 bp DNA ladder	Carl Roth
ExtractMe DNA Clean-Up & Gel-Out Kit	Blrt
ExtractMe Plasmid Mini Kit	Blrt
ExtractMe Pladmid Midi Kit	Blrt
NucleoSpin Gel and PCR Clean-up	Macherey Nagel
NucleoSpin Plasmid EasyPure	Macherey Nagel

6.4 Crystallization screens

Table 6-3: List of crystallization screens with corresponding suppliers.

Crystallization screen	Supplier
JCSG plus	Jena Bioscience
Morpheus	Molecular Dimensions
ProPlex	Molecular Dimensions
PACT premier	Molecular Dimensions
LMB	Molecular Dimensions
Ligand friendly	Molecular Dimensions
MemGold	Molecular Dimensions

6.5 Solutions

Table 6-4: List of general used solutions.

Buffer/ Solution	Ingredients
APS solution	10 % APS in ddH2O
Coomassie staining solution	40 % (v/v) ethanol, 10 % (v/v) acetic acid, 0.1 % (w/v) Coomassie brilliant blue R250
Coomassie destain solution	10 % (v/v) ethanol, 5 % (v/v) acetic acid
PBS	20 mM Na2HPO4, 4.6 mM NaH2PO4, 150 mM NaCl; pH 7.5
PMSF solution	100 mM PMSF in isopropanol
SDS running buffer	25 mM Tris pH 8.3, 194 mM glycine, 0.1 % (w/v) SDS
SDS sample buffer (4x)	240 mM Tris pH 6.8, 8 % SDS, 5 % βME, 0.04 % bromophenol blue, 40 % glycerol

6.6 Vectors and oligonucleotides

Table 6-5: Vectors used during this work.

Vector	Resistance	Source
pACEBac1-MBP-tev	$Gent^R$	Geyer lab (University of Bonn)
pACEBac1-GST-tev	$Gent^R$	Geyer lab (University of Bonn)
pACEBac1-Avi-MBP-tev	$Gent^R$	Geyer lab (University of Bonn)
pGEX-4T1-GST-tev	Amp^R	GE Healthcare
pIRESpuro3-N-Avi	Amp^R	IFM Therapeutics
pSBinit2	Cam^R	Core Facility Nanobodies (University of Bonn)

Table 6-6: Amplification primer for restriction cloning.

Primer	Sequence
NOD2_fw (215+ BamHI)	cgcggatccgaagctgc
NOD2_rv (-1040 HindIII)	ataagaatgcggccgctcaaagcaagagtctg
NOD2_fw (1+ BamHI)	cgggatccatgggggaagag
NOD2_rv (-1040 XbaI)	cgtctagatcaaagcaagagtctgg
Fw NLRP12 V403I	agc ctc tct tca cca tgt gct tca tcc ccc t
Rv NLRP12 V403I	acc cag cac acc agg ggg atg aag cac
Fw NLRP12 S516T	tac tac agc ttc atc cac ttg act ttc cag
Rv NLRP12 S516T	ata gct gca aag aac tcc tgg aaa gtc aag tg
Fw NLRP12 G609S/S615Y	cct gca gca gag ctc ctt gga gtt ctt cta ctg ctt g
Rv NLRP12 G609S/S615Y	ctc gta caa gca gta gaa gaa ctc caa gga gct ctg ctg
Fw NLRP12 A642S/E646D	gtg gtc agc aac att tcc tcc aag atg gac cac atg
Rv NLRP12 A642S/E646D	cga gga gac cat gtg gtc cat ctt gga gga aat gtt g
Fw NLRP12 A557I/L558F	cgt ttt ctg aaa gga gct tcc tga tat tca cca g
Rv NLRP12 A557I/L558F	caa aca gga agc ggc tgg tga ata tca gga agc
Fw NLRP10 (4+ BamHI)	cgcggatccgccaaggccagaaagcc
Rv NLRP10 (-655 EcoRI)	ccggaattcttatatgtaagtatttttggtgtttcct
Rv NLRP10 (-482 EcoRI)	ccggaattcttactctttcaccaggtaag
Rv NLRP10 (-583 EcoRI)	ccggaattcttaattgttcatctgaatacc
Rv NLRP10 (-655 XbaI) C-tail mutant	gctctagattatatgtaagtattttgtggtgtttcct
Fw FAF2 (1+ NotI)	atttgcggccgcatggcggcg
Rv FAF2 (-445 XbaI)	gctctagatcattcgtcagttag
Fw TELO2 (1+ NotI)	atttgcggccgcatggagccagc
Rv TELO2 (-837 XbaI)	gctctagactagggagacgcggg
Fw TTI1 (1+ NotI)	atttgcggccgcatggcagtttttg
Rv TTI1 (-1089 HindIII)	ccccaagctttcactgcagctccttg

Table 6-7: Primer for site-directed mutagenesis.

Primer	Sequence
Fw NLRP12 (122-663) qc cac to taa	gtgctgtaattgtatggcgccacctac
Rv NLRP12 (122-663) qc cac to taa	catacaattacagcacctgggcgc
Fw NLRP12 (122-667) qc gcc to taa	gtatggctaaacctacagcgcggac

Rv NLRP12 (122-667) qc gcc to taa	gtaggtttagccatacaagtgcagcacc
Fw NLRP12 (122-676) qc gcc to taa	gaagactgagcgcggtaagaattcgc
Rv NLRP12 (122-676) qc gcc to taa	gcgctcagtcttccccgtcc
Fw NLRP12 I557A qc	cctggcattcaccagccg
Rv NLRP12 I557A qc	gtgaatgccaggaagctcctttcag
Fw NLRP10 K27E	gatttcaaggagttaaagttctac
Rv NLRP10 K27E	ctttaactccttgaaatcgttc
Fw NLRP10 E85R	gaacctgttgagacttgtggac
Rv NLRP10 E85R	cacaagtctcaacaggttcatg

6.7 Bacterial strains and cell lines

Table 6-8: List of bacterial strains and cell lines with corresponding suppliers.

Strain or cell line	Supplier
Escherichia coli (*E. coli*) DH5α	Thermo Fisher Scientific
E. coli NEBβ10	New England Biolabs
E. coli BL21 (DE3)	Thermo Fisher Scientific
E. coli WK6	Thermo Fisher Scientific
E. coli DH10 *Multi*Bac^{Turbo}	Geneva Biotech
Sf9 insect cells (clonal isolate of *Spodoptera frugiperda Sf21* cells [IPLB-*Sf21*-AE])	Thermo Fisher Scientific

6.8 Media and reagents

Table 6-9: List of media and cell culture reagents.

Media/ Reagent	Supplier
Lysogeny broth (LB) medium	10 g/L tryptone, 5 g/L yeast extract, 5 g/L NaCl; pH 7.0
Terrific broth (TB) medium	12 g/L tryptone, 24 g/L yeast extract, 4 ml/L Glycerol, 12.54 g/L K_2HPO_4, 2.31 g/L KH_2PO_4; pH 7.0
LB Agar plates	20 g/L agar in LB medium
Sf-900^{TM} III SFM	Invitrogen
Cellfectin^{TM} insect cell transfection reagent	Thermo Fisher Scientific
*Trans*IT^{TM} insect cell transfection reagent	Mirus Bio

6.9 Columns and resins

Table 6-10: List of used columns and affinity resins.

Column/ resin	Supplier
MBPTrap HP	GE Healthcare Europe
GSTrap FF	GE Healthcare Europe
Amylose resin	New England Biolabs
Glutathione agarose	Thermo Fisher Scientific
Ni-NTA agarose	Qiagen
HiLoad 16/600 Superdex 75 PG	GE Healthcare Europe
HiLoad 16/600 Superdex 200 PG	GE Healthcare Europe
Superdex 75 Increase 10/300 GL	GE Healthcare Europe

Superdex 200 Increase 10/300 GL	GE Healthcare Europe
Superdex 75 Increase 3.2/300	GE Healthcare Europe
Superdex 200 Increase 3.2/300	GE Healthcare Europe
Superose 6 Increase 10/300 GL	GE Healthcare Europe
Superose 6 Increase 3.2/300	GE Healthcare Europe
Chromolith Performance RP-18e 100-4.6	Merck Millipore

6.10 Devices

Table 6-11: List of used devices.

Device	Name	Manufacturer
Automatic cell counter	EVE	NanoEntek
Cell sonicator	SONOPULS HD3100	Bandelin electronic
Centrifuge	Avanti JXN 26	Beckman Coulter
Cooling cabinet	Unichromat 1500	Uniequip
Crystallization imager	Rock Imager 1000	Fromulatrix
Crystallization robot	Crystal Gryphon LCP	Art Robbins Instruments
DLS	DynaPro NanoStar	Wyatt
Electron microscope	JEM-2200FS	Jeol
FPLC	Äkta Start, Prime Plus, Pure	GE Healthcare
Gel casting and PAGE system	Mini-Protean Tetra Cell	Bio-Rad
Gel imager	ChemiDoc XRS+	Bio-Rad Laboratories
HPLC	1260 Infinity II	Agilent
Incubator	Multitron, Minitron	Infors HT
ITC	MicroCal PEAQ-ITC	Malvern Panalytical
MALS	miniDAWN	Wyatt
nanoDSF	Prometheus NT.48	NanoTemper
PCR thermocycler	Mastercycler Nexus SX1	Eppendorf
pH meter	Lab855	SI Analytics
Pipetting robot	epMotion 5073	Eppendorf
Spectrophotometer	NanoDrop DN-2000C	Thermo Scientific
SPR	Biacore 8K	GE Healthcare
Table top centrifuge (large)	Centrifuge 5804 R	Eppendorf
Table top centrifuge (small)	Centrifuge 5427 R	Eppendorf
Thermomixer	Thermomixer comfort	Eppendorf
Ultrasonic bath	USC100T	VWR
Water purification system	Milli-Q Direct	Merck Millipore

6.11 Software

Table 6-12: List of used software.

Software	Developer/ Company
Affinity Designer	Serif Ltd
AlphaFold2	Jumper et al. 2021
AlphaFold3	Abramson et al. 2024
Astra	Wyatt Technologies

Biacore Insight evaluation	GE Healthcare
CLC Sequence Viewer 7	Qiagen
ChimeraX-1.5	(RBVI), UCSF
CryoSPARC	Structura Biotechnology Inc.
DYNAMICS	Wyatt Technologies
ESPript 3.0	Webserver
GraphPad Prism 10	Dotmatics
ImageLab 6.0.1	Bio-Rad
Office for Mac	Microsoft
OpenLab 2.2 and 3.4	Agilent Technologies
ProtParam (Expasy)	Swiss Institute of Bioinformatics
PyMOL	Schrödinger LLC
Scaffold 5	Proteome Software
SnapGene	Dotmatics

7. Additional Figures

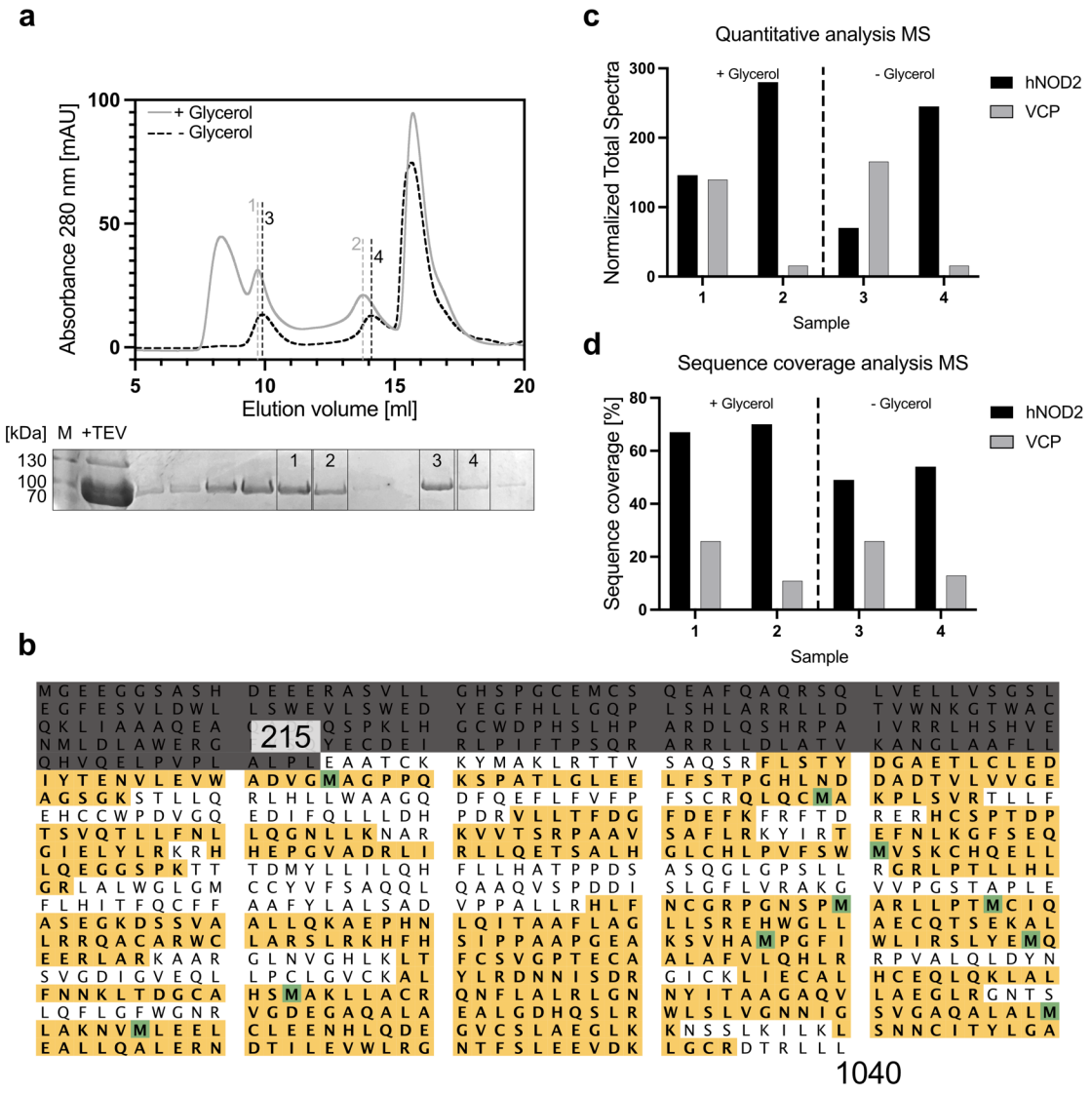

Figure 7-1: Peptide mass fingerprint analysis of the NOD2-VCP complex.
*(**a**) Size exclusion chromatography profiles of humanNOD2ΔCARDs after amylose affinity chromatography using an Äkta Pure system and a Superdex 200 inc 10/300 column. The x- axis shows the elution volume in ml and the y- axis the UV absorption at 280 nm in mAU. The different samples for mass spectrometry analysis are indicated. Grey with 10 % glycerol, black without glycerol in buffer. Polyacrylamide gel showing S1 to S4 which were used for mass spectrometry analysis. S1 and S3 are supposed to be an oligomeric species, S2 and S4 are supposed to be monomeric species. (hNOD2ΔCARDs (TEV-cleaved), calculated MW: 91.4 kDa and VCP (Sf9), calculated MW: 89.3 kDa) (**b**) Result of mass spectrometry analysis with sequence coverage marked in yellow. Example shown for hNOD2ΔCARDs in S1. (**c**) Quantitative analysis of mass spectrometry samples shown as normalized values. Black bars represent hNOD2ΔCARDs and grey bars represent VCP (Sf9). (**d**) Sequence coverage analysis of mass spectrometry samples shows the percentage of covered sequences.*

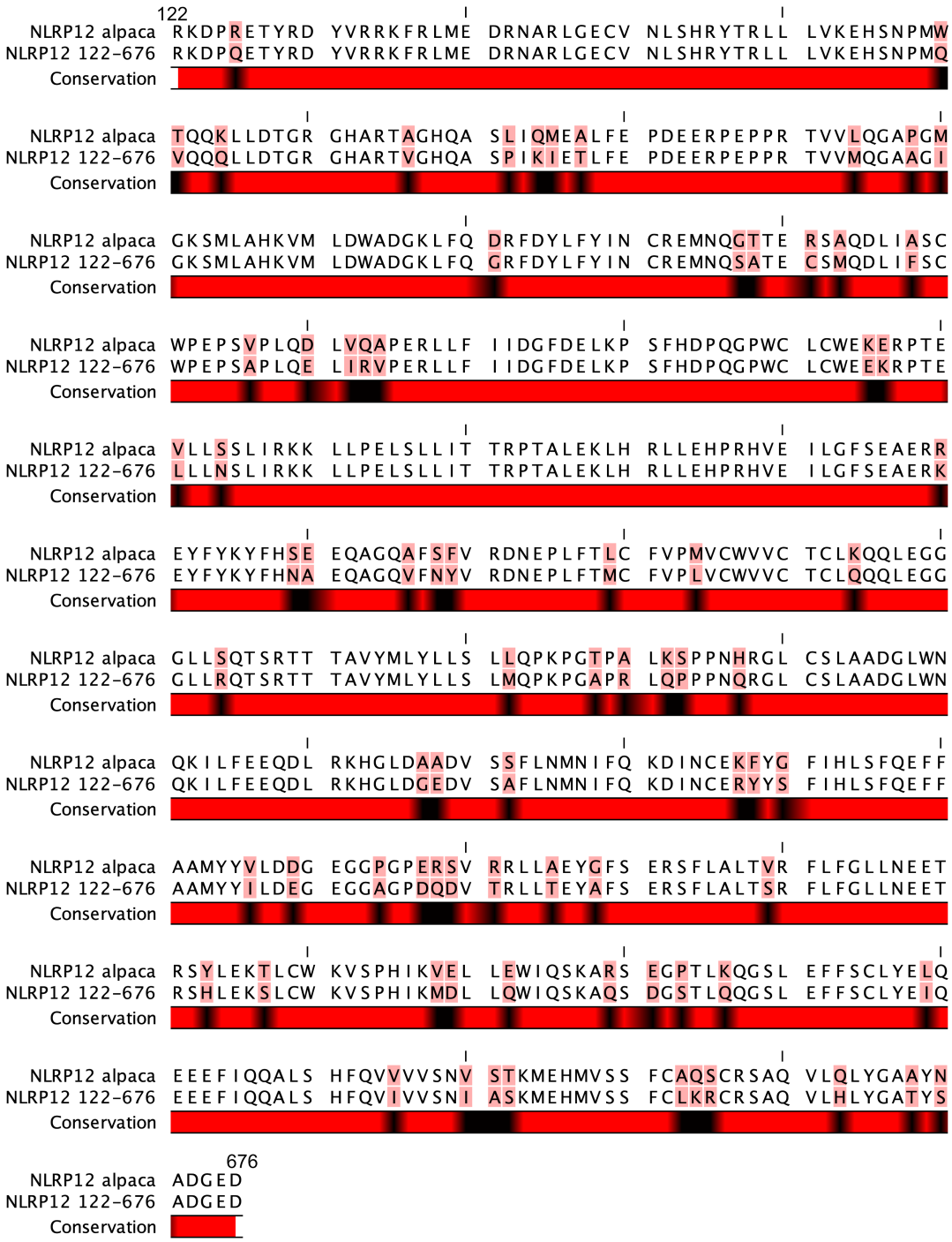

Figure 7-2: Sequence alignment of NLRP12^{NACHT} in humans and alpacas.
The amino acid sequence alignment between human NLRP12 and alpaca NLRP12 shows a sequence identity of 85.8 %.

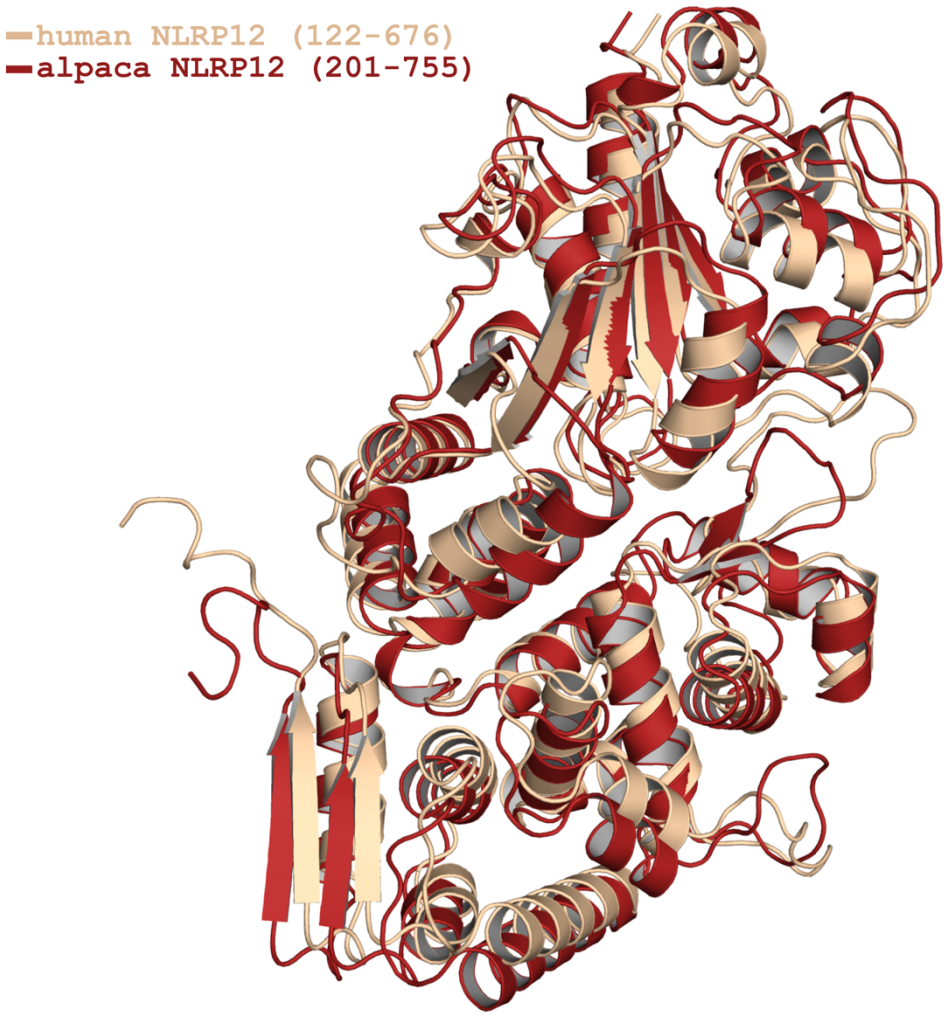

Figure 7-3: Structure alignment of NLRP12^{NACHT} in humans and alpacas.
Structure alignment of human NLRP12 (122-676) with alpaca NLRP12 (201-755). AlphaFold predictions were used.

8. References

Abramson, J., Adler, J., Dunger, J., Evans, R., Green, T., Pritzel, A., Ronneberger, O., Willmore, L., Ballard, A. J., Bambrick, J., Bodenstein, S. W., Evans, D. A., Hung, C.-C., O'Neill, M., Reiman, D., Tunyasuvunakool, K., Wu, Z., Žemgulytė, A., Arvaniti, E., … Jumper, J. M. (2024). Accurate structure prediction of biomolecular interactions with AlphaFold 3. *Nature*, *630*(8016), 493–500. https://doi.org/10.1038/s41586-024-07487-w

Akira, S., Takeda, K., & Kaisho, T. (2001). Toll-like receptors: critical proteins linking innate and acquired immunity. *Nature Immunology*, *2*(8), 675–680. https://doi.org/10.1038/90609

Ataide, M. A., Andrade, W. A., Zamboni, D. S., Wang, D., Souza, M. do C., Franklin, B. S., Elian, S., Martins, F. S., Pereira, D., Reed, G., Fitzgerald, K. A., Golenbock, D. T., & Gazzinelli, R. T. (2014). Malaria-Induced NLRP12/NLRP3-Dependent Caspase-1 Activation Mediates Inflammation and Hypersensitivity to Bacterial Superinfection. *PLoS Pathogens*, *10*(1), e1003885. https://doi.org/10.1371/journal.ppat.1003885

Balka, K. R., & Nardo, D. D. (2019). Understanding early TLR signaling through the Myddosome. *Journal of Leukocyte Biology*, *105*(2), 339–351. https://doi.org/10.1002/jlb.mr0318-096r

Bamming, D., & Horvath, C. M. (2009). Regulation of Signal Transduction by Enzymatically Inactive Antiviral RNA Helicase Proteins MDA5, RIG-I, and LGP2*. *Journal of Biological Chemistry*, *284*(15), 9700–9712. https://doi.org/10.1074/jbc.m807365200

Banerjee, S., Bartesaghi, A., Merk, A., Rao, P., Bulfer, S. L., Yan, Y., Green, N., Mroczkowski, B., Neitz, R. J., Wipf, P., Falconieri, V., Deshaies, R. J., Milne, J. L. S., Huryn, D., Arkin, M., & Subramaniam, S. (2016). 2.3 Å resolution cryo-EM structure of human p97 and mechanism of allosteric inhibition. *Science*, *351*(6275), 871–875. https://doi.org/10.1126/science.aad7974

Bauernfeind, F. G., Horvath, G., Stutz, A., Alnemri, E. S., MacDonald, K., Speert, D., Fernandes-Alnemri, T., Wu, J., Monks, B. G., Fitzgerald, K. A., Hornung, V., & Latz, E. (2009). Cutting Edge: NF-κB Activating Pattern Recognition and Cytokine Receptors License NLRP3 Inflammasome Activation by Regulating NLRP3 Expression. *The Journal of Immunology*, *183*(2), 787–791. https://doi.org/10.4049/jimmunol.0901363

Bauernfried, S., Scherr, M. J., Pichlmair, A., Duderstadt, K. E., & Hornung, V. (2021). Human NLRP1 is a sensor for double-stranded RNA. *Science*, *371*(6528). https://doi.org/10.1126/science.abd0811

Bonilla, F. A., & Oettgen, H. C. (2010). Adaptive immunity. *Journal of Allergy and Clinical Immunology*, *125*(2), S33–S40. https://doi.org/10.1016/j.jaci.2009.09.017

Booshehri, L. M., & Hoffman, H. M. (2019). CAPS and NLRP3. *Journal of Clinical Immunology*, *39*(3), 277–286. https://doi.org/10.1007/s10875-019-00638-z

Borzutzky, A., Fried, A., Chou, J., Bonilla, F. A., Kim, S., & Dedeoglu, F. (2010). NOD2-associated diseases: Bridging innate immunity and autoinflammation. *Clinical Immunology*, *134*(3), 251–261. https://doi.org/10.1016/j.clim.2009.05.005

Brinkschulte, R., Fußhöller, D. M., Hoss, F., Rodríguez-Alcázar, J. F., Lauterbach, M. A., Kolbe, C.-C., Rauen, M., Ince, S., Herrmann, C., Latz, E., & Geyer, M. (2022). ATP-binding and hydrolysis of human NLRP3. *Communications Biology*, *5*(1), 1176. https://doi.org/10.1038/s42003-022-04120-2

Broske, B., Binder, S. C., McEnroe, B. A., Kempchen, T. N., Fandrey, C. I., Messmer, J. M., Tan, E., Konopka, P., Ferber, D., Yong, M. C. R., Kleinert, M., Hoch, A., Blumenstock, K., Tödtmann, J. M. P., Oldenburg, J., Rühl, H., Semaan, A., Toma, M. I., Markova, K., … Hölzel, M. (2025). Development of AI-designed protein binders for detection and targeting of cancer cell surface proteins. *bioRxiv*, 2025.05.11.652819. https://doi.org/10.1101/2025.05.11.652819

Brown, G. D. (2006). Dectin-1: a signalling non-TLR pattern-recognition receptor. *Nature Reviews Immunology*, *6*(1), 33–43. https://doi.org/10.1038/nri1745

Broz, P., Pelegrín, P., & Shao, F. (2020). The gasdermins, a protein family executing cell death and inflammation. *Nature Reviews Immunology*, *20*(3), 143–157. https://doi.org/10.1038/s41577-019-0228-2

Caffrey, B., Zhu, X., Berezuk, A., Tuttle, K., Chittori, S., & Subramaniam, S. (2021). AAA+ ATPase p97/VCP mutants and inhibitor binding disrupt inter-domain coupling and subsequent allosteric activation. *Journal of Biological Chemistry*, *297*(4), 101187. https://doi.org/10.1016/j.jbc.2021.101187

Caruso, R., Warner, N., Inohara, N., & Núñez, G. (2014). NOD1 and NOD2: Signaling, Host Defense, and Inflammatory Disease. *Immunity*, *41*(6), 898–908. https://doi.org/10.1016/j.immuni.2014.12.010

Cho, J. H. (2001). The Nod2 Gene in Crohn's Disease: Implications for Future Research Into the Genetics and Immunology of Crohn's Disease. *Inflammatory Bowel Diseases*, *7*(3), 271–275. https://doi.org/10.1097/00054725-200108000-00014

Cho, Y., Cao, Z., Luo, X., Tian, J. J., Hukkanen, R. R., Hussien, R., Cancilla, B., Chowdhury, P., Li, F., Ma, S., LaGory, E. L., Schroeder, M., Dusenberry, A., Marshall, L., Hawkins, J., Campagne, M. van L., & Zhou, Y. (2024). NLRP10 maintains epidermal homeostasis by promoting keratinocyte survival and P63-dependent differentiation and barrier function. *Cell Death & Disease*, *15*(10), 759. https://doi.org/10.1038/s41419-024-07146-y

Chou, W.-C., Jha, S., Linhoff, M. W., & Ting, J. P.-Y. (2023). The NLR gene family: from discovery to present day. *Nature Reviews Immunology*, *23*(10), 635–654. https://doi.org/10.1038/s41577-023-00849-x

Chui, A. J., Okondo, M. C., Rao, S. D., Gai, K., Griswold, A. R., Johnson, D. C., Ball, D. P., Taabazuing, C. Y., Orth, E. L., Vittimberga, B. A., & Bachovchin, D. A. (2019). N-terminal degradation activates the NLRP1B inflammasome. *Science*, *364*(6435), 82–85. https://doi.org/10.1126/science.aau1208

Coll, R. C., Robertson, A. A. B., Chae, J. J., Higgins, S. C., Muñoz-Planillo, R., Inserra, M. C., Vetter, I., Dungan, L. S., Monks, B. G., Stutz, A., Croker, D. E., Butler, M. S., Haneklaus, M., Sutton, C. E., Núñez, G., Latz, E., Kastner, D. L., Mills, K. H. G., Masters, S. L., … O'Neill, L. A. J. (2015). A small-molecule inhibitor of the NLRP3 inflammasome for the treatment of inflammatory diseases. *Nature Medicine*, *21*(3), 248–255. https://doi.org/10.1038/nm.3806

Coombs, J. R., Zamoshnikova, A., Holley, C. L., Maddugoda, M. P., Teo, D. E. T., Chauvin, C., Poulin, L. F., Vitak, N., Ross, C. M., Mellacheruvu, M., Coll, R. C., Heinz, L. X., Burgener, S. S., Emming, S., Chamaillard, M., Boucher, D., & Schroder, K. (2024). NLRP12 interacts with NLRP3 to block the activation of the human NLRP3 inflammasome. *Science Signaling*, *17*(820), eabg8145. https://doi.org/10.1126/scisignal.abg8145

Creagh, E. M., & O'Neill, L. A. J. (2006). TLRs, NLRs and RLRs: a trinity of pathogen sensors that co-operate in innate immunity. *Trends in Immunology*, *27*(8), 352–357. https://doi.org/10.1016/j.it.2006.06.003

Damm, A., Lautz, K., & Kufer, T. A. (2013). Roles of NLRP10 in innate and adaptive immunity. *Microbes and Infection*, *15*(6–7), 516–523. https://doi.org/10.1016/j.micinf.2013.03.008

Danot, O., Marquenet, E., Vidal-Ingigliardi, D., & Richet, E. (2009). Wheel of Life, Wheel of Death: A Mechanistic Insight into Signaling by STAND Proteins. *Structure*, *17*(2), 172–182. https://doi.org/10.1016/j.str.2009.01.001

Dekker, C., Mattes, H., Wright, M., Boettcher, A., Hinniger, A., Hughes, N., Kapps-Fouthier, S., Eder, J., Erbel, P., Stiefl, N., Mackay, A., & Farady, C. J. (2021). Crystal Structure of NLRP3 NACHT Domain With an Inhibitor Defines Mechanism of Inflammasome Inhibition. *Journal of Molecular Biology*, *433*(24), 167309. https://doi.org/10.1016/j.jmb.2021.167309

DeLaBarre, B., & Brunger, A. T. (2003). Complete structure of p97/valosin-containing protein reveals communication between nucleotide domains. *Nature Structural & Molecular Biology*, *10*(10), 856–863. https://doi.org/10.1038/nsb972

Deltcheva, E., Chylinski, K., Sharma, C. M., Gonzales, K., Chao, Y., Pirzada, Z. A., Eckert, M. R., Vogel, J., & Charpentier, E. (2011). CRISPR RNA maturation by trans-encoded small RNA and host factor RNase III. *Nature*, *471*(7340), 602–607. https://doi.org/10.1038/nature09886

Duan, T., Du, Y., Xing, C., Wang, H. Y., & Wang, R.-F. (2022). Toll-Like Receptor Signaling and Its Role in Cell-Mediated Immunity. *Frontiers in Immunology*, *13*, 812774. https://doi.org/10.3389/fimmu.2022.812774

Duhoo, Y., Roche, J., Trinh, T. T. N., Desmyter, A., Gaubert, A., Kellenberger, C., Cambillau, C., Roussel, A., & Leone, P. (2017). Camelid nanobodies used as crystallization chaperones for different constructs of PorM, a component of the type IX secretion system from Porphyromonas gingivalis. *Acta Crystallographica Section F*, *73*(5), 286–293. https://doi.org/10.1107/s2053230x17005969

Fukuda, D., Nishimoto, S., Aini, K., Tanaka, A., Nishiguchi, T., Kim-Kaneyama, J., Lei, X., Masuda, K., Naruto, T., Tanaka, K., Higashikuni, Y., Hirata, Y., Yagi, S., Kusunose, K., Yamada, H., Soeki, T., Imoto, I., Akasaka, T., Shimabukuro, M., & Sata, M. (2019). Toll-Like Receptor 9 Plays a Pivotal Role in Angiotensin II–Induced Atherosclerosis. *Journal of the American Heart Association*, *8*(7), e010860. https://doi.org/10.1161/jaha.118.010860

Gay, N. J. (2019). Role of self-organising myddosome oligomers in inflammatory signalling by Toll-like receptors. *BMC Biology*, *17*(1), 15. https://doi.org/10.1186/s12915-019-0637-5

Geijtenbeek, T. B. H., & Gringhuis, S. I. (2009). Signalling through C-type lectin receptors: shaping immune responses. *Nature Reviews Immunology*, *9*(7), 465–479. https://doi.org/10.1038/nri2569

Ghalandary, M., Li, Y., Fröhlich, T., Magg, T., Liu, Y., Rohlfs, M., Hollizeck, S., Conca, R., Schwerd, T., Uhlig, H. H., Bufler, P., Koletzko, S., Muise, A. M., Snapper, S. B., Hauck, F., Klein, C., & Kotlarz, D. (2022). Valosin-containing protein-regulated endoplasmic reticulum stress causes NOD2-dependent inflammatory responses. *Scientific Reports*, *12*(1), 3906. https://doi.org/10.1038/s41598-022-07804-1

Gharagozloo, M., Mahmoud, S., Simard, C., Mahvelati, T. M., Amrani, A., & Gris, D. (2018). The Dual Immunoregulatory function of Nlrp12 in T Cell-Mediated Immune Response: Lessons from Experimental Autoimmune Encephalomyelitis. *Cells*, *7*(9), 119. https://doi.org/10.3390/cells7090119

Ghimire, L., Paudel, S., Jin, L., & Jeyaseelan, S. (2020). The NLRP6 inflammasome in health and disease. *Mucosal Immunology*, *13*(3), 388–398. https://doi.org/10.1038/s41385-020-0256-z

Girardin, S. E., Boneca, I. G., Viala, J., Chamaillard, M., Labigne, A., Thomas, G., Philpott, D. J., & Sansonetti, P. J. (2003). Nod2 Is a General Sensor of Peptidoglycan through Muramyl Dipeptide (MDP) Detection*. *Journal of Biological Chemistry*, *278*(11), 8869–8872. https://doi.org/10.1074/jbc.c200651200

Goubau, D., Deddouche, S., & Reis e Sousa, C. (2013). Cytosolic Sensing of Viruses. *Immunity*, *38*(5), 855–869. https://doi.org/10.1016/j.immuni.2013.05.007

Gram, A. M., Wright, J. A., Pickering, R. J., Lam, N. L., Booty, L. M., Webster, S. J., & Bryant, C. E. (2020). Salmonella Flagellin Activates NAIP/NLRC4 and Canonical NLRP3 Inflammasomes in Human Macrophages. *The Journal of Immunology*, *206*(3), ji2000382. https://doi.org/10.4049/jimmunol.2000382

Grimes, C. L., Ariyananda, L. D. Z., Melnyk, J. E., & O'Shea, E. K. (2012). The Innate Immune Protein Nod2 Binds Directly to MDP, a Bacterial Cell Wall Fragment. *Journal of the American Chemical Society*, *134*(33), 13535–13537. https://doi.org/10.1021/ja303883c

Heim, V. J., Stafford, C. A., & Nachbur, U. (2019). NOD Signaling and Cell Death. *Frontiers in Cell and Developmental Biology*, *7*, 208. https://doi.org/10.3389/fcell.2019.00208

Hirota, T., Takahashi, A., Kubo, M., Tsunoda, T., Tomita, K., Sakashita, M., Yamada, T., Fujieda, S., Tanaka, S., Doi, S., Miyatake, A., Enomoto, T., Nishiyama, C., Nakano, N., Maeda, K., Okumura, K., Ogawa, H., Ikeda, S., Noguchi, E., … Tamari, M. (2012). Genome-wide association study identifies eight new susceptibility loci for atopic dermatitis in the Japanese population. *Nature Genetics*, *44*(11), 1222–1226. https://doi.org/10.1038/ng.2438

Hochheiser, I. V., Behrmann, H., Hagelueken, G., Rodríguez-Alcázar, J. F., Kopp, A., Latz, E., Behrmann, E., & Geyer, M. (2022). Directionality of PYD filament growth determined by the transition of NLRP3 nucleation seeds to ASC elongation. *Science Advances*, *8*(19), eabn7583. https://doi.org/10.1126/sciadv.abn7583

Hochheiser, I. V., Pilsl, M., Hagelueken, G., Moecking, J., Marleaux, M., Brinkschulte, R., Latz, E., Engel, C., & Geyer, M. (2022). Structure of the NLRP3 decamer bound to the cytokine release inhibitor CRID3. *Nature*, *604*(7904), 184–189. https://doi.org/10.1038/s41586-022-04467-w

Høivik, M. L., Moum, B., Solberg, I. C., Henriksen, M., Cvancarova, M., Bernklev, T., & Group, I. (2013). Work disability in inflammatory bowel disease patients 10 years after disease onset: results from the IBSEN Study. *Gut*, *62*(3), 368. https://doi.org/10.1136/gutjnl-2012-302311

Hollingsworth, L. R., Sharif, H., Griswold, A. R., Fontana, P., Mintseris, J., Dagbay, K. B., Paulo, J. A., Gygi, S. P., Bachovchin, D. A., & Wu, H. (2021). DPP9 sequesters the C terminus of NLRP1 to repress inflammasome activation. *Nature*, *592*(7856), 778–783. https://doi.org/10.1038/s41586-021-03350-4

Hu, Z., Yan, C., Liu, P., Huang, Z., Ma, R., Zhang, C., Wang, R., Zhang, Y., Martinon, F., Miao, D., Deng, H., Wang, J., Chang, J., & Chai, J. (2013). Crystal Structure of NLRC4 Reveals Its Autoinhibition Mechanism. *Science*, *341*(6142), 172–175. https://doi.org/10.1126/science.1236381

Huang, L., Tao, Y., Wu, X., Wu, J., Shen, M., & Zheng, Z. (2023). The role of NLRP12 in inflammatory diseases. *European Journal of Pharmacology*, *956*, 175995. https://doi.org/10.1016/j.ejphar.2023.175995

Huang, Y.-H., Lo, M.-H., Cai, X.-Y., & Kuo, H.-C. (2018). Epigenetic hypomethylation and upregulation of NLRC4 and NLRP12 in Kawasaki disease. *Oncotarget*, *9*(27), 18939–18948. https://doi.org/10.18632/oncotarget.24851

Huoh, Y., & Hur, S. (2022). Death domain fold proteins in immune signaling and transcriptional regulation. *The FEBS Journal*, *289*(14), 4082–4097. https://doi.org/10.1111/febs.15901

Imamura, R., Wang, Y., Kinoshita, T., Suzuki, M., Noda, T., Sagara, J., Taniguchi, S., Okamoto, H., & Suda, T. (2010). Anti-Inflammatory Activity of PYNOD and Its Mechanism in Humans and Mice. *The Journal of Immunology*, *184*(10), 5874–5884. https://doi.org/10.4049/jimmunol.0900779

Ingraham, J. B., Baranov, M., Costello, Z., Barber, K. W., Wang, W., Ismail, A., Frappier, V., Lord, D. M., Ng-Thow-Hing, C., Vlack, E. R. V., Tie, S., Xue, V., Cowles, S. C., Leung, A., Rodrigues, J. V., Morales-Perez, C. L., Ayoub, A. M., Green, R., Puentes, K., … Grigoryan, G. (2023). Illuminating protein space with a programmable generative model. *Nature*, *623*(7989), 1070–1078. https://doi.org/10.1038/s41586-023-06728-8

Inohara, N., & Nuñez, G. (2001). The NOD: a signaling module that regulates apoptosis and host defense against pathogens. *Oncogene*, *20*(44), 6473–6481. https://doi.org/10.1038/sj.onc.1204787

Inohara, N., Ogura, Y., Fontalba, A., Gutierrez, O., Pons, F., Crespo, J., Fukase, K., Inamura, S., Kusumoto, S., Hashimoto, M., Foster, S. J., Moran, A. P., Fernandez-Luna, J. L., & Nuñez, G. (2003). Host Recognition of Bacterial Muramyl Dipeptide Mediated through NOD2 IMPLICATIONS FOR CROHN′S DISEASE*. *Journal of Biological Chemistry*, *278*(8), 5509–5512. https://doi.org/10.1074/jbc.c200673200

Janeway, C. A. (1989). Approaching the Asymptote? Evolution and Revolution in Immunology. *Cold Spring Harbor Symposia on Quantitative Biology*, *54*(0), 1–13. https://doi.org/10.1101/sqb.1989.054.01.003

Janeway, Travers, & Walport. (2001). *Immunobiology: The Immune System in Health and Disease. 5th edition.* Garland Science.

Jansen, Ruud., Embden, Jan. D. A. van, Gaastra, Wim., & Schouls, Leo. M. (2002). Identification of genes that are associated with DNA repeats in prokaryotes. *Molecular Microbiology*, *43*(6), 1565–1575. https://doi.org/10.1046/j.1365-2958.2002.02839.x

Jessop, M., Felix, J., & Gutsche, I. (2021). AAA+ ATPases: structural insertions under the magnifying glass. *Current Opinion in Structural Biology*, *66*, 119–128. https://doi.org/10.1016/j.sbi.2020.10.027

Jiang, F., Taylor, D. W., Chen, J. S., Kornfeld, J. E., Zhou, K., Thompson, A. J., Nogales, E., & Doudna, J. A. (2016). Structures of a CRISPR-Cas9 R-loop complex primed for DNA cleavage. *Science*, *351*(6275), 867–871. https://doi.org/10.1126/science.aad8282

Jin, T., Chuenchor, W., Jiang, J., Cheng, J., Li, Y., Fang, K., Huang, M., Smith, P., & Xiao, T. S. (2017). Design of an expression system to enhance MBP-mediated crystallization. *Scientific Reports*, *7*(1), 40991. https://doi.org/10.1038/srep40991

Jin, Y., Wu, W., Zhang, W., Zhao, Y., Wu, Y., Ge, G., Ba, Y., Guo, Q., Gao, T., Chi, X., Hao, H., Wang, J., & Feng, F. (2017). Involvement of EGF receptor signaling and NLRP12 inflammasome in fine particulate matter-induced lung inflammation in mice. *Environmental Toxicology*, *32*(4), 1121–1134. https://doi.org/10.1002/tox.22308

Jinek, M., Chylinski, K., Fonfara, I., Hauer, M., Doudna, J. A., & Charpentier, E. (2012). A Programmable Dual-RNA–Guided DNA Endonuclease in Adaptive Bacterial Immunity. *Science*, *337*(6096), 816–821. https://doi.org/10.1126/science.1225829

Joly, S., Eisenbarth, S. C., Olivier, A. K., Williams, A., Kaplan, D. H., Cassel, S. L., Flavell, R. A., & Sutterwala, F. S. (2012). Cutting Edge: Nlrp10 Is Essential for Protective Antifungal Adaptive Immunity against Candida albicans. *The Journal of Immunology*, *189*(10), 4713–4717. https://doi.org/10.4049/jimmunol.1201715

Jumper, J., Evans, R., Pritzel, A., Green, T., Figurnov, M., Ronneberger, O., Tunyasuvunakool, K., Bates, R., Žídek, A., Potapenko, A., Bridgland, A., Meyer, C., Kohl, S. A. A., Ballard, A. J., Cowie, A., Romera-Paredes, B., Nikolov, S., Jain, R., Adler, J., … Hassabis, D. (2021). Highly accurate protein structure prediction with AlphaFold. *Nature*, *596*(7873), 583–589. https://doi.org/10.1038/s41586-021-03819-2

Kalia, N., Singh, J., & Kaur, M. (2021). The role of dectin-1 in health and disease. *Immunobiology*, *226*(2), 152071. https://doi.org/10.1016/j.imbio.2021.152071

Kaper, J. B., Morris, J. G., & Levine, M. M. (1995). Cholera. *Clinical Microbiology Reviews*, *8*(1), 48–86. https://doi.org/10.1128/cmr.8.1.48

Kersse, K., Verspurten, J., Berghe, T. V., & Vandenabeele, P. (2011). The death-fold superfamily of homotypic interaction motifs. *Trends in Biochemical Sciences*, *36*(10), 541–552. https://doi.org/10.1016/j.tibs.2011.06.006

Keuler, T., Ferber, D., Marleaux, M., Geyer, M., & Gütschow, M. (2022). Structure–Stability Relationship of NLRP3 Inflammasome-Inhibiting Sulfonylureas. *ACS Omega*, *7*(9), 8158–8162. https://doi.org/10.1021/acsomega.2c00125

Kim, H.-J., Kim, H., Lee, J.-H., & Hwangbo, C. (2023). Toll-like receptor 4 (TLR4): new insight immune and aging. *Immunity & Ageing*, *20*(1), 67. https://doi.org/10.1186/s12979-023-00383-3

Kim, Y. K., Shin, J.-S., & Nahm, M. H. (2016). NOD-Like Receptors in Infection, Immunity, and Diseases. *Yonsei Medical Journal*, *57*(1), 5–14. https://doi.org/10.3349/ymj.2016.57.1.5

Kim, Y., Park, J., Joo, S. Y., Kim, B.-G., Jo, A., Lee, H., & Cho, Y. (2022). Structure of the Human TELO2-TTI1-TTI2 Complex. *Journal of Molecular Biology*, *434*(2), 167370. https://doi.org/10.1016/j.jmb.2021.167370

Kopp, A., Hagelueken, G., Jamitzky, I., Moecking, J., Schiffelers, L. D. J., Schmidt, F. I., & Geyer, M. (2023). Pyroptosis inhibiting nanobodies block Gasdermin D pore formation. *Nature Communications*, *14*(1), 7923. https://doi.org/10.1038/s41467-023-43707-z

Koyano, F., Yamano, K., Hoshina, T., Kosako, H., Fujiki, Y., Tanaka, K., & Matsuda, N. (2024). AAA+ ATPase chaperone p97/VCPFAF2 governs basal pexophagy. *Nature Communications*, *15*(1), 9347. https://doi.org/10.1038/s41467-024-53558-x

Lautz, K., Damm, A., Menning, M., Wenger, J., Adam, A. C., Zigrino, P., Kremmer, E., & Kufer, T. A. (2012). NLRP10 enhances Shigella-induced pro-inflammatory responses. *Cellular Microbiology*, *14*(10), 1568–1583. https://doi.org/10.1111/j.1462-5822.2012.01822.x

Leipe, D. D., Koonin, E. V., & Aravind, L. (2004). STAND, a Class of P-Loop NTPases Including Animal and Plant Regulators of Programmed Cell Death: Multiple, Complex Domain Architectures, Unusual Phyletic Patterns, and Evolution by Horizontal Gene Transfer. *Journal of Molecular Biology*, *343*(1), 1–28. https://doi.org/10.1016/j.jmb.2004.08.023

Lemaitre, B., & Hoffmann, J. (2007). The Host Defense of Drosophila melanogaster. *Annual Review of Immunology*, *25*(1), 697–743. https://doi.org/10.1146/annurev.immunol.25.022106.141615

Li, D., & Wu, M. (2021). Pattern recognition receptors in health and diseases. *Signal Transduction and Targeted Therapy*, *6*(1), 291. https://doi.org/10.1038/s41392-021-00687-0

Lim, K.-H., & Staudt, L. M. (2013). Toll-Like Receptor Signaling. *Cold Spring Harbor Perspectives in Biology*, *5*(1), a011247. https://doi.org/10.1101/cshperspect.a011247

Liu, H., & Naismith, J. H. (2008). An efficient one-step site-directed deletion, insertion, single and multiple-site plasmid mutagenesis protocol. *BMC Biotechnology*, *8*(1), 91–91. https://doi.org/10.1186/1472-6750-8-91

Madeira, F., Madhusoodanan, N., Lee, J., Eusebi, A., Niewielska, A., Tivey, A. R. N., Lopez, R., & Butcher, S. (2024). The EMBL-EBI Job Dispatcher sequence analysis tools framework in 2024. *Nucleic Acids Research*, *52*(W1), W521–W525. https://doi.org/10.1093/nar/gkae241

Maekawa, S., Ohto, U., Shibata, T., Miyake, K., & Shimizu, T. (2016). Crystal structure of NOD2 and its implications in human disease. *Nature Communications*, *7*(1), 11813. https://doi.org/10.1038/ncomms11813

Manglik, A., Kobilka, B. K., & Steyaert, J. (2016). Nanobodies to Study G Protein–Coupled Receptor Structure and Function. *Annual Review of Pharmacology and Toxicology*, *57*(1), 19–37. https://doi.org/10.1146/annurev-pharmtox-010716-104710

Marquenet, E., & Richet, E. (2010). Conserved Motifs Involved in ATP Hydrolysis by MalT, a Signal Transduction ATPase with Numerous Domains from Escherichia coli. *Journal of Bacteriology*, *192*(19), 5181–5191. https://doi.org/10.1128/jb.00522-10

Martinon, F., Burns, K., & Tschopp, J. (2002). The Inflammasome A Molecular Platform Triggering Activation of Inflammatory Caspases and Processing of proIL-β. *Molecular Cell*, *10*(2), 417–426. https://doi.org/10.1016/s1097-2765(02)00599-3

Mason, D. R., Beck, P. L., & Muruve, D. A. (2011). Nucleotide-Binding Oligomerization Domain-Like Receptors and Inflammasomes in the Pathogenesis of Non-Microbial Inflammation and Diseases. *Journal of Innate Immunity*, *4*(1), 16–30. https://doi.org/10.1159/000334247

Masters, S. L. (2023). Ten things to know about NLRP10. *Nature Immunology*, *24*(4), 561–562. https://doi.org/10.1038/s41590-023-01466-5

Matico, R. E., Yu, X., Miller, R., Somani, S., Ricketts, M. D., Kumar, N., Steele, R. A., Medley, Q., Berger, S., Faustin, B., & Sharma, S. (2024). Structural basis of the human NAIP/NLRC4 inflammasome assembly and pathogen sensing. *Nature Structural & Molecular Biology*, *31*(1), 82–91. https://doi.org/10.1038/s41594-023-01143-z

McBride, C., Trzoss, L., Povero, D., Lazic, M., Ambrus-Aikelin, G., Santini, A., Pranadinata, R., Bain, G., Stansfield, R., Stafford, J. A., Veal, J., Takahashi, R., Ly, J., Chen, S., Liu, L., Nespi, M., Blake, R., Katewa, A., Kleinheinz, T., … Stivala, C. E. (2022). Overcoming Preclinical Safety Obstacles to Discover (S)-N-((1,2,3,5,6,7-Hexahydro-s-indacen-4-yl)carbamoyl)-6-(methylamino)-6,7-dihydro-5H-pyrazolo[5,1-b][1,3]oxazine-3-sulfonamide (GDC-2394): A Potent and Selective NLRP3 Inhibitor. *Journal of Medicinal Chemistry*, *65*(21), 14721–14739. https://doi.org/10.1021/acs.jmedchem.2c01250

Meunier, E., & Broz, P. (2017). Evolutionary Convergence and Divergence in NLR Function and Structure. *Trends in Immunology*, *38*(10), 744–757. https://doi.org/10.1016/j.it.2017.04.005

Mi, L., Min, X., Chai, Y., Zhang, J., & Chen, X. (2022). NLRP1 Inflammasomes: A Potential Target for the Treatment of Several Types of Brain Injury. *Frontiers in Immunology*, *13*, 863774. https://doi.org/10.3389/fimmu.2022.863774

Miao, J., Zhang, J., Huang, X., Wu, N., Wu, D., & Shen, M. (2023). NLRP12-associated autoinflammatory disease in Chinese adult patients: a single-centre study. *RMD Open*, *9*(4), e003598. https://doi.org/10.1136/rmdopen-2023-003598

Mo, J., Boyle, J. P., Howard, C. B., Monie, T. P., Davis, B. K., & Duncan, J. A. (2012). Pathogen Sensing by Nucleotide-binding Oligomerization Domain-containing

Protein 2 (NOD2) Is Mediated by Direct Binding to Muramyl Dipeptide and ATP*. *Journal of Biological Chemistry*, *287*(27), 23057–23067. https://doi.org/10.1074/jbc.m112.344283

Morelli, G., Song, Y., Mazzoni, C. J., Eppinger, M., Roumagnac, P., Wagner, D. M., Feldkamp, M., Kusecek, B., Vogler, A. J., Li, Y., Cui, Y., Thomson, N. R., Jombart, T., Leblois, R., Lichtner, P., Rahalison, L., Petersen, J. M., Balloux, F., Keim, P., … Achtman, M. (2010). Yersinia pestis genome sequencing identifies patterns of global phylogenetic diversity. *Nature Genetics*, *42*(12), 1140–1143. https://doi.org/10.1038/ng.705

Motta, V., Soares, F., Sun, T., & Philpott, D. J. (2015). NOD-Like Receptors: Versatile Cytosolic Sentinels. *Physiological Reviews*, *95*(1), 149–178. https://doi.org/10.1152/physrev.00009.2014

Ogura, Y., Inohara, N., Benito, A., Chen, F. F., Yamaoka, S., & Núñez, G. (2001). Nod2, a Nod1/Apaf-1 Family Member That Is Restricted to Monocytes and Activates NF-κB*. *Journal of Biological Chemistry*, *276*(7), 4812–4818. https://doi.org/10.1074/jbc.m008072200

O'Keefe, M. E., Dubyak, G. R., & Abbott, D. W. (2024). Post-translational control of NLRP3 inflammasome signaling. *Journal of Biological Chemistry*, *300*(6), 107386. https://doi.org/10.1016/j.jbc.2024.107386

Peter, M. F., Ruland, J. A., Depping, P., Schneberger, N., Severi, E., Moecking, J., Gatterdam, K., Tindall, S., Durand, A., Heinz, V., Siebrasse, J. P., Koenig, P.-A., Geyer, M., Ziegler, C., Kubitscheck, U., Thomas, G. H., & Hagelueken, G. (2022). Structural and mechanistic analysis of a tripartite ATP-independent periplasmic TRAP transporter. *Nature Communications*, *13*(1), 4471. https://doi.org/10.1038/s41467-022-31907-y

Pinheiro, A. S., Eibl, C., Ekman-Vural, Z., Schwarzenbacher, R., & Peti, W. (2011). The NLRP12 Pyrin Domain: Structure, Dynamics, and Functional Insights. *Journal of Molecular Biology*, *413*(4), 790–803. https://doi.org/10.1016/j.jmb.2011.09.024

Platnich, J. M., & Muruve, D. A. (2019). NOD-like receptors and inflammasomes: A review of their canonical and non-canonical signaling pathways. *Archives of Biochemistry and Biophysics*, *670*, 4–14. https://doi.org/10.1016/j.abb.2019.02.008

Próchnicki, T., Vasconcelos, M. B., Robinson, K. S., Mangan, M. S. J., Graaf, D. D., Shkarina, K., Lovotti, M., Standke, L., Kaiser, R., Stahl, R., Duthie, F. G., Rothe, M., Antonova, K., Jenster, L.-M., Lau, Z. H., Rösing, S., Mirza, N., Gottschild, C., Wachten, D., … Latz, E. (2023). Mitochondrial damage activates the NLRP10 inflammasome. *Nature Immunology*, *24*(4), 595–603. https://doi.org/10.1038/s41590-023-01451-y

Püschel, G., Kühn, H., Kietzmann, T., Höhne, W., Christ, B., Doenecke, D., & Koolman, J. (2011). *Taschenlehrbuch Biochemie* (1st ed.). Georg Thieme Verlag KG.

Rathinam, V. A. K., Jiang, Z., Waggoner, S. N., Sharma, S., Cole, L. E., Waggoner, L., Vanaja, S. K., Monks, B. G., Ganesan, S., Latz, E., Hornung, V., Vogel, S. N., Szomolanyi-Tsuda, E., & Fitzgerald, K. A. (2010). The AIM2 inflammasome is essential for host defense against cytosolic bacteria and DNA viruses. *Nature Immunology*, *11*(5), 395–402. https://doi.org/10.1038/ni.1864

Rehwinkel, J., & Gack, M. U. (2020). RIG-I-like receptors: their regulation and roles in RNA sensing. *Nature Reviews Immunology*, *20*(9), 537–551. https://doi.org/10.1038/s41577-020-0288-3

Reubold, T. F., Hahne, G., Wohlgemuth, S., & Eschenburg, S. (2014). Crystal structure of the leucine-rich repeat domain of the NOD-like receptor NLRP1: Implications for binding of muramyl dipeptide. *FEBS Letters*, *588*(18), 3327–3332. https://doi.org/10.1016/j.febslet.2014.07.017

Rigante, D. (2012). The fresco of autoinflammatory diseases from the pediatric perspective. *Autoimmunity Reviews*, *11*(5), 348–356. https://doi.org/10.1016/j.autrev.2011.10.008

Robert, X., & Gouet, P. (2014). Deciphering key features in protein structures with the new ENDscript server. *Nucleic Acids Research*, *42*(W1), W320–W324. https://doi.org/10.1093/nar/gku316

Ruan, J., Wei, X., Li, S., Ye, Z., Hu, L., Zhuang, R., Cao, Y., Wang, S., Wu, S., Peng, D., Chen, S., Yuan, S., & Xu, A. (2025). Apaf-1 is an evolutionarily conserved DNA sensor that switches the cell fate between apoptosis and inflammation. *Cell Discovery*, *11*(1), 4. https://doi.org/10.1038/s41421-024-00750-4

Salomão, R., Martins, P. S., Brunialti, M. K. C., Fernandes, M. da L., Martos, L. S. W., Mendes, M. E., Gomes, N. E., & Rigato, O. (2008). TLR SIGNALING PATHWAY IN PATIENTS WITH SEPSIS. *Shock*, *30*(7), 73–77. https://doi.org/10.1097/shk.0b013e318181af2a

Sandall, C. F., Ziehr, B. K., & MacDonald, J. A. (2020a). ATP-Binding and Hydrolysis in Inflammasome Activation. *Molecules*, *25*(19), 4572. https://doi.org/10.3390/molecules25194572

Sandall, C. F., Ziehr, B. K., & MacDonald, J. A. (2020b). ATP-Binding and Hydrolysis in Inflammasome Activation. *Molecules*, *25*(19), 4572. https://doi.org/10.3390/molecules25194572

Schnappauf, O., Chae, J. J., Kastner, D. L., & Aksentijevich, I. (2019). The Pyrin Inflammasome in Health and Disease. *Frontiers in Immunology*, *10*, 1745. https://doi.org/10.3389/fimmu.2019.01745

Schwartz, R. S., Netea, M. G., & Meer, J. W. M. van der. (2011). Immunodeficiency and Genetic Defects of Pattern-Recognition Receptors. *The New England Journal of Medicine*, *364*(1), 60–70. https://doi.org/10.1056/nejmra1001976

Shaw, M. H., Reimer, T., Kim, Y.-G., & Nuñez, G. (2008). NOD-like receptors (NLRs): bona fide intracellular microbial sensors. *Current Opinion in Immunology*, *20*(4), 377–382. https://doi.org/10.1016/j.coi.2008.06.001

Shaw, P. J., Lamkanfi, M., & Kanneganti, T. (2010). NOD-like receptor (NLR) signaling beyond the inflammasome. *European Journal of Immunology*, *40*(3), 624–627. https://doi.org/10.1002/eji.200940211

Shen, C., Lu, A., Xie, W. J., Ruan, J., Negro, R., Egelman, E. H., Fu, T.-M., & Wu, H. (2019). Molecular mechanism for NLRP6 inflammasome assembly and activation. *Proceedings of the National Academy of Sciences*, *116*(6), 2052–2057. https://doi.org/10.1073/pnas.1817221116

Shi, C., Gao, T., Lyu, W., Qiang, B., Chen, Y., Chen, Q., Zhang, L., & Liu, Z. (2024). Deep-Learning-Driven Discovery of SN3–1, a Potent NLRP3 Inhibitor with Therapeutic Potential for Inflammatory Diseases. *Journal of Medicinal Chemistry*, *67*(19), 17833–17854. https://doi.org/10.1021/acs.jmedchem.4c01857

Sousa, C. R. e, Yamasaki, S., & Brown, G. D. (2024). Myeloid C-type lectin receptors in innate immune recognition. *Immunity*, *57*(4), 700–717. https://doi.org/10.1016/j.immuni.2024.03.005

Stafford, C. A., Gassauer, A.-M., Mann, C. C. de O., Tanzer, M. C., Fessler, E., Wefers, B., Nagl, D., Kuut, G., Sulek, K., Vasilopoulou, C., Schwojer, S. J., Wiest, A., Pfautsch, M. K., Wurst, W., Yabal, M., Fröhlich, T., Mann, M., Gisch, N., Jae, L. T., & Hornung, V. (2022). Phosphorylation of muramyl peptides by NAGK is required for NOD2 activation. *Nature*, *609*(7927), 590–596. https://doi.org/10.1038/s41586-022-05125-x

Strober, W., Murray, P. J., Kitani, A., & Watanabe, T. (2006). Signalling pathways and molecular interactions of NOD1 and NOD2. *Nature Reviews Immunology*, *6*(1), 9–20. https://doi.org/10.1038/nri1747

Strober, W., & Watanabe, T. (2011). NOD2, an intracellular innate immune sensor involved in host defense and Crohn's disease. *Mucosal Immunology*, *4*(5), 484–495. https://doi.org/10.1038/mi.2011.29

Strzyz, P. (2020). CRISPR–Cas9 wins Nobel. *Nature Reviews Molecular Cell Biology*, *21*(12), 714–714. https://doi.org/10.1038/s41580-020-00307-9

Su, M. Y., Chang, C. F., & Chang, C. I. (2013). *Three-dimensional structure of human NLRP10/PYNOD pyrin domain*. https://doi.org/10.2210/pdb2m5v/pdb

Sundaram, B., Tweedell, R. E., Kumar, S. P., & Kanneganti, T.-D. (2024). The NLR family of innate immune and cell death sensors. *Immunity*, *57*(4), 674–699. https://doi.org/10.1016/j.immuni.2024.03.012

Swanson, K. V., Deng, M., & Ting, J. P.-Y. (2019). The NLRP3 inflammasome: molecular activation and regulation to therapeutics. *Nature Reviews Immunology*, *19*(8), 477–489. https://doi.org/10.1038/s41577-019-0165-0

Takeuchi, O., & Akira, S. (2010). Pattern Recognition Receptors and Inflammation. *Cell*, *140*(6), 805–820. https://doi.org/10.1016/j.cell.2010.01.022

Tang, W. K., & Xia, D. (2016). Role of the D1-D2 Linker of Human VCP/p97 in the Asymmetry and ATPase Activity of the D1-domain. *Scientific Reports*, *6*(1), 20037. https://doi.org/10.1038/srep20037

Tapia-Abellán, A., Angosto-Bazarra, D., Alarcón-Vila, C., Baños, M. C., Hafner-Bratkovič, I., Oliva, B., & Pelegrín, P. (2021). Sensing low intracellular potassium by NLRP3 results in a stable open structure that promotes inflammasome activation. *Science Advances*, *7*(38), eabf4468. https://doi.org/10.1126/sciadv.abf4468

Thompson, M. R., Kaminski, J. J., Kurt-Jones, E. A., & Fitzgerald, K. A. (2011). Pattern Recognition Receptors and the Innate Immune Response to Viral Infection. *Viruses*, *3*(6), 920–940. https://doi.org/10.3390/v3060920

Tuladhar, S., & Kanneganti, T.-D. (2020). NLRP12 in innate immunity and inflammation. *Molecular Aspects of Medicine*, *76*, 100887. https://doi.org/10.1016/j.mam.2020.100887

Valanne, S., Wang, J.-H., & Rämet, M. (2011). The Drosophila Toll Signaling Pathway. *The Journal of Immunology*, *186*(2), 649–656. https://doi.org/10.4049/jimmunol.1002302

Varadi, M., Bertoni, D., Magana, P., Paramval, U., Pidruchna, I., Radhakrishnan, M., Tsenkov, M., Nair, S., Mirdita, M., Yeo, J., Kovalevskiy, O., Tunyasuvunakool, K., Laydon, A., Žídek, A., Tomlinson, H., Hariharan, D., Abrahamson, J., Green, T., Jumper, J., … Velankar, S. (2023). AlphaFold Protein Structure Database in 2024: providing structure coverage for over 214 million protein sequences. *Nucleic Acids Research*, *52*(D1), D368–D375. https://doi.org/10.1093/nar/gkad1011

Verma, D., Fekri, S. Z., Sigurdardottir, G., Eding, C. B., Sandin, C., & Enerbäck, C. (2021). Enhanced Inflammasome Activity in Patients with Psoriasis Promotes Systemic Inflammation. *Journal of Investigative Dermatology*, *141*(3), 586-595.e5. https://doi.org/10.1016/j.jid.2020.07.012

Vladimer, G. I., Weng, D., Paquette, S. W. M., Vanaja, S. K., Rathinam, V. A. K., Aune, M. H., Conlon, J. E., Burbage, J. J., Proulx, M. K., Liu, Q., Reed, G., Mecsas, J. C., Iwakura, Y., Bertin, J., Goguen, J. D., Fitzgerald, K. A., & Lien, E. (2012). The NLRP12 Inflammasome Recognizes Yersinia pestis. *Immunity*, *37*(1), 96–107. https://doi.org/10.1016/j.immuni.2012.07.006

Wang, H. (2022). NLRP12-associated systemic autoinflammatory diseases in children. *Pediatric Rheumatology*, *20*(1), 9. https://doi.org/10.1186/s12969-022-00669-8

Wang, L., Manji, G. A., Grenier, J. M., Al-Garawi, A., Merriam, S., Lora, J. M., Geddes, B. J., Briskin, M., DiStefano, P. S., & Bertin, J. (2002). PYPAF7, a Novel PYRIN-containing Apaf1-like Protein That Regulates Activation of NF-κB and Caspase-1-dependent Cytokine Processing*. *Journal of Biological Chemistry*, *277*(33), 29874–29880. https://doi.org/10.1074/jbc.m203915200

Wang, Y., Hasegawa, M., Imamura, R., Kinoshita, T., Kondo, C., Konaka, K., & Suda, T. (2004). PYNOD, a novel Apaf-1/CED4-like protein is an inhibitor of ASC and caspase-1. *International Immunology*, *16*(6), 777–786. https://doi.org/10.1093/intimm/dxh081

Watson, J. L., Juergens, D., Bennett, N. R., Trippe, B. L., Yim, J., Eisenach, H. E., Ahern, W., Borst, A. J., Ragotte, R. J., Milles, L. F., Wicky, B. I. M., Hanikel, N., Pellock, S. J., Courbet, A., Sheffler, W., Wang, J., Venkatesh, P., Sappington, I., Torres, S. V., … Baker, D. (2023). De novo design of protein structure and function with RFdiffusion. *Nature*, *620*(7976), 1089–1100. https://doi.org/10.1038/s41586-023-06415-8

Weber, A. N. R., McManus, R. M., Hornung, V., Geyer, M., Kuemmerle-Deschner, J. B., & Latz, E. (2025). The expanding role of the NLRP3 inflammasome from periodic fevers to therapeutic targets. *Nature Immunology*, 1–14. https://doi.org/10.1038/s41590-025-02230-7

Wein, T., & Sorek, R. (2022). Bacterial origins of human cell-autonomous innate immune mechanisms. *Nature Reviews Immunology*, *22*(10), 629–638. https://doi.org/10.1038/s41577-022-00705-4

Wendler, P., Ciniawsky, S., Kock, M., & Kube, S. (2012). Structure and function of the AAA+ nucleotide binding pocket. *Biochimica et Biophysica Acta (BBA) - Molecular Cell Research*, *1823*(1), 2–14. https://doi.org/10.1016/j.bbamcr.2011.06.014

Xiao, L., Magupalli, V. G., & Wu, H. (2023). Cryo-EM structures of the active NLRP3 inflammasome disc. *Nature*, *613*(7944), 595–600. https://doi.org/10.1038/s41586-022-05570-8

Yang, Y., Lv, J., Jiang, S., Ma, Z., Wang, D., Hu, W., Deng, C., Fan, C., Di, S., Sun, Y., & Yi, W. (2016). The emerging role of Toll-like receptor 4 in myocardial inflammation. *Cell Death & Disease*, *7*(5), e2234–e2234. https://doi.org/10.1038/cddis.2016.140

Yao, J., & Wang, X. (2025). Artificial intelligence in de novo protein design. *Medicine in Novel Technology and Devices*, *26*, 100366. https://doi.org/10.1016/j.medntd.2025.100366

Ye, Z., Lich, J. D., Moore, C. B., Duncan, J. A., Williams, K. L., & Ting, J. P.-Y. (2008). ATP Binding by Monarch-1/NLRP12 Is Critical for Its Inhibitory Function. *Molecular and Cellular Biology*, *28*(5), 1841–1850. https://doi.org/10.1128/mcb.01468-07

Zheng, D., Mohapatra, G., Kern, L., He, Y., Shmueli, M. D., Valdés-Mas, R., Kolodziejczyk, A. A., Próchnicki, T., Vasconcelos, M. B., Schorr, L., Hertel, F., Lee, Y. S., Rufino, M. C., Ceddaha, E., Shimshy, S., Hodgetts, R. J., Dori-Bachash, M., Kleimeyer, C., Goldenberg, K., … Elinav, E. (2023). Epithelial Nlrp10 inflammasome mediates protection against intestinal autoinflammation. *Nature Immunology*, *24*(4), 585–594. https://doi.org/10.1038/s41590-023-01450-z

Zheng, M., Karki, R., Williams, E. P., Yang, D., Fitzpatrick, E., Vogel, P., Jonsson, C. B., & Kanneganti, T.-D. (2021). TLR2 senses the SARS-CoV-2 envelope protein to produce inflammatory cytokines. *Nature Immunology*, *22*(7), 829–838. https://doi.org/10.1038/s41590-021-00937-x

Zipfel, C. (2014). Plant pattern-recognition receptors. *Trends in Immunology*, *35*(7), 345–351. https://doi.org/10.1016/j.it.2014.05.004

Zou, H., Henzel, W. J., Liu, X., Lutschg, A., & Wang, X. (1997). Apaf-1, a Human Protein Homologous to C. elegans CED-4, Participates in Cytochrome c–Dependent Activation of Caspase-3. *Cell*, *90*(3), 405–413. https://doi.org/10.1016/s0092-8674(00)80501-2

Zurek, B., Proell, M., Wagner, R. N., Schwarzenbacher, R., & Kufer, T. A. (2010). Mutational analysis of human NOD1 and NOD2 NACHT domains reveals different modes of activation. *Innate Immunity*, *18*(1), 100–111. https://doi.org/10.1177/1753425910394002

List of Abbreviations

&	and
%	percent
°	degrees
°C	degrees Celsius
<	less than
>	greater than
~	approximately
Å	Angstrom (0.1 nm)
A_x	absorbance at x nm
aa	amino acids
AC	affinity chromatography
ADP	adenosine diphosphate
AIM2	absent in melanoma-2
ALR	AIM2-like receptor
AMP	adenosine monophosphate
Amp	ampicillin
APAF-1	apoptotic protease activating factor-1
APS	ammonium persulfate
ASC	apoptosis-associated speck-like protein containing a CARD
ATP	adenosine triphosphate
ATPase	adenosine triphosphatase
ATPγS	adenosine 5′-O-(3-thio)triphosphate
B-cell	bone marrow lymphocytes
BFP	blue fluorescent protein
BIR	baculovirus inhibitor of apoptosis protein repeat
BMDMs	bone marrow-derived macrophages
bp	base pair
BSA	bovine serum albumin
c	concentration
C-term	carboxy terminus
CAPS	cryopyrin-associated periodic syndrome
CARD	caspase activation and recruitment domain
CD14	cluster of differentiation 14
CHAPS	3-[(3-cholamidopropyl)dimethylammonio]-1-propanesulfonate
CIITA	class II, major histocompatibility complex, transactivator
CLR	C-type lectin receptor
cm	centimeter
CMD	carboxymethyl dextran
cn	canonical
COVID-19	coronavirus disease 2019
CRID	cytokine release inhibitory drug
cryo	cryogenic
CTD	C-terminal domain
CTLD	C-type lectin-like domain
CV	column volume
d	distance

Da	Dalton
DAMP	damage-associated molecular pattern
DC	dendritic cell
DD	death domain
Dectin	dendritic cell-associated C-type lectin
DESY	Deutsches Elektronen Synchrotron
DLS	dynamic light scattering
DMSO	dimethyl sulfoxide
DNA	deoxyribonucleic acid
DNase	deoxyribonuclease
dNTP	deoxynucleotide triphosphates
DPP9	dipeptidyl peptidase 9
ds	double-stranded
DTT	dithiothreitol
E. coli	*Escherichia coli*
e.g.	example given
EDTA	ethylenediaminetetraacetic acid
EM	electron microscopy
ER	endoplasmatic reticulum
et al.	et alia, et alii, et aliae
etc.	et cetera
FAF	Fas-associated factor
FCAS	familial cold autoinflammatory syndrome
FIND	function to find domain
FISNA	fish-specific NACHT-associated domain
FPLC	fast protein liquid chromatography
fw	forward
Gent	gentamycin
GFP	green fluorescent protein
GSDMD	gasdermin D
GST	glutathione-*S*-transferase
h	hour
HD	helical domain
HEPES	4-(2-hydroxyethyl)-1-piperazineethanesulfonic acid
HET-E	Incompatibility locus protein from *Podospora anserina*
HIV	human immunodeficiency virus
hNLRP	human NLRP
HPLC	high performance liquid chromatography
HSP	heat shock protein
Hz	hertz
I	intensity
IFN	interferon
IKK	IκB kinase
IL	interleukin
IPTG	isopropyl-β-D-thiogalactopyranoside
IRAK	IL-1R associated kinase
k_a	second-order association constant
kb	kilobase

kbp	kilobase pair
K_D	equilibrium dissociation constant
k_d	first-order dissociation constant
kDa	kilodalton
kV	kilovolt
L	liter
l	length
LB	lysogeny broth
LGP2	laboratory of genetics and physiology 2
LLPS	liquid-liquid phase separation
LPS	lipopolysaccharide
LRR	leucine-rich repeat
M	marker or molar
mA	milliampere
MALS	multi angle light scattering
MAPK	mitogen-activated protein kinase
mAU	milli-absorbance unit
MAVS	mitochondrial antiviral-signaling protein
MBP	maltose binding protein
mCherry	monomeric Cherry
MCS	multiple cloning site
MDA5	melanoma differentiation-associated protein 5
MDP	muramyl dipeptide
mg	milligram
min	minute
ml	milliliter
mM	millimolar
MW	molecular weight
MWCO	molecular weight cut-off
MWS	Muckle-Wells syndrome
MyD88	myeloid differentiation primary response 88
N-term	amino terminus
NACHT	acronym for NAIP, CIITA, HET-E, and TP1
NAIP	NLR Family Apoptosis Inhibitory Protein
nanoDSF	nano-format differential scanning fluorimetry
NBD	nucleotide binding domain
NEK7	NIMA-related kinase 7
NF-κB	nuclear factor kappa B
ng	nanogram
NIK	NF-κB-inducing kinase
NK cell	natural killer cell
NLR	NOD-like receptor
NLRA	NLR family acidic transactivating domain containing protein
NLRB	NLR family BIR domain containing protein
NLRC	NLR family CARD containing protein
NLRP	NLR family PYD containing protein
NLRX	NLR family protein containing an unknown N-terminal effector domain
nm	nanometer

nM	nanomolar
NMR	Nuclear magnet resonance
NOD	nucleotide-binding oligomerization domain
ns	not significant
OD	optical density
o.n.	overnight
PAGE	Polyacrylamide gel electrophoresis
PAMP	pathogen-associated molecular pattern
PBS	phosphate-buffered saline
PCR	polymerase chain reaction
PDB	protein data bank
PEG	polyethylene glycol
PGN	peptidoglycan
pH	potentia hydrogenii
pI	isoelectric point
PMSF	phenylmethylsulfonylfluoride
PRR	pattern recognition receptor
PTM	post-translational modifications
PYD	Pyrin domain
rv	reverse
r_H	hydrodynamic radius
r.c.f.	relative centrifugal force
RI	refractive index
RIG-I	retinoic acid-inducible gene-I
RIPK	receptor-interacting serine/threonine-protein kinase
RLRs	RIG-I-like receptors
RMSD	root-mean-square deviation
RNA	ribonucleic acid
rpm	revolutions per minute
RT	room temperature
RU	response unit
sec	second
SDS	sodium dodecyl sulfate
SEC	size-exclusion chromatography
Sf9	*Spodoptera Frugiperda* 9
SMILES	simplified molecular input line entry specification
SPR	surface plasmon resonance
ss	Single-stranded
STAND	signal transduction ATPases with numerous domains
Syk	spleen tyrosine kinase
T	temperature
T-cell	thymus lymphocytes
TAE	tris-acetate-EDTA
TCEP	tris(2-carboxyethyl)phosphine
TEM	transmission electron microscope
TEMED	tetramethyl ethylenediamine
Tet	tetracycline
TEV	tobacco etch virus

THP1	human leukemia monocytic cell line
TIR	Toll-interleukin-1 receptor
TLR	Toll-like receptor
T_M	melting temperature
TNF	tumor necrosis factor
tr	transition
Tris	tris(hydroxymethyl)aminomethane
U	units
UPA	acronym for UNC5, PIDD, and Ankyrins
UT	untreated
UV	ultraviolet
V	volt
v/v	volume to volume
V_0, V_1, V_2	Viral stocks
Vis	visible spectroscopy
w/o	without
w/v	weight to volume
w/w	weight to weight
WHD	winged helix domain
X-gal	5-bromo-4-chloro-3-indolyl β-D-galactopyranoside
X-ray	roentgen radiation
ZU5	acronym for ZO-1 and UNC5
α	alpha, alpha helix
β	beta, beta helix
βME	β-mercaptoethanol
γ	gamma
Δ	delta
ε	extinction coefficient
η	3_{10}-helix
λ	wavelength
µg	microgram
µl	microliter
µM	micromolar
µm	micrometer
σ	sigma

Elements and their ions as well as chemicals, including nucleotides and amino acids are abbreviated according to the IUPAC nomenclature.

List of Figures

List of Tables